STRUCTURAL COMPLEXITIES

IN

SYNTHETIC SELF-ASSEMBLING NANOMATERIALS

A Dissertation

Presented to the Faculty of the Graduate School

of Cornell University

In Partial Fulfillment of the Requirements for the Degree of

Doctor of Philosophy

by

Hiroaki Sai

January, 2013

STRUCTURAL COMPLEXITIES IN SYNTHETIC NANOMATERIALS

Hiroaki Sai, Ph. D.

Cornell University, 2013

Self-assembly of amphiphilic molecules such as surfactants and amphiphilic block copolymers (BCPs), provides an energy-efficient bottom-up approach for controllably creating structures at the mesoscale (2-50 nm) with potential applications in catalysis, next-generation energy production and storage devices, optical metamaterials and bioengineered materials. Biological systems serve as examples of complex materials at mesoscopic length scales that integrate structural and compositional heterogeneities that lead to functions including toughness, optical iridescence and van der Waals adhesion due to large surface area.

In this dissertation, I will describe three different approaches for adding structural complexity to synthetic mesoscale structures. Firstly, controlled synthesis and detailed characterization of multicompartment mesoporous silica nanoparticles (multi-MSNs) from surfactant coassembly with sol-gel silica is described. These multi-MSNs consist of a core with cage-like cubic mesoporous network morphology and up to four fingers/branches with hexagonally packed cylindrical mesopores epitaxially emanating from the vertices of the cubic core. These multi-MSNs are mesoscale structural analogues to branched semiconductor nanocrystals. Possible nucleation and growth processes leading to this particle morphology are discussed. Secondly, multicomponent evaporation-induced self-assembly behavior of ligand-stabilized platinum nanoparticles (Pt NPs) with poly(isoprene-block-dimethylaminoethyl methacrylate) block copolymers is discussed. Detailed characterization on Pt NPs

revealed sparse ligand coverage. Changing the volume fraction of Pt NPs in BCP-NP composites yielded organic-inorganic hybrids with spherical micellar, wormlike micellar, lamellar and inverse hexagonal mesoscale morphologies. Disassembly of hybrids with spherical, wormlike micellar, and lamellar morphologies generated isolated metal-NP based nanospheres, cylinders and sheets, respectively. Results suggest the existence of powerful design criteria for the formation of metal-based nanostructures from designer blocked macromolecules. Finally, a facile synthesis protocol for hierarchically structured polymeric scaffolds with highly ordered mesopores is introduced. Mixtures of poly(styrene-*block*-ethylene oxide) BCPs with oligomeric poly(ethylene oxide) additives were dissolved in high boiling point solvents, and bulk films were cast through solvent evaporation. Spinodal decomposition of the BCP/additive mixture resulted in macrostructure formation, with the BCP-rich domains forming ordered mesostructures. Facile washing of the films resulted in the formation of macro/meso-porous three-dimensional polymer scaffolds. Experimental parameters relevant for structure formation including additive molecular weights, solvents and drying temperatures are explored.

BIOGRAPHICAL SKETCH

Hiroaki Sai was born in Matsudo, Chiba Pref. Japan on October 20th, 1984. After moving to Yokohama, he went to Kenzan Elementary School. In the September of 1992, he was absolutely thrilled to watch the Space Shuttle Endeavor launch with the first Japanese astronaut on the television, which eventually became his first source of motivation for studying in the field of science and technology. From 1997 to 2003, Hiro attended Eiko Gakuen High School, where he was inspired by splendid friends and the beautiful surroundings of Kamakura. The teachers in Eiko High gave him tremendous amount of care and mentoring through various opportunities, such as reading Euclid's *Elements*, club activity camp for stargazing with a telescope, playing violin in the school orchestra, and providing laboratory experiences in chemistry, which prepared him for the winning the Chemical Society of Japan Award in the Japanese National High School Chemistry Olympiad in 2002.

After a short period of enrollment in the University of Tokyo, Hiro travelled overseas for the second time in his life (his first time was a five-day trip to Hong Kong for a math competition when he was 11 years old) to commence his study at Princeton University as a member of the Class of 2007. Under the supervision of Prof. Ilhan Aksay in the Department of Chemical Engineering, Hiro started to work in the Ceramic Materials Laboratory on the mesoporous silica formation under capillary electroosmotic flow. His interest for materials science and engineering grew with this laboratory experience, and he subsequently stayed in the lab for the next three years till the senior thesis project, in which the mechanical properties of L_3 sponge-phase templated silica were investigated. Outside of laboratory and classrooms, Hiro served as an undergraduate Residential College Advisor in the Butler College in Princeton for two years, first as an assistant advisor and then full, where he made friends with Hiro

graduated from Princeton University in the May of 2007 as a Bachelor of Science in Engineering with Highest Honors. From the fall of 2007, Hiro has attended graduate school in the Department of Materials Science and Engineering in Cornell University in the research group of Prof. Ulrich Wiesner, with Profs. Lara A. Estroff and Sol M. Gruner as co-advisors.

This dissertation is dedicated to each and every one who interacted with me in the past.

Without you, I would not have been able to stand where I am now.

Spencer Robbins, Kwan Wee Tan, Christina Cowman, Yibei Gu, and recently Ji-yeob Kim were all great office-mates in Thurston 304 and I greatly enjoyed the countless discussions we had, be it research-related or completely tangential. I would like to thank all of the Wiesner group members, past and present, for bearing with my sometimes-endless questions in the group meetings and fun times in group activities. Finally, I would like to thank Dolores Dewbury, as known as the magic person we could rely on for any administrative issues.

By participating in other groups than my main research group, I was fortunate to be able to take a glimpse of completely different projects and learning perspectives I would never have thought of. I would like to thank the Estroff group members, especially Dr. Jason Dorvee and Dr. Debra Lin and Dr. Ruiqi Song for the hydroxyapatite project. I would like to thank the Gruner group members, especially Dr. Mark Tate who taught me on the rotating anode beamline, Dr. Suntao Wang who collaborated with the terpolymer hybrid analysis, and Dr. Yi-fan Chen for instruction on the high-pressure beryllium cell setup.

It was a great privilege working with many people other than graduate students in our groups: these include the suite of enthusiastic undergrads Patrick Kiernan, Christopher Sarra, Samantha Smith, Andrea Bowring, Alden Coots and Dan Shae, visiting professors and scientists Yuzo Fujiki, Prof. Taeghwan Hyeon, Tatsuro Morimoto, Stefan Guldin, Kazufumi Kawahara, Rina Maeda, Prof. Byoung-Ki Cho and Prof. Rodrigo Orefice, and other external collaborators Joshua Choi, Will Baumgardner, Dave Moore, Robert Hovden, Mihaela Nedelcu, Azusa Takai, and Asuka Toda.

Virtually none of the characterization work could have been done without the facility managers. I would like to thank the Cornell Center of Materials Research (CCMR) staff: Dr. John Hunt, Dr. John Grazul, Dr. Mick Thomas and Dr. Yuanming

TABLE OF CONTENTS

LIST OF FIGURES

LIST OF TABLES

CHAPTER 1

INTRODUCTION

Overview

The role of the nanoscale in materials science and engineering has a long-standing history, dating back to the production of stained glass using the tunable plasmonic absorption spectrum of gold nanoparticles[1] or hardening of steel by carbon inclusions,[2] to name only a few examples. These discoveries, albeit lacking an understanding of the underlying mechanisms at their times, are associated with endeavors to manipulate the bulk intensive properties of materials such as density, color, modulus, or electrical conductivity. As these properties originate from interactions of atoms and molecules, designing and characterizing nanoscale structures near the length scale of these building blocks would enable direct observation and tuning of structure-property relationships rather than the historical trial-and-error approaches.

Biologically occurring materials provide a plethora of inspirations for how to design nanometer and micrometer scale structures for achieving such goals without the use of energetically costly approaches such as lithography or high-temperature processing. Many living organisms use abundant elements on earth such as silicon, calcium, iron and lighter elements, and through directing structures and compositions at varying length scales ranging from atomic to millimeter-range or larger, synthesize functional materials such as optically active butterfly wing scales,[3] mechanically

robust bone,[4] or universally adhesive gecko feet.[5] In each case, organic templates made from biological molecules whose information is encoded in DNA form the building blocks for organization at a larger length scale using local interactions, hence the name *bottom-up self-assembly*. Researchers have realized the effectiveness of self-assembly in synthetic materials and have recently used synthetic structure-directing agents to guide materials synthesis at nanometer- and micrometer-scales.[6]

Amphiphilic molecules for nanoscale self-assembly and structure-direction

In this section, we will review two types of structure-directing agents. Surfactants (short for surface active agents) are a class of materials that lowers the interfacial energies between distinct phases.[7] Surfactants generally consist of hydrophilic head portions covalently attached to hydrophobic tails. An example of such a molecule is cetyltrimethylammonium bromide (CTAB), which consists of a quaternary ammonium head attached to a C_{16} hydrocarbon tail. When dissolved in water, CTAB molecules stay as unimolecular species in solution below a certain concentration called critical micelle concentration (CMC). Above the CMC they aggregate in water into mesoscale (2-50nm) spherical, hexagonally packed cylindrical, cubic, or lamellar supramolecular structures. The morphologies formed depend on the concentration of CTAB, and thus are termed lyotropic liquid crystals (LLCs). Figure 1.1 illustrates the phase diagram of the CTAB-water model system.[8] Combination of surfactant self-assembly with sol-gel processing of ceramics results in LLC-templated organic-inorganic hybrids (see Figure 1.2),[8] in which the inorganic precursors in solution undergo hydrolysis and condensation to form a sol and then a crosslinked

2
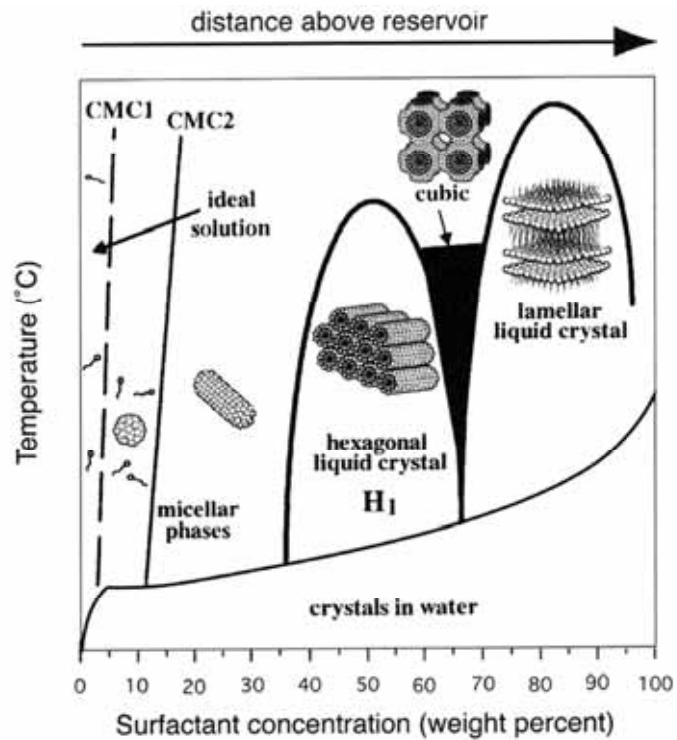
Figure 1.1. Schematic water-CTAB phase diagram. Reproduced from Brinker *et al*. with permission.[7]
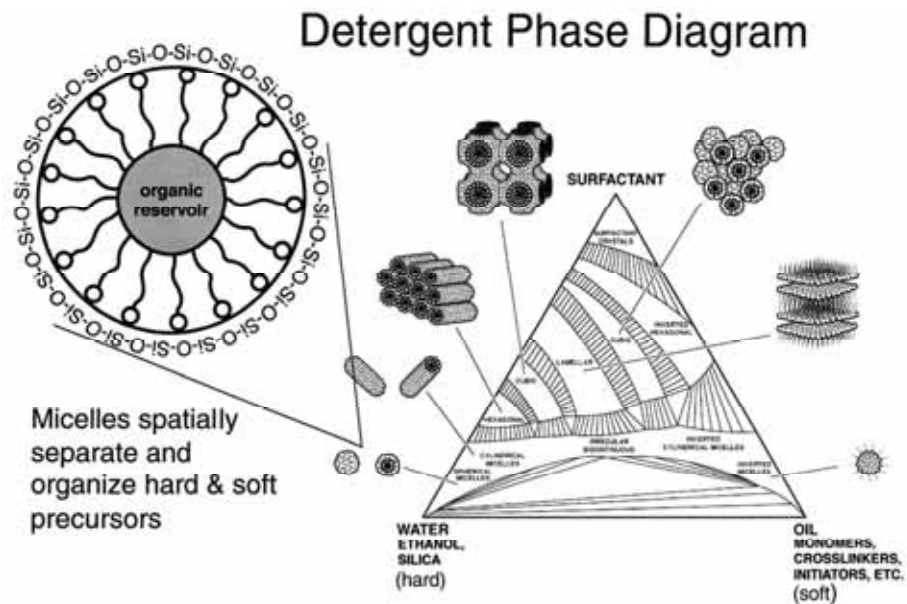
Figure 1.2. Schematic mesoporous silica formation phase diagram from surfactant-oil-water systems. Reproduced from Brinker *et al*. with permission.[7]

network (gel) that precipitates out of solution. By tuning environmental parameters such as temperature, pH, ionic strength and solvents, the kinetics for hydrolysis and condensation can be adjusted so that the cluster size and dispersibility can be optimized for structure-directing inorganic species. While the first mention of using surfactants to co-assemble nanostructured materials dates back to a patent in 1971,[9] the first report on mesostructured silica through surfactants appeared in 1990,[10] followed by a seminal paper from the Mobil group in 1992.[11] Since then, a large number of research groups have followed the route to produce nanostructured materials of various compositions,[12] form factors (e.g. thin films[13] and nanoparticles[14]), feature sizes and morphologies.

Block copolymers (BCP) provides another self-assembling building block for creating nanostructures through bottom-up approaches. Block copolymers consist of chemically distinct macromolecular blocks that are covalently joined. When these blocks are amphiphilic, minimization of hydrophilic/hydrophobic interface formation at the block-junction and the volumetric confinement induce phase separation at the length scale of the size of the macromolecules, typically 5-50 nm,[15, 16] resulting in the formation of periodic, ordered structures. Similarly to surfactant self-assembly, these mesophases form ordered nanostructures as shown in Figure 1.3.[17, 18] The mesoscale morphology is determined by the volume fraction of each block, block sequence and degree of chemical incompatibility between blocks, while the length scale is correlated with the overall polymer chain length. In a similar fashion to the surfactant template co-assembly, sol-gel precursors or nanoparticles tailored to interact favorably
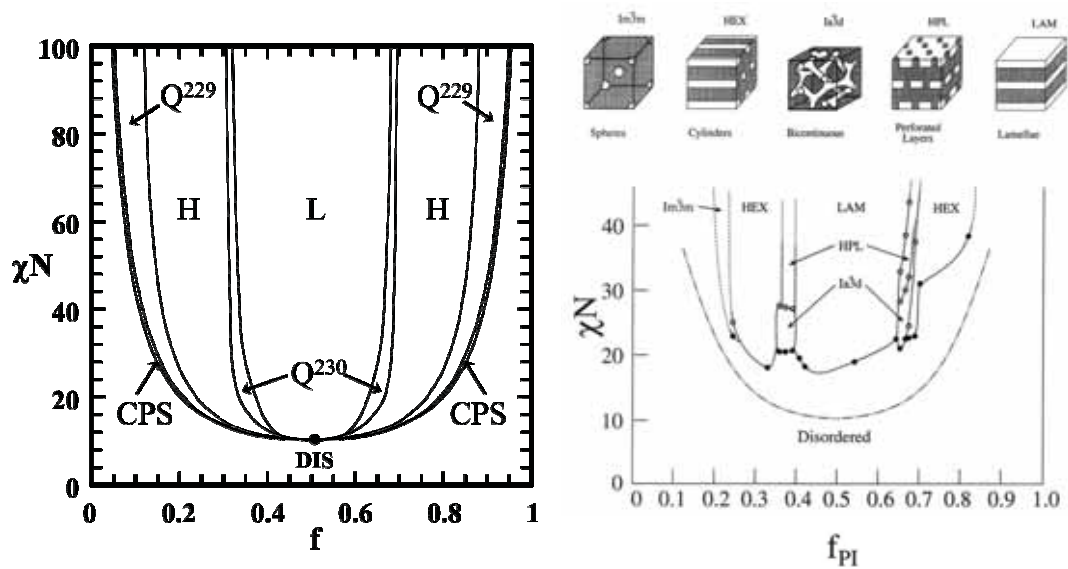
Figure 1.3. (Left) Morphology diagram of an ideal diblock copolymer via self-consistent field theory calculations. Reproduced from Cochran *et al*. with permission.[17] (Right) Experimental morphology diagram of a poly(styrene-*block*-isoprene) block copolymer. Top schematics show the structures in a cell. Reproduced from Khandpur *et al*. with permission.[16]
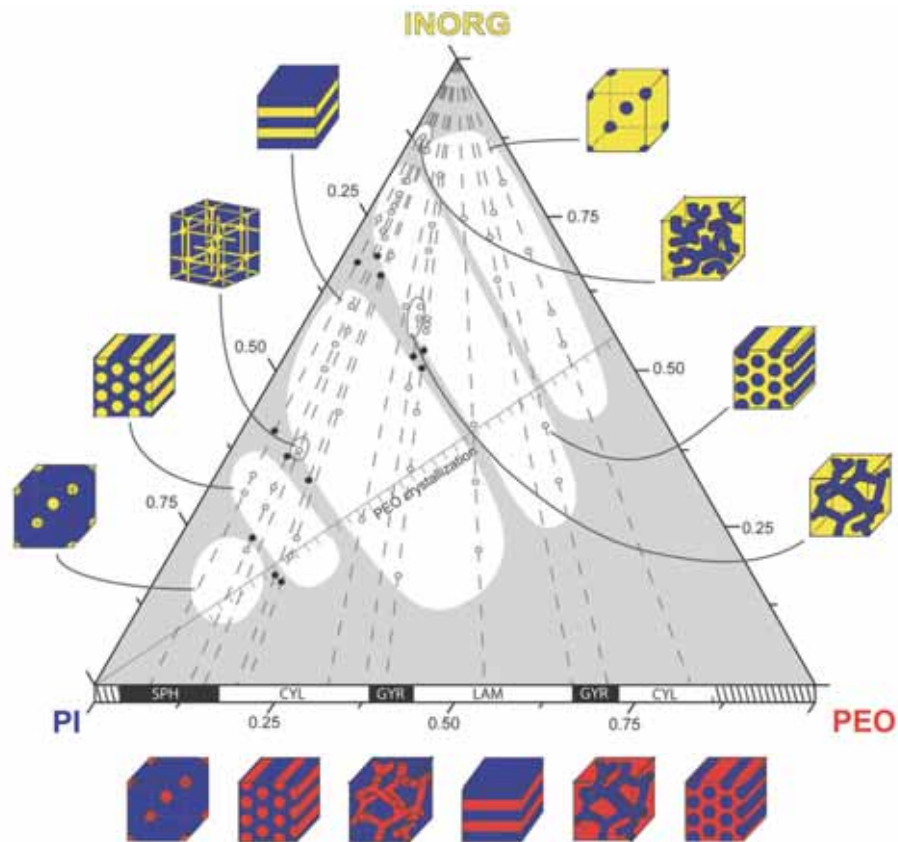
Figure 1.4. Poly(isoprene-*block*-ethylene oxide)/aluminosilicate sol ternary morphology diagram. Reproduced from Garcia *et al*. with permission.[18]

with one block of the block copolymer can be incorporated into the BCP mesophases to form polymer-inorganic hybrids (Figure 1.4).[19-21]

A fundamental difference between lyotropic (*e.g.* surfactant) and thermotropic (*e.g.* BCP) liquid crystals is the participation of solvents in the formation of mesophases. In the surfactant LLCs, thermodynamic equilibrium structures are determined through minimization of overall surface energy, and the majority of the volume that occupies the structure is filled with solvent, resulting in sometimes complex surface patterns.[22] In contrast, BCP chains must extend to the core of the structure to fill the volume, which constitutes a loss in available chain conformational entropy and thus contributes to the systems free energy.[23]

The above building blocks provide nanoscale structure control in surfactant- and polymer-inorganic hybrid materials when forming near-thermodynamic equilibrium structures. The aim of this dissertation is to take these building blocks and to explore synthesis routes to generate organic-inorganic hybrid materials with specific nanostructures. After synthesis, these nanomaterials are characterized by a combination of imaging and scattering techniques.

Analytical toolbox for nanoscale structural characterization

Characterization of nanoscale structures, unlike bulk materials, is non-trivial due to the diffraction limit for visible light. Increasing levels of complexities in chemistry, morphology and length scale compound challenges for accurate assignment of structural features. Two categories of techniques are commonly employed for nanoscale feature characterizations: real-space and reciprocal-space techniques.

In real-space imaging, electromagnetic waves such as high-energy electron beams or hard x-rays are applied on the sample, and the signals from the sample (attenuated transmission signals, scattered electron beam signals, or generated secondary electrons) are collected to reconstruct images of the sample. The short wavelengths of these beams push the diffraction limit down to sub-nm length scales. Transmission electron microscopy (TEM), scanning transmission electron microscopy (STEM), and scanning electron microscopy (SEM) are examples of real-space imaging techniques. While the information obtained is intuitively easier to understand than in reciprocal techniques, the fields of view and thus the amount of materials that can be analyzed with such techniques are usually limited.

On the other hand, high-energy beams can be used to form diffractograms around the beam center by azimuthally integrating the signal scattering intensity around the direct beam, which will yield reciprocal space information of the materials. Such scattering techniques are particularly powerful for materials having long-range order due to the rise of structure factors, but can be used to measure the ensemble form factors and correlation length in locally ordered materials as well. Small-angle X-ray scattering, X-ray diffraction, and selected area electron diffraction are commonly used to obtain reciprocal space images.

Outline of this dissertation

The outline of this dissertation is as follows:

Chapter 1, the current chapter, introduces the readers to the field of nanostructure synthesis using bottom-up approaches and the characterization methods for such materials.

Chapter 2 discusses one aspect of structural complexity, namely multiple nano-sized compartments within a single particle, through synthesis and characterization of multicompartment mesoporous silica nanoparticles. Surfactant coassembly with sol-gel silica precursors leads to the synthesis of locally amorphous, but mesoscopically epitaxially branched silica nanoparticles. The synthesis protocol, characterization, and proposal for possible mechanisms are detailed.

Chapter 3 discusses another aspect of structural complexity, namely the co-assembly of ligand-stabilized platinum nanoparticles (Pt NPs) with block copolymers into nanostructured NP/BCP hybrid materials.

Chapters 4 and 5 discuss another aspect of structural complexity, namely the synthesis of hierarchically porous nanomaterials. Poly(styrene-*block*-ethylene oxide) mixed with oligomeric polyethylene oxides are self-assembled into hierarchical structures, followed by rinsing of the oligomers with protic solvents to yield hierarchically porous polymeric scaffolds. Synthesis parameters are explored affecting the final structures obtained by this synthesis method, termed Spinodal decomposition-Induced Meso-/Macrophase separation PLus Extraction by rinsing (SIM^{2}PLE).

Chapter 6 concludes this dissertation by reflecting on the findings of the various sections in light of possible future directions that could be pursued by subsequent students.

REFERENCES

1. Eichelbaum, M.; Rademann, K.; Muller, R.; Radtke, M.; Riesemeier, H.; Gorner, W., *Angew. Chem., Int. Ed.* **2005,** *44* (48), 7905.
2. Fahlman, B. D., *Materials chemistry*. 2nd ed.; Springer: Dordrecht ; New York, 2011; p xi, 736 p.
3. Saranathan, V.; Osuji, C. O.; Mochrie, S. G. J.; Noh, H.; Narayanan, S.; Sandy, A.; Dufresne, E. R.; Prum, R. O., *Proc. Natl. Acad. Sci. U. S. A.* **2010,** *107* (26), 11676.
4. Weiner, S.; Wagner, H. D., *Annu Rev Mater Sci* **1998,** *28*, 271.
5. Autumn, K.; Liang, Y. A.; Hsieh, S. T.; Zesch, W.; Chan, W. P.; Kenny, T. W.; Fearing, R.; Full, R. J., *Nature* **2000,** *405* (6787), 681.
6. Sanchez, C.; Arribart, H.; Guille, M. M. G., *Nat. Mater.* **2005,** *4* (4), 277.
7. Israelachvili, J. N., *Intermolecular and surface forces*. 3rd ed.; Academic Press: Burlington, MA, 2011; p xxx, 674 p.
8. Brinker, C. J.; Lu, Y. F.; Sellinger, A.; Fan, H. Y., *Adv. Mater.* **1999,** *11* (7), 579.
9. Chiola, V.; Ritsko, J. E.; Vanderpool, C. D. Process for producing low-bulk density silica. U. S. Patent. 3,556,725, 1971.
10. Yanagisawa, T.; Shimizu, T.; Kuroda, K.; Kato, C., *Bull. Chem. Soc. Jpn.* **1990,** *63* (4), 988.
11. Kresge, C. T.; Leonowicz, M. E.; Roth, W. J.; Vartuli, J. C.; Beck, J. S., *Nature* **1992,** *359* (6397), 710.
12. Huo, Q. S.; Margolese, D. I.; Ciesla, U.; Feng, P. Y.; Gier, T. E.; Sieger, P.; Leon, R.; Petroff, P. M.; Schuth, F.; Stucky, G. D., *Nature* **1994,** *368* (6469), 317.
13. Lu, Y. F.; Ganguli, R.; Drewien, C. A.; Anderson, M. T.; Brinker, C. J.; Gong, W. L.; Guo, Y. X.; Soyez, H.; Dunn, B.; Huang, M. H.; Zink, J. I., *Nature* **1997,** *389* (6649), 364.
14. Grun, M.; Lauer, I.; Unger, K. K., *Adv. Mater.* **1997,** *9* (3), 254.
15. Leibler, L., *Macromolecules* **1980,** *13* (6), 1602.
16. Bates, F. S.; Fredrickson, G. H., *Annu. Rev. Phys. Chem.* **1990,** *41* (1), 525.
17. Floudas, G.; Vazaiou, B.; Schipper, F.; Ulrich, R.; Wiesner, U.; Iatrou, H.; Hadjichristidis, N., *Macromolecules* **2001,** *34* (9), 2947.
18. Cochran, E. W.; Garcia-Cervera, C. J.; Fredrickson, G. H., *Macromolecules* **2006,** *39* (7), 2449.
19. Garcia, B. C.; Kamperman, M.; Ulrich, R.; Jain, A.; Gruner, S. M.; Wiesner, U., *Chem. Mater.* **2009,** *21* (22), 5397.
20. Templin, M.; Franck, A.; DuChesne, A.; Leist, H.; Zhang, Y. M.; Ulrich, R.; Schadler, V.; Wiesner, U., *Science* **1997,** *278* (5344), 1795.
21. Yang, P. D.; Zhao, D. Y.; Margolese, D. I.; Chmelka, B. F.; Stucky, G. D., *Nature* **1998,** *396* (6707), 152.
22. Han, Y.; Zhang, D. L.; Chng, L. L.; Sun, J. L.; Zhao, L.; Zou, X. D.; Ying, J. Y., *Nature Chem.* **2009,** *1* (2), 123.
23. Matsen, M. W.; Bates, F. S., *Macromolecules* **1996,** *29* (23), 7641.

CHAPTER 2

MULTICOMPARTMENT MESOPOROUS SILICA NANOPARTICLES WITH

BRANCHED SHAPES FROM SURFACTANT COASSEMBLY[*]

Abstract

    We report a one-pot synthesis method for mesoporous silica nanoparticles (MSNs) containing both cubic and hexagonally structured compartments within one particle. These multicompartment MSNs (multi-MSNs) consist of a core with cage-like cubic mesoporous network morphology and up to four branches with hexagonally packed cylindrical mesopores epitaxially growing out of the vertices of the cubic core. Particle structure is investigated using a combination of transmission electron microscopy and small-angle x-ray scattering while pore characteristics are assessed using nitrogen sorption measurements. The extent of cylindrical mesostructure growth is controlled through concentration variation of ethyl acetate in the initial mixture. Possible nucleation and growth processes leading to this particle morphology are discussed. Results suggest that the use of epitaxial growth relations may allow synthesis of mesostructured nanoparticles with well-controlled branched architectures and shapes.

Since their discovery,[1, 2] mesoporous silica materials have attracted widespread interest due to the versatility in pore structure, surface chemistry and macroscopic form (particles, coatings or bulk materials). A variety of mesostructures in mesoporous silica have been explored, including hexagonal, cage-like cubic, cubic bicontinuous and platelet ordered structures as well as, most recently, dodecagonal quasicrystalline structures.[3, 4] Mesoporous silica nanoparticles (MSNs) offer a particularly interesting materials platform owing to the large surface area, pore volume, the ability to functionalize outer and/or inner surfaces, as well as the tunability of pore geometry through coassembly or pore swelling agents.[5, 6] Inspired by multi-compartment nanoparticles recently described from self-assembling designer soft macromolecular materials,[7-9] we started to explore the possibility of synthesizing multi-compartment mesoporous silica nanoparticles (multi-MSNs) based on the existing library of geometrical variations of the silica pore mesostructure.

The field of solution-grown semiconductor nanoparticle synthesis provides a clue of how to possibly accomplish such architectures. Here nanoparticles have been extensively studied with polymorphic *atomic structures* which are *epitaxially* attached at the interface from a core, leading to branched inorganic nanostructures with well-defined and characteristic shapes such as tetrapods or even dendrimers.[10-12] Rather than epitaxy from atomic structures, *mesostructural epitaxy* exists in mesoporous silica, e.g. for various cubic lattices[13-16] as well as between $Pm\bar{3}n$ and 2D hexagonal lattices.[17, 18] The question we will address in the following is how in low molar mass surfactant coassembly such mesostructural epitaxy can be employed to generate multicompartment mesoporous silica nanoparticles with branched shapes, in which the branches exhibit different pore geometries than the core, based on different mesostructural lattices. Results may open up the translation of concepts from
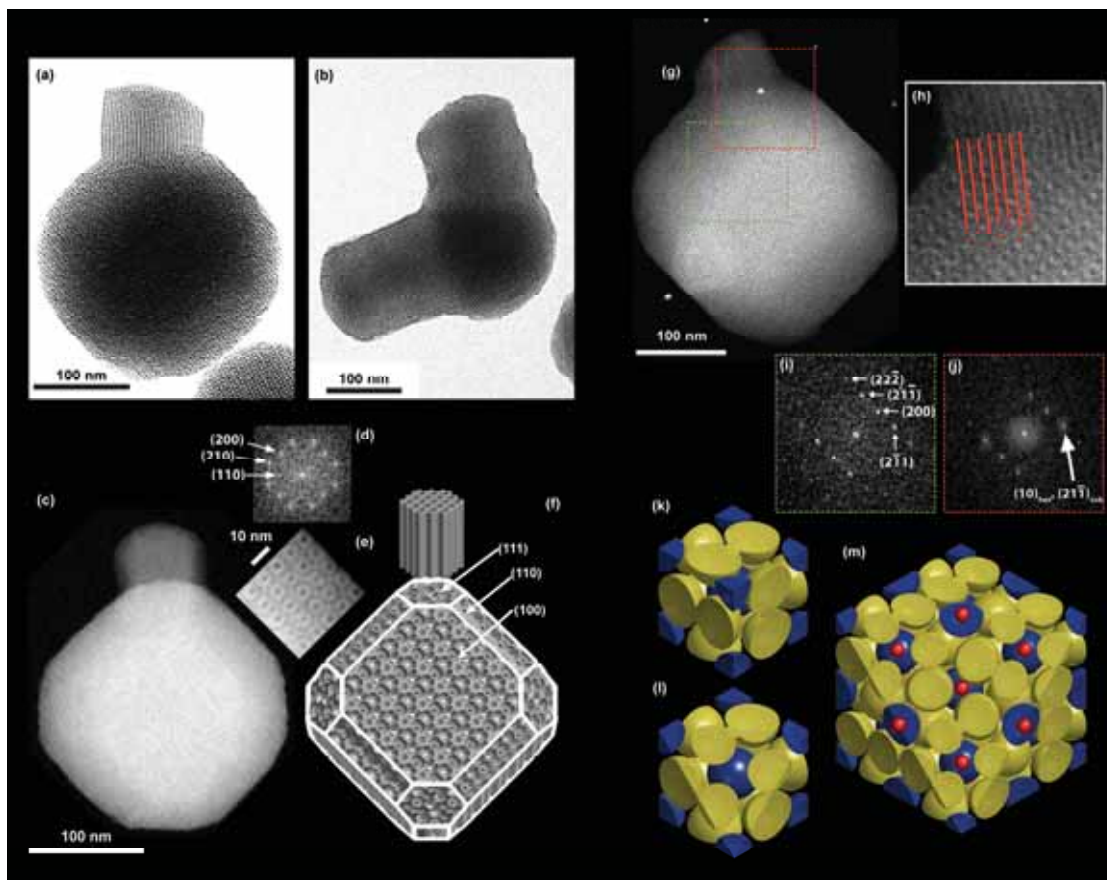
Figure 2.1. Geometrical description of branched, multicompartment mesoporous silica nanoparticles (multi-MSNs). (a) BF-TEM image of a multi-MSN having a branch with hexagonal pore structure emanating from one corner of the mesoporous silica nanoparticle core with cubic pore structure. (b) BF-TEM image of a multi-MSN showing two hexagonal branches emanating from two corners of the cubic core. (c) HAADF-STEM image of a multi-MSN showing the characteristic (100) projection of the cubic particle core and one branch growing out at the top. (d) Fast Fourier transform (FFT) of the entire cubic core part of the image in Figure 2.1c showing spots consistent with the $Pm\bar{3}n$ symmetry. (e) Zoomed image of the top right edge of the particle in Figure 2.1c exhibiting the characteristic pattern from the cage-like structure. (f) Schematics of a model multi-MSN showing characteristic features of the cubic core and emanating hexagonal branch (please note that the cubic pore dimension relative to the particle size is not to scale). Miller indices for some of the representative facets are provided as a visual guide (see Supporting Information Figure 2.S1 for details). (g) HAADF-STEM image of a multi-MSN exhibiting the (110) projection of the cubic particle core. Note that in this projection the cylindrical pores in the branch are clearly visible. (h) Magnified image of the connecting region between the cubic core and hexagonal branch in Figure 2.1g. As visual guides, red lines connect the hexagonal pores (dark lines seen right above the red lines) with the projected vacancies in the cubic micellar structure as indicated by red dots, thus visually demonstrating the structural registry/epitaxy. (i) FFT of the cubic core region in Figure 2.1g (green box) exhibiting sharp reflexes consistent with the (110) zone axis projection of the $Pm\bar{3}n$ symmetry. (j) FFT of the connected region in Figure 2.1g (red box) showing an overlap between the sharp cubic lattice (211) reflexes identical to Figure 2.1i and the diffuse spots corresponding to the 2D hexagonal lattice. (k-m) Model visualization of the epitaxial relationship of mesopores at the interface of (111) $Pm\bar{3}n$ cubic / (0001) $P6mm$ hexagonal planes. (k) Unit cell of the $Pm\bar{3}n$ cage-like structure exhibiting the BCC lattice micelles (represented as blue spheres) and pairs of micelles on the faces (represented as yellow spheres). (l) (111) plane cut of a single unit cell exposing the alignment of the central blue sphere with respect to the three neighboring yellow spheres. (m) (111) plane cut of a 2x2x2 lattice additionally showing the positions of expected hexagonal channels as small red dots growing vertically out of this plane.

12

nanocrystal growth in terms of nanoparticle shape and structure control to locally-amorphous, mesoscopically ordered nanoparticle formation.

We focused on the effect of ethyl acetate (EtOAc) concentration upon nanoparticle morphology in the synthesis of highly aminated cubic MSNs with cage-like pore structure consistent with $Pm\overline{3}n$ symmetry.[19,20] We observed that when EtOAc concentration was increased, mesoporous silica branches with hexagonal cylinder pore structure grew from specific facets of the cubic MSN cores (Figure 2.1a,b). Bright field transmission electron microscopy (TEM) images already suggested that these two parts or "compartments" of the nanoparticles have a well-defined structural relation when viewed along the [110] zone axis (Figure 2.1a). Furthermore, it was observed that some particles possessed multiple branches (Figure 2.1b). High-angle annular dark field scanning TEM (HAADF-STEM) images of multi-MSNs along the [100] zone axis (Figure 2.1c) showed the characteristic four-fold internal structure consistent with the faceted overall particle shape. Fast Fourier transform (FFT) patterns of the HAADF-STEM image exhibited spots for (110), (200) and (210) planes, consistent with the peak extinction conditions of $Pm\overline{3}n$ symmetry (Figure 2.1d). Closer inspection of the particle in 1c clearly revealed the corresponding characteristic four-fold internal patterns consistent with a cage-like structure (Figure 2.1e). Figure 2.1f depicts the corresponding model schematic viewed from a similar angle as in Figure 2.1c. Note that although the size of micellar pores vs. overall particle is modified in this model in order to better show the internal structure, the external shape of the particle in 1c is consistent with the model in 1f where the cube is truncated at its corners with (111) planes and its sides with (110) planes. Occasionally the emanating hexagonal branches are also observed to be faceted along the $(10\overline{1}0)$ (see Supporting Information, Figure 2.S1), coincident with (110) planes on the cubic core, which provided basis for determining the truncating planes in the

model. When HAADF-STEM images were obtained along the [110] zone axis (Figure 2.1g) of the cubic center, the internal linear pore structure of the hexagonal branch was clearly observed. Figure 2.1h shows a magnified image of the connecting region between the cubic core and the branch. Red lines represent extensions of the cylindrical pores of the hexagonal branch and are in registry with the micellar pores of the cubic core depicted as red dots, visually supporting an epitaxial relationship between the mesostructures of the two compartments. While FFT of the cubic core region showed spots corresponding to the $Pm\overline{3}n$ peak positions with the (110) zone axis (Figure 2.1i), FFT of the connected region showed an overlap of relatively sharp (211) spots from the cubic lattice and relatively diffuse (10) spots from the 2D hexagonal lattice, also consistent with an epitaxial relationship between the two structures (Figure 2.1j). This epitaxial relationship can be modeled by a sphere-to-rod transition of micelles as illustrated in Figure 2.1k-m. The $Pm\overline{3}n$ cage-like cubic structure is composed of a body-centered cubic arrangement of micelles plus pairs of micelles on each cubic face (Figure 2.1k). Sectioning the unit cell at the (111) plane, each blue micelle resides on top of a set of three yellow micelles, making a locally layered order (Figure 2.1l). Figure 2.1m shows the top-view schematic of where the 2D hexagonal channels are placed with respect to the (111) cubic planes: the hexagonal lattice of the blue micelles are in registry with the hexagonally ordered channels, consistent with the observations made in Figure 2.1h as highlighted by the red lines and dots.

By increasing the concentration of ethyl acetate in the initial mixture, the relative amount of hexagonal versus cubic mesostructure can be controlled (Figure 2.2). Low magnification TEM images of MSNs synthesized from EtOAc concentrations of 91 mM, 274 mM, and 457 mM, respectively (Figure 2.2a,d,g) show hexagonally ordered branches only at elevated concentrations (Figure 2.2a only shows
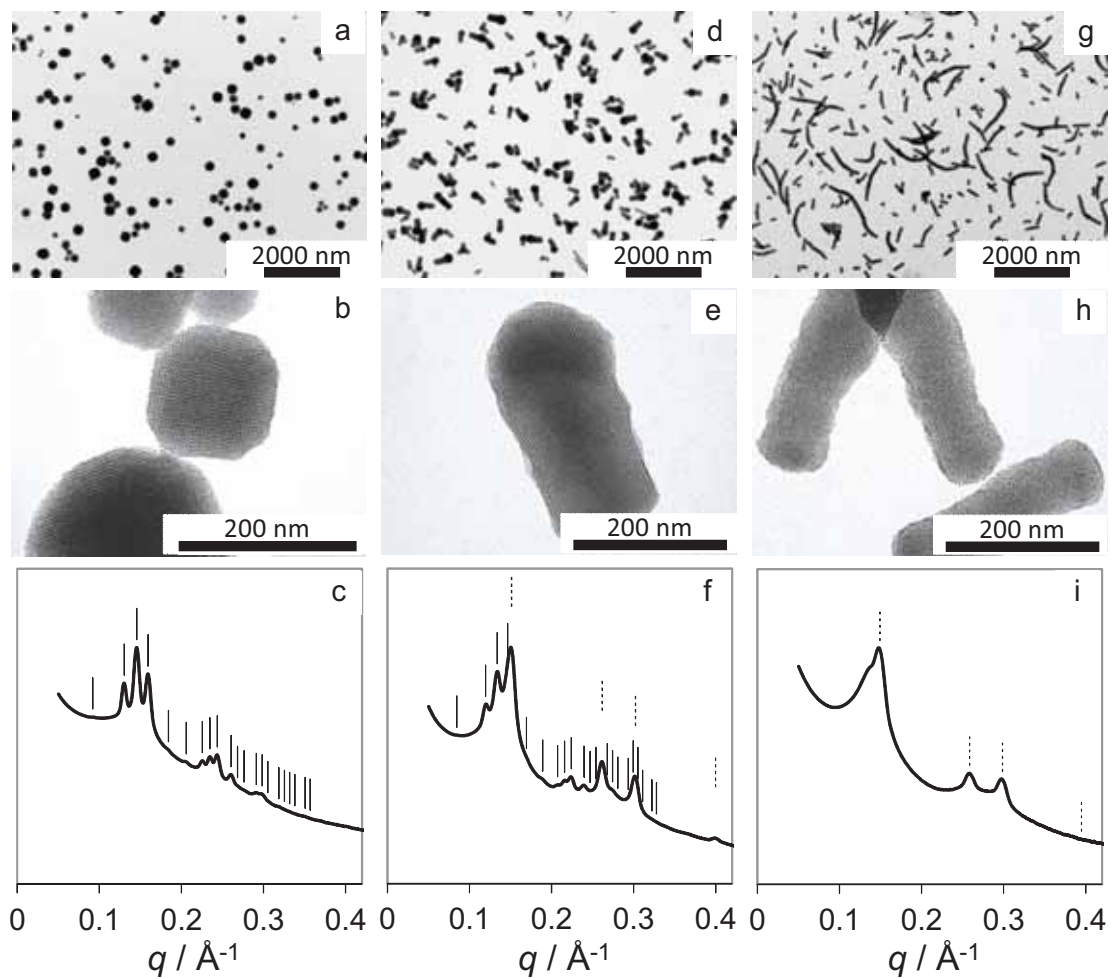
Figure 2.2. TEM images at two different magnifications (a,d,g and b,e,h) and corresponding SAXS patterns (c,f,i) of aminated MSNs prepared from 91 mM (a-c), 274 mM (d-f) and 457 mM (g-i) ethyl acetate concentration. In the SAXS patterns expected peak positions from cubic and hexagonal lattices are indicated with solid and dotted lines, respectively. Data for 91 mM ethyl acetate is adapted from Ref. 19.

15

cubic MSNs). The length of these hexagonally ordered branches increases with increasing EtOAc concentration (compare Figures 2d and g). In Figure 2.2d the majority of multi-MSNs from 274 mM EtOAc has short hexagonal branches with diameters equal to or smaller than the cubic core size. In the 457 mM sample, these branches grow to rods as long as 2 microns, often in a non-straight fashion (Figure 2.2g). Higher magnification images show that the 274 mM nanoparticles (Figure 2.2e) consist of a hexagonal branch attached to a core with cage-like cubic structure identical to the cubic MSN shown in Figure 2.2b. At 457 mM (Figure 2.2h), for most of the rods we could not find a cubic core portion, suggesting structural transformation from cubic to hexagonal mesostructure. Small angle X-ray scattering patterns (Figures 2c,f,i) of these samples averaging over macroscopic material volumes corroborate the more local TEM observations in that the relative intensities of the peaks consistent with *P6mm* 2D hexagonal symmetry increase at the expense of those consistent with $Pm\bar{3}n$ symmetry: The cubic MSN sample from 91 mM EtOAc shows reflections consistent with $Pm\bar{3}n$ symmetry and 9.65 nm unit cell size (Figure 2.2c).[19] At 274 mM EtOAc a superposition is observed of reflections consistent with 2D hexagonal symmetry and 4.80 nm unit cell size with reflections consistent with $Pm\bar{3}n$ symmetry and 10.5 nm unit cell size (Figure 2.2f). The (211) reflection for the cubic lattice coincides closely with the (10) reflection for the hexagonal lattice, with lattice mismatch of ~3%, further suggesting an epitaxial relation between the two lattices. The pore-to-pore spacing for the hexagonal branches/compartments in the 274mM multi-MSNs are 8 % larger than those for purely hexagonal MSNs synthesized in the absence of APTES and 3-4 % larger than those synthesized in the presence of varying amounts of APTES (see Supporting Information, Figure 2.S2).[20, 21] On the other hand, the (211) spacing of the cubic core is 4.95 nm, indicating that the 2D hexagonal lattice is stretched to accommodate for the lattice mismatch. At 457 mM EtOAc reflections

consistent with $Pm\bar{3}n$ have almost disappeared, leaving mostly those consistent with 2D hexagonal symmetry and 4.86 nm pore-to-pore spacing (Figure 2.2i). The increase in spacing as a function of EtOAc concentration for both cubic and hexagonal structures (as shown in Figure 2.S2) is likely associated with swelling of the hydrophobic micelle cores with EtOAc, *vide infra*.

In order to establish a structure-property relationship for these three batches of MSNs, nitrogen sorption measurements were performed (Figure 2.3). All three samples showed characteristic type IV isotherms, with the capillary condensation of mesopores occurring at $P/P_0 \sim 0.3$. The large nitrogen uptake at $P/P_0 > 0.9$ corresponds to condensation in the interstitial spaces of the particles. We note that the multi-MSNs containing more hexagonal pores, i.e. from higher amounts of EtOAc, exhibited a sharper condensation behavior at lower relative pressure, $P/P_0 \sim 0.3$. This is reflected in the pore size distribution calculated using non-local density functional theory (NLDFT) (Figure 2.3 inset). While the cubic MSN showed a broad distribution of pore sizes centered at 3.6 nm and extending up to 4.5 nm, multi-MSNs with increasing amount of hexagonal pores exhibited narrower pore size distributions around 3-4 nm. This sorption behavior is consistent with the cage-like pore geometry with constricted windows between the cages in the cubic core and the straight channel geometry in the hexagonal branches.[22]

The above trend in MSN structure as a function of EtOAc sheds light on a possible growth mechanism of hexagonal branches emanating from the cubic MSN cores. EtOAc is known over time to hydrolyze in basic conditions into ethanol and acetic acid, which quenches an equimolar amount of base and thus lowers the pH of the reaction mixture.[23] At room temperature, the kinetic constant of ester hydrolysis is measured to be 5.4 L mol^{-1} min^{-1}.[24] Increasing the EtOAc concentration from 91 mM to 457 mM while keeping the concentration of base (ammonium hydroxide and
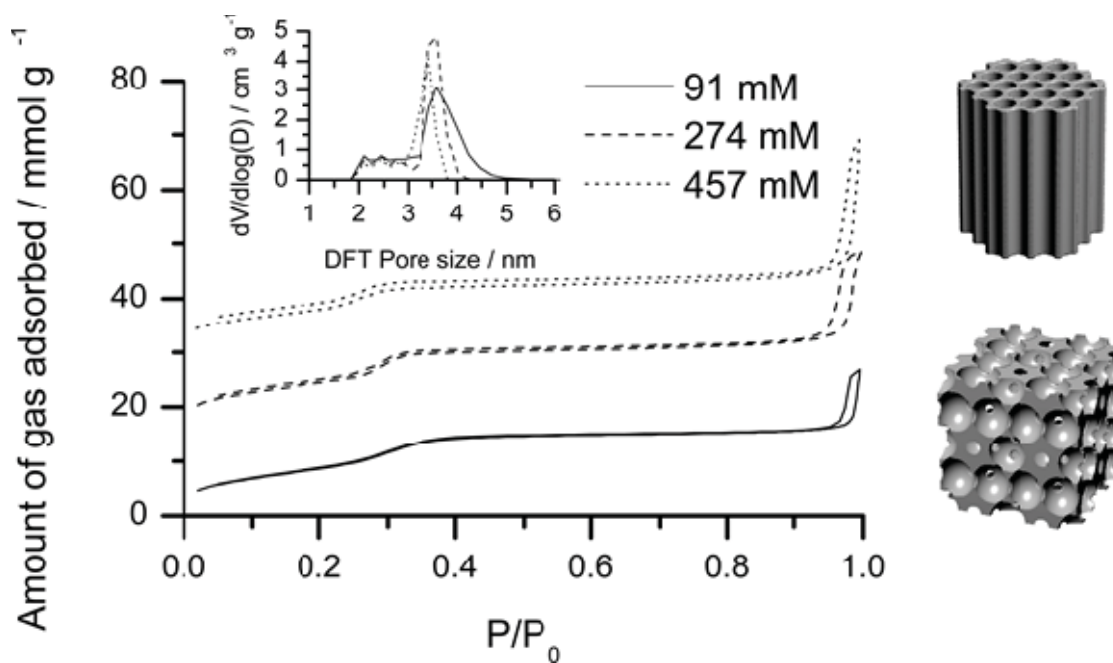
Figure 2.3. Nitrogen sorption isotherms of MSNs synthesized with varying EtOAc concentrations. Isotherms for 274 mM and 457 mM multi-MSNs are offset along the y-axis by 15 and 30 mmol/g, respectively. The inset shows pore size distributions obtained from non-local density functional theory (NLDFT) calculations based on the respective absorption branches. The models on the right provide a direct comparison of the pore structures of hexagonal and cubic lattices.

APTES) constant at ~ 200 mM imposes two effects on the solution pH. First, it induces an increase in the rate of pH drop. This effect is linearly dependent on the initial EtOAc concentration assuming first-order hydrolysis kinetics. Second, it lowers the final pH of the solution. This latter effect is asymptotic with respect to the initial EtOAc concentration, for the hydrolysis reaction significantly slows down as the hydroxide ions are quenched. In fact, the final pH values for solutions with EtOAc concentrations above that of the base (200 mM) are expected to be nearly identical, since excess EtOAc cannot participate in hydrolysis and base quenching. As pH decreases below 10, the predominant state of the amine group of APTES becomes positively charged, which repels against the charged head groups of the structure-directing hexadecyltrimethylammonium bromide (CTAB) cations. This change in the charge state of APTES may induce a structural change in the CTAB micelles. While at high pH uncharged APTES can insert between CTAB head groups, charge repulsion prevents this swelling at lower pH, thus leading to changes in micelle curvature. It is this change in micelle curvature that has been suggested as the main factor driving a morphological change from cage-like cubic to hexagonal, in agreement with the observed transition from a cubic core to hexagonally structured branches growing off of this core in the present study.[22, 25] The room-temperature synthesis protocol used here enables fine-tuning of the sol-gel kinetics against pH change, providing control over the multi-MSN morphology. In energy dispersive spectroscopy (EDS) derived elemental maps, we did not observe significant variations in the amine content for the cubic versus hexagonal parts of the nanoparticles (see Supporting Information, Figure 2.S3), suggesting high inclusion of APTES in both cubic and hexagonal pore walls.

Rather than only on one facet, nucleation of hexagonally mesostructured compartments on the cubic MSN cores can occur on multiple facets of the cubic core, as became particularly apparent when intermediate concentrations of EtOAc were
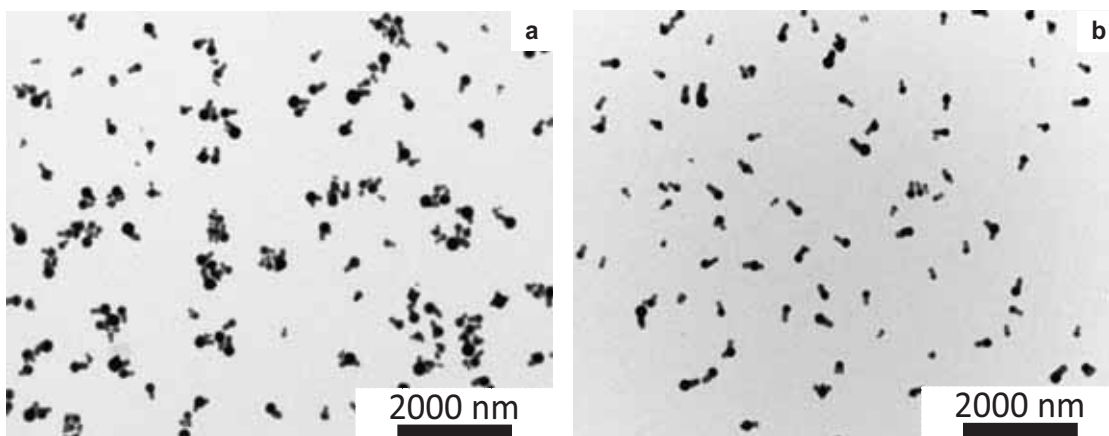
Figure 2.4. Low magnification TEM images of aminated MSNs prepared from (a) 137 and (b) 183 mM ethyl acetate.

employed. While for EtOAc concentrations of 137 mM and 183 mM most particles still only showed one hexagonal branch per cubic core, a fraction had one, two, three and even four branches (Figure 2.4a,b). Close TEM examination of these multi-MSNs revealed that the angles at which the hexagonally structured branches grow were consistent with models where hexagonal branches grow in <111> directions off of the cubic core, further consistent with the epitaxial relationship (compare TEM images with corresponding models in Figure 2.5a-d and f-i, respectively). Interestingly, no MSN with a number of branches larger than four was observed in our samples, while we did observe some multi-MSNs in which hexagonal rods that grew in two distinct directions merged into one rod with a large diameter (compare TEM image/model in Figure 2.5e/j). On a truncated cubic structure, there are eight (111) equivalent surfaces corresponding to the number of cube vertices, giving eight equivalent sites for hexagonal branches to form and grow. As a particular branch grows, it may deplete the available silica in its direct vicinity, thus preventing growth of another branch next to it. This is one possible explanation why the vast majority of observed branches had grown on non-nearest (111) core surfaces and why the maximum number of branches observed was only four. We further hypothesize that in the case two nearest neighboring sites nucleate hexagonal branches, geometrical crowding joins the neighboring nuclei as they grow. Such merging and overgrowth of hexagonal rods also reduces the number of rods per particle and increases the rod diameter compared to the core particle size. This may be what lead to the observed structures in the 457 mM EtOAc sample (Figure 2.2g).

In summary, we have demonstrated the successful synthesis of branched multicompartment MSNs containing a cage-like cubic core and branches growing off of the core with hexagonal cylindrical pores. Using a combination of TEM and SAXS experiments an epitaxial relation between the mesostructures of the two compartments
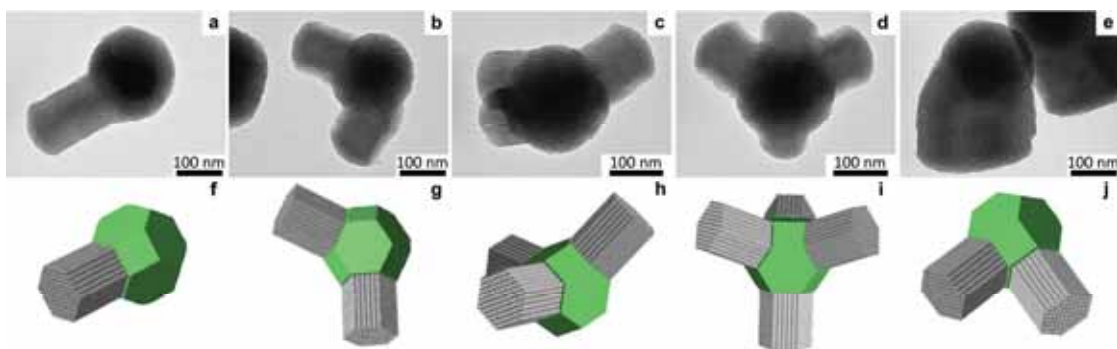
Figure 2.5. TEM images (a-e) and models (f-j) of multicompartment MSNs with different numbers of branches with hexagonally arranged cylindrical mesopores epitaxially grown from the cubic core (from a particle batch prepared from 183 mM ethyl acetate). (a) 1 arm, (b) 2 arms, (c) 3 arms, (d) 4 arms and (e) two arms merged into one. In the models core cubic compartments are drawn as green truncated cubes, and branches are represented as gray columns. Note that images (f-i) show rods growing from non-neighboring (111) facets, whereas in (j) the two rods are growing from neighboring (111) facets.

was evidenced. With the help of nitrogen sorption measurements a correlation between the specific structure of the nanoparticles and their porosity was established. A simple parameter, namely the ethyl acetate (EtOAc) concentration in the starting synthesis mixture governed the overall fraction of nanoparticle silica with hexagonal cylindrical morphology. Based on our findings a mechanism for the growth of these multicompartment nanoparticles was suggested. The results described here suggest that in analogy to recent developments in nanocrystal synthesis, the use of epitaxial growth relations in the synthesis of locally-amorphous, mesoscopically ordered (silica) nanoparticles may allow access to more complex yet precisely controlled shapes and compositions as well as to assemblies of these nanoparticles with carefully controlled interconnections.

REFERENCES

1.   Yanagisawa, T.; Shimizu, T.; Kuroda, K.; Kato, C., *Bull. Chem. Soc. Jpn.* **1990,** *63* (4), 988.

2.   Kresge, C. T.; Leonowicz, M. E.; Roth, W. J.; Vartuli, J. C.; Beck, J. S., *Nature* **1992,** *359* (6397), 710.

3.   Hoffmann, F.; Cornelius, M.; Morell, J.; Froba, M., *Angew. Chem. Int. Ed.* **2006,** *45* (20), 3216.

4.   Xiao, C. H.; Fujita, N.; Miyasaka, K.; Sakamoto, Y.; Terasaki, O., *Nature* **2012,** *487* (7407), 349.

5.   Vallet-Regi, M.; Balas, F.; Arcos, D., *Angew. Chem. Int. Ed.* **2007,** *46* (40), 7548.

6.   Slowing, II; Vivero-Escoto, J. L.; Wu, C. W.; Lin, V. S. Y., *Adv. Drug Delivery Rev.* **2008,** *60* (11), 1278.

7.   Li, Z. B.; Kesselman, E.; Talmon, Y.; Hillmyer, M. A.; Lodge, T. P., *Science* **2004,** *306* (5693), 98.

8.   Cui, H. G.; Chen, Z. Y.; Zhong, S.; Wooley, K. L.; Pochan, D. J., *Science* **2007,** *317* (5838), 647.

9.   Chandrawati, R.; van Koeverden, M. P.; Lomas, H.; Caruso, F., *J. Phys. Chem. Lett.* **2011,** *2* (20), 2639.

10.   Manna, L.; Milliron, D. J.; Meisel, A.; Scher, E. C.; Alivisatos, A. P., *Nat. Mater.* **2003,** *2* (6), 382.

11.   Yin, Y.; Alivisatos, A. P., *Nature* **2005,** *437* (7059), 664.

12.   Talapin, D. V.; Nelson, J. H.; Shevchenko, E. V.; Aloni, S.; Sadtler, B.; Alivisatos, A. P., *Nano Lett.* **2007,** *7* (10), 2951.

13.   Srinivasu, P.; Lim, S.; Kubota, Y.; Tatsumi, T., *Catal. Today* **2006,** *111* (3-4), 379.

14.   Han, L.; Sakamoto, Y.; Che, S.; Terasaki, O., *Chem. Eur. J.* **2009,** *15* (12), 2818.

15.   Atluri, R.; Bacsik, Z.; Hedin, N.; Garcia-Bennett, A. E., *Microporous Mesoporous Mater.* **2010,** *133* (1-3), 27.

16.   Han, L.; Miyasaka, K.; Terasaki, O.; Che, S. N., *J. Am. Chem. Soc.* **2011,** *133* (30), 11524.

17.   Che, S. N.; Kamiya, S.; Terasaki, O.; Tatsumi, T., *J. Am. Chem. Soc.* **2001,** *123* (48), 12089.

18.   Kamiya, S.; Tanaka, H.; Che, S.; Tatsumi, T.; Terasaki, O., *Solid State Sci.* **2003,** *5* (1), 197.

19.   Suteewong, T.; Sai, H.; Cohen, R.; Wang, S.; Bradbury, M.; Baird, B.; Gruner, S. M.; Wiesner, U., *J. Am. Chem. Soc.* **2011,** *133* (2), 172.

20.   Suteewong, T.; Sai, H.; Bradbury, M.; Estroff, L. A.; Gruner, S. M.; Wiesner, U., *Chem. Mater.,* **2012,** 24 (20), 3895.

21.   Suteewong, T.; Sai, H.; Lee, J.; Bradbury, M.; Hyeon, T.; Gruner, S. M.; Wiesner, U., *J. Mater. Chem.* **2010,** *20* (36), 7807.

22.   Atluri, R.; Sakamoto, Y.; Garcia-Bennettt, A. E., *Langmuir* **2009,** *25* (5), 3189.

23.   Schulz-Ekloff, G.; Rathousky, J.; Zukal, A., *Int. J. Inorg. Mater.* **1999,** *1* (1), 97.

24.   Dittert, L. W.; Higuchi, T., *J. Pharm. Sci.* **1963,** *52* (9), 852.

25.   Ogura, M.; Miyoshi, H.; Naik, S. P.; Okubo, T., *J. Am. Chem. Soc.* **2004,** *126* (35), 10937.

APPENDIX: SUPPLEMENTARY MATERIALS

Experimental Methods

Materials

Hexadecyltrimethylammonium bromide (CTAB, approx. 99%), ethyl acetate (EtOAc, ACS grade), tetraethyl orthosilicate (TEOS, ≥99%, GC), (3-aminopropyl)triethoxysilane (APTES, > 95%), ammonium hydroxide (NH_4OH, 29%), acetic acid (glacial), hydrochloric acid (36.5-38%), ethanol (absolute, anhydrous) and deionized water (Milli-Q, 18.2 MΩ-cm) were used as obtained without further purification.

Synthesis of multicompartment mesoporous silica nanoparticles (multi-MSNs)

Multicompartment mesoporous silica nanoparticles (multi-MSNs) were prepared by increasing the ethyl acetate (EtOAc) concentration of the highly aminated cubic MSNs reported in a previous publication.[1,2] The volumetric ratio in milliliters of chemicals used in the synthesis of cubic MSNs was 1 CTAB (aq):0.045 TEOS:0.055 APTES:0.54 NH_4OH:0.176 EtOAc:27.38 H_2O. For multi-MSNs, EtOAc volume per CTAB (aq) was varied from 0.264 for 137 mM to 0.880 for 457 mM. CTAB solution was gently stirred in a container to which H_2O, EtOAc, NH_4OH, and mixed silanes were added in this order. We note that after EtOAc addition, the mixture was left stirring for a few minutes to let the EtOAc dissolve before adding the rest of the reagents. Five minutes after silane addition was complete, H_2O (7.98 v/v CTABaq) was added and the mixture was left stirring for 24 hours. On completion of the reaction, samples were neutralized with 2 M HClaq, and the MSNs were cleaned of

26

incorporated CTAB micelles with acetic acid as reported previously.[1,2] The particles were redispersed in absolute ethanol or kept dry for storage to prevent further hydrolysis.

In order to determine the surface amine content on the multi-MSN using elemental analysis by energy-dispersive x-ray spectroscopy (EDS), iridium (III) chloride hydrate was used as a contrasting agent according to previous literature.[3]

Characterization

Bright-field transmission electron microscopy (TEM) images were obtained on a Tecnai T12 Spirit microscope, equipped with a LaB_6 source and a SIS Megaview III CCD camera and running at an acceleration voltage of 120 kV. High-angle annular dark field scanning transmission electron microscopy (HAADF-STEM) images and EDS elemental maps were acquired on a Tecnai F20 microscope operating at an acceleration voltage of 200 kV. Hanning-filtered Fast Fourier transform (FFT) images were calculated and analyzed in the Electron Direct Methods (EDM) software suite, version 3.0.

Small-angle x-ray scattering (SAXS) patterns of surfactant-extracted, dried MSN samples were obtained on a home-built rotating anode beamline as well as at the G1 station in Cornell High Energy Synchrotron Source (CHESS).[1,2] For the rotating anode setup, a flight path of 15 cm was used with the CuKα source, while a 40cm flight path with 10 keV x-ray was used in CHESS G1. Two-dimensional patterns obtained on a phosphor-optical fiber coupled CCD were azimuthally integrated to generate the 1D SAXS patterns in the MATLAB software suite.

Nitrogen sorption experiments were performed on a Micromeritics ASAP2020 instrument. Around 10 mg of the samples were degassed at 110-120 °C under vacuum overnight prior to the measurements. Acquired isotherms were analyzed for pore size distribution using the non-local density functional theory (NLDFT) package using a cylindrical geometry and Tarazona's density functional model.

REFERENCES

1.   Suteewong, T.; Sai, H.; Cohen, R.; Wang, S.; Bradbury, M.; Baird, B.; Gruner, S. M.; Wiesner, U., *J. Am. Chem. Soc.* **2011,** 133 (2), 172.
2.   Suteewong, T.; Sai, H.; Bradbury, M.; Estroff, L. A.; Gruner, S. M.; Wiesner, U., *Chem. Mater.,* **2012,** 24 (20), 3895.
3.   Kecht, J.; Schlossbauer, A.; Bein, T., *Chem. Mater.* **2008,** *20* (23), 7207.
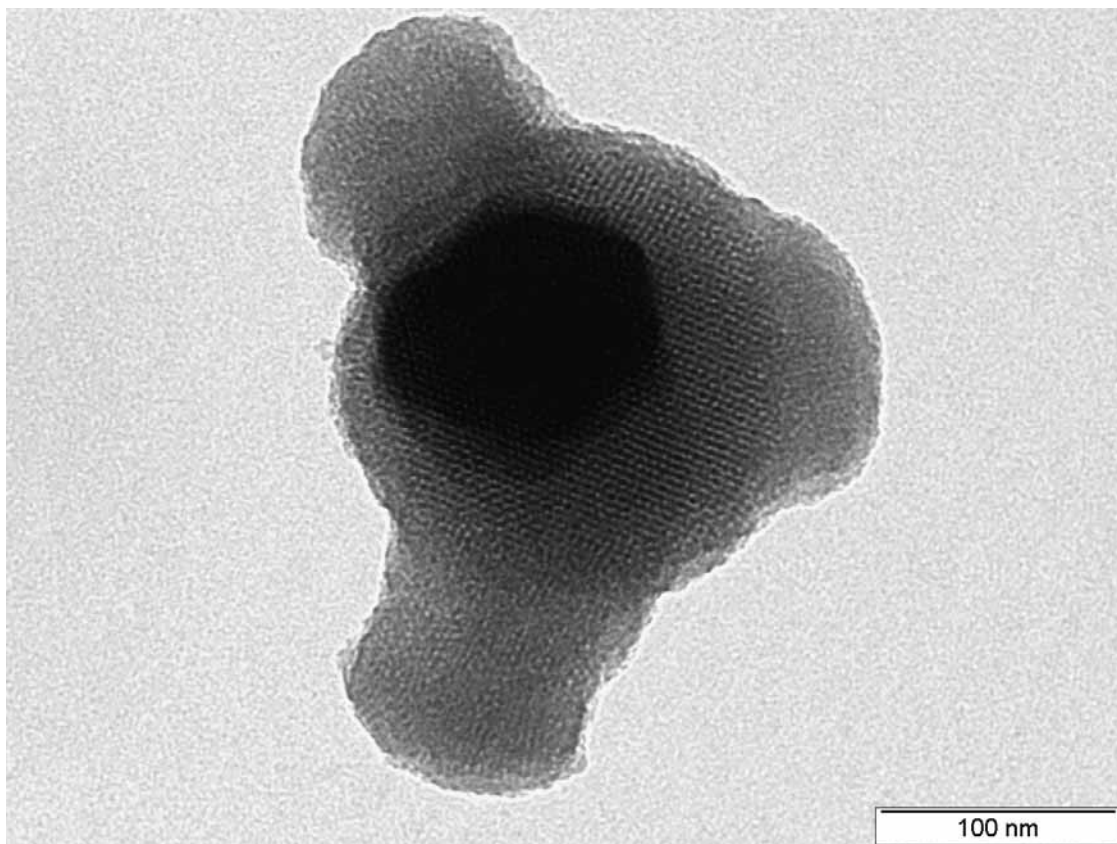
Figure 2.S1. TEM image of a multi-MSN showing one of the four branches (dark domain in the middle) growing in the same direction as the electron beam. Pore alignment geometry inside the hexagonal branch suggests that the external facets are parallel to the [10] direction of the hexagonal lattice, as shown in the model schematic in Figure 2.1d in the main text.
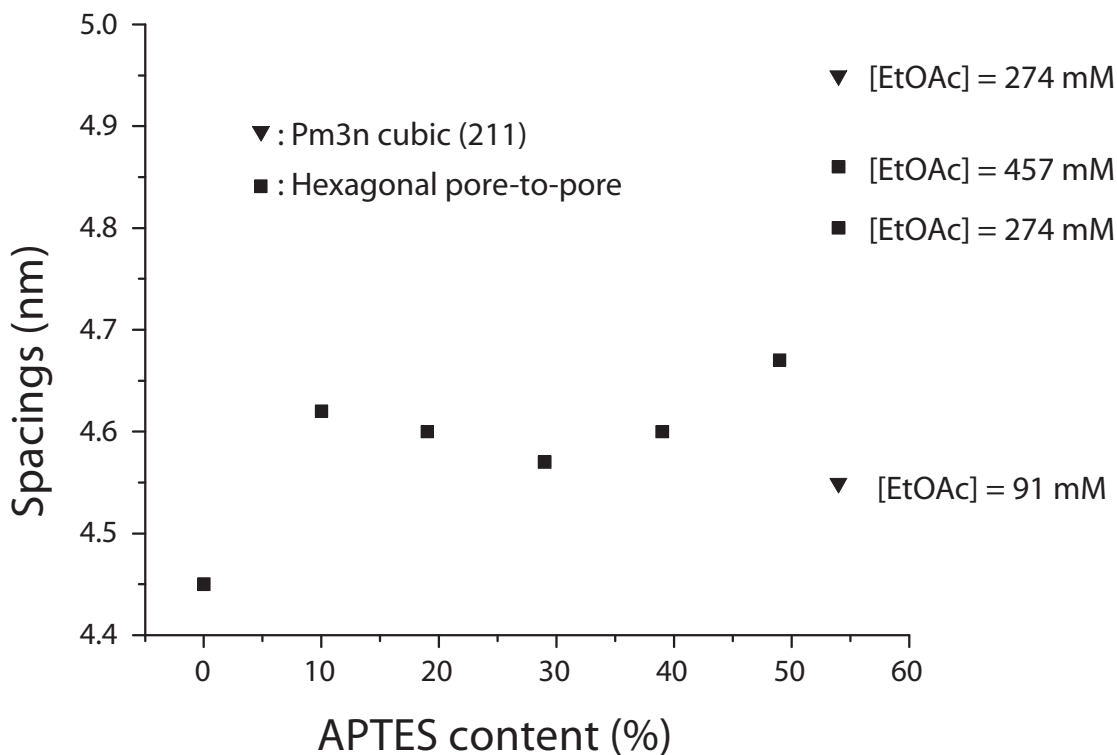
Figure 2.S2. Comparison of hexagonal pore-to-pore (squares) and cubic (211) (triangles) spacings in MSNs for varying amounts of APTES at a constant amount of EtOAc (91 mM), as well as for varying amounts of EtOAc at a constant amount of APTES (54 vol.%; 4 data points on the very right). Data points for 0-49 vol.% APTES in the synthesis feed are from a previous report.[1]
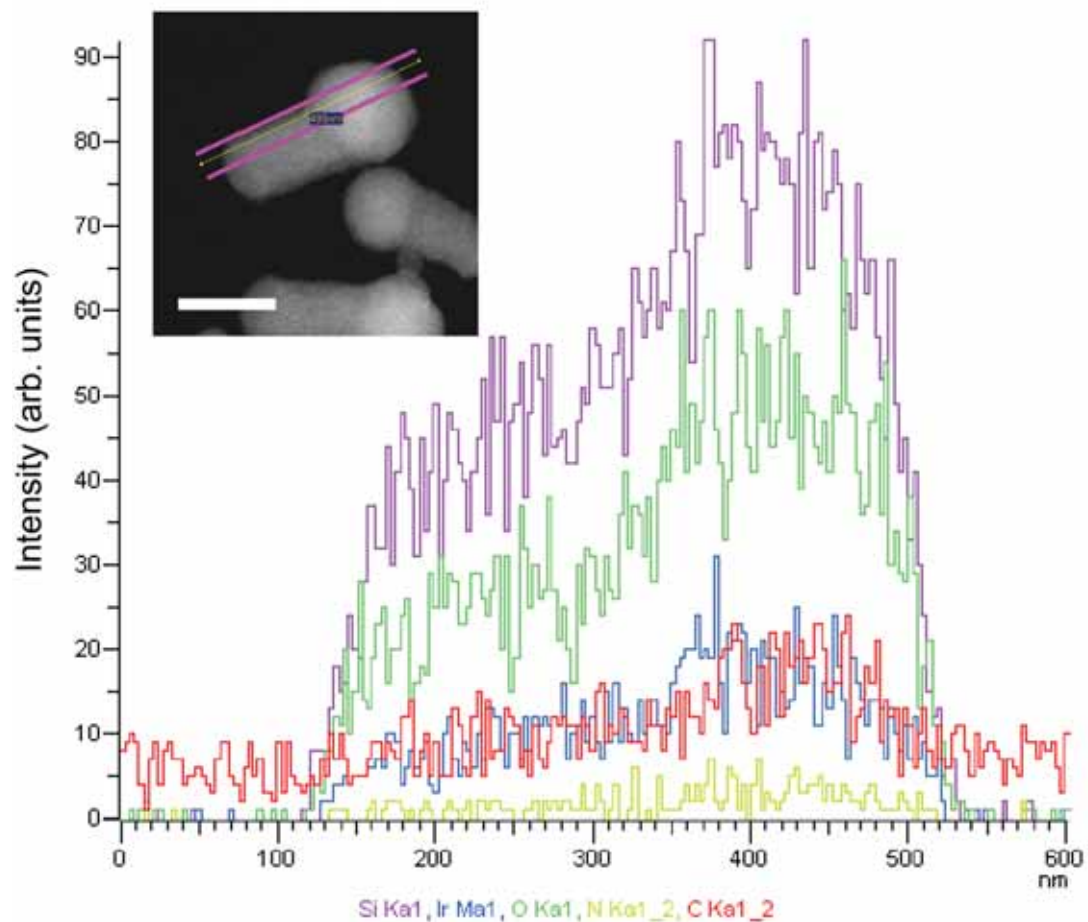
Figure 2.S3. EDS-derived elemental mapping profiles on a line slice of an iridium-stained multi-MSN (see Supporting Information, Experimental Methods). Inset shows the contour along which the spectra were taken. Note that the Si/Ir ratio difference between the hexagonal branch and the cubic center is insignificant, indicating that the amine content in the hexagonal branch and cubic core is the same.

CHAPTER 3

METAL NANOPARTICLE/BLOCK COPOLYMER COMPOSITE ASSEMBLY

AND DISASSEMBLY[*]

Abstract

Ligand-stabilized platinum nanoparticles (Pt NPs) were self-assembled with poly(isoprene-*block*-dimethylaminoethyl methacrylate) (PI-*b*-PDMAEMA) block copolymers to generate organic-inorganic hybrid materials. High loadings of NPs in hybrids were achieved through usage of *N,N*-di-(2-(allyloxy)ethyl)-*N*-3-mercaptopropyl-*N*-3-methylammonium chloride as the ligand, which provided high solubility of NPs in various solvents as well as high affinity to PDMAEMA. From NP synthesis, existence of sub-1 nm Pt NPs was confirmed by high-angle annular dark field scanning transmission electron microscopy (HAADF-STEM) images. Estimations of the Pt NP ligand head group density based on HAADF-STEM images and thermogravimetric analysis (TGA) data yielded results comparable to what has been found for alkanethiol self-assembled monolayers (SAMs) on flat Pt {111} surfaces. Changing the volume fraction of Pt NPs in block copolymer-NP composites yielded hybrids with spherical micellar, wormlike micellar, lamellar and inverse hexagonal morphologies. Disassembly of hybrids with spherical, wormlike micellar, and lamellar morphologies generated isolated metal-NP based nano-spheres, cylinders and sheets, respectively. Results suggest the existence of powerful design criteria for the formation of metal-based nanostructures from designer blocked macromolecules.

[*] Li, Z.; Sai, H.; Warren, S. C.; Kamperman, M. K.; Arora, H.; Gruner, S. M.; Wiesner, U. *Chem. Mater.* **2009**, *21* (23), 5578–5584.

Introduction

Block copolymer (BCP) self-assembly is considered a powerful route to achieve nanoscale (2-50 nm) materials because of its ability to form various periodic structures with tunable length scale.[1-3] BCPs have been used as structure directing agents to incorporate different loadings of functional inorganic species into select blocks of BCPs, resulting in ordered nanostructured organic-inorganic hybrid materials.[4-6] BCPs in hybrids with high inorganic loading can be removed by chemical, photochemical and/or thermal treatments without collapse of the structures, resulting in nanoporous functional materials. This methodology has been successfully applied to various inorganic systems, such as aluminosilicates,[6] orthosilicates,[7-9] transition metal oxides[10,11] and non-oxide ceramics.[12,13] Despite the achievements in the field, synthesizing ordered nanostructured metal hybrids and metals thereof using BCPs remains challenging due to high surface energies of metals. To date, mainly two approaches are being utilized: the first involves *in-situ* metal nanoparticles (NP) synthesis, where BCPs are loaded or swollen by metal precursors prior or after microphase separation, and a subsequent reducing step is applied to transform the metal precursors into metal NPs.[14-19] Different metals (e.g. Au, Pt, Pd, Ag) and polymers (e.g. poly(styrene-*block*-acrylic acid) (PS-*b*-PAA), poly(styrene-*block*-2-vinylpyridine) (PS-*b*-P2VP)) have been used, proving the generality of this approach. Although *in-situ* methods are suitable for thin film applications, loading of the metals is limited by the diffusion of the reagents when applying to bulk materials with larger thickness. The second approach involves *ex-situ* metal NP synthesis. Preformed metal NPs are self-assembled with block copolymers where the NPs are stabilized with tailored surface ligands or functional groups which render them compatible with only one block of the block copolymer.[20-26] Extensive studies of this method have been performed in the last nearly two decades both in thin films and in the bulk. For

example, Au NPs stabilized with alkanethiol groups localized at the interface between a symmetric poly(styrene-*block*-ethylene-*co*-propylene) (PS-*b*-PEP) has been reported by Bockstaller *et al*.[20] Kim *et al*. studied PS-coated Au NPs self-assembled with PS-*b*-P2VP. They found that the addition of NPs increased the effective volume fraction of the PS block and thus induced a lamellar-to-cylindrical phase transition.[21] They also studied the effect of ligand head group density on NPs/polymer interaction.[22,23] Finally, more recently some of us reported the assembly of metal NPs in block copolymer brushes in which NP-BCP interactions are tuned, likewise, by ligand head density.[26]

Most of the work on BCP/metal NP self-assembly has focused on the dilute nanoparticle regime, where the NPs only comprise a small volume fraction of the hybrid material. Achieving hybrid synthesis in the dense nanoparticle regime[27] where NPs comprise the majority volume fraction will provide access to nanostructured organic-metal hybrid materials, as well as to nanoporous metals.[19,28,29] It has been reported in several BCP/NP systems that when the volume fraction of NPs increases, controlled microphase separation of the BCP was disrupted.[30,31] The observed macrophase separation could arise from poor particle solubility in solvents at high concentration, insufficient favorable enthalpic interactions between NPs and BCP as well as unfavorable entropic interactions.[32-34] Moreover, the small volume fraction of the core metal embedded in the corona when using polymer coated NPs leads to small metal loadings in the final material. Thus, in order to achieve BCP/metal NP hybrids with high metal loadings, the metal NPs have to be tailored to fulfill several criteria:[35,36]

1.   NPs should maintain high solubility in polymer-compatible solvents.

2.   There should be sufficient preferential interaction of NPs with one block of the BCP.

34

3.   NP size should be smaller than the radius of gyration of the preferential block.

4.   The ligand should be short enough to ensure a reasonable core/corona volume ratio.

Fulfilling these criteria, our group recently developed novel ligand-stabilized platinum NPs which self-assembled with poly(isoprene-*block*-dimethylaminoethyl methacrylate) (PI-*b*-PDMAEMA), see Figure 3.1.[35,37] The use of thiol-containing quaternary ammonium salts with ether chain ends as a ligand ensured Pt NPs' high solubility in polar solvents as well as dipole-dipole interactions with PDMAEMA. Ageing of Pt NPs removed a small proportion of the ligands on the surface and greatly enhanced the morphology control in the structure formation process, possibly due to the chemisorption of amine groups that exist on each DMAEMA monomer unit to the metal surface. Inverse hexagonal and lamellar hybrid structures were obtained through this method. The ligand density on the NPs surface was estimated based on average particle size as obtained from bright field transmission electron microscopy (BF-TEM) images and thermogravimetric analysis (TGA) results. In the present paper, a full account of these results is given. First, we revisit the question of the ligand density on the Pt NPs. Then we explore the morphology space of PI-*b*-PDMAEMA/Pt NP hybrids, revealing the accessibility of two new morphologies by varying Pt NP/PI-*b*-PDMAEMA ratios. Finally, we discuss the preparation of shape controlled metal nano-objects by disassembly of Pt NP/block copolymer hybrid materials with varying morphologies.

Experimental Section

Materials and Instrumentation

Materials.

For the block copolymer synthesis, *sec*-butyllithium (1.4 M in cyclohexane, Aldrich) was used as received. Isoprene (99 %, Aldrich), cyclohexane (99 %, J. T.
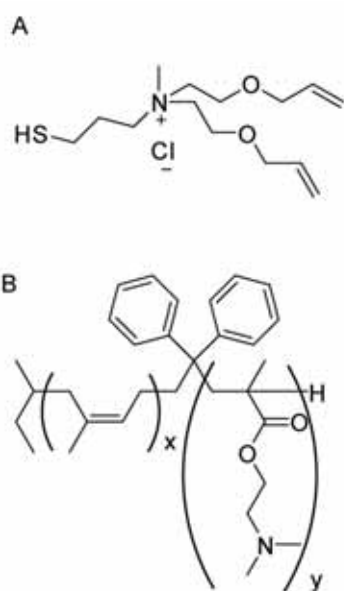
Figure 3.1. (A) *N*, *N*-di-(2-(allyloxy)ethyl)-*N*-3-mercaptopropyl-*N*-3-methylammonium chloride, which is used as ligand to stabilize Pt NPs; (B) poly(isoprene-*block*-dimethylaminoethyl methacrylate) (PI-*b*-PDMAEMA) block copolymer.

Baker), tetrahydrofuran (THF) (99 %, J. T. Baker) and 1, 1-diphenylethylene (97 %, Aldrich) were distilled from *n*-butyllithium (1.6 M in hexanes, Sigma-Aldrich) prior to use. 2-(dimethylamino)ethyl methacrylate (DMAEMA) (98 %, Aldrich) was stirred over CaH_2 (90 %-95 %, Aldrich) overnight and distilled under vacuum. Methanolic HCl (3 N, Supelco) was degassed with a freeze-pump-thaw process three times prior to use.

For the ligand synthesis, 2-allyloxyethanol (Aldrich, 98 %) was stirred over CaH_2 overnight and distilled under vacuum prior to use. 1,3-dibromopropane (Sigma-Aldrich, 99 %) was distilled under vacuum prior to use. Pyridine (Aldrich, anhydrous 99.8 %), phosphorus tribromide (Aldrich, 98 %), 33 wt. % methylamine in ethanol (Aldrich), sodium carbonate (Sigma-Aldrich, 98 %), methanol (J. T. Baker, anhydrous), methanol (Aldrich, anhydrous, 99.8 %), sodium hydrosulfide hydrate (Aldrich), 35 wt % hydrochloric acid aqueous solution (Sigma-Aldrich), potassium hydroxide (Sigma-Aldrich, 97 %), chloroform (J. T. Baker, 99 %) and magnesium sulfate (Sigma-Aldrich, anhydrous, 99 %) were used as received.

For the nanoparticle synthesis and hybrid synthesis, platinum (IV) chloride (Aldrich, 99.9 %), sodium borohydride (Sigma-Aldrich, 99 %), methanol (J. T. Baker, anhydrous), ethyl ether (J. T. Baker, anhydrous) and chloroform (J. T. Baker, 99 %) were used as received.

Instrumentation.

[1]H Nuclear Magnetic Resonance (NMR).

^{1}H solution NMR spectra were recorded on a Varian INOVA 400 MHz spectrometer using CDCl3 signal (δ = 7.27 ppm) as an internal standard.

Small-Angle X-ray Scattering (SAXS).

Small angle x-ray scattering (SAXS) data were obtained on a home-built Rigaku RU3HR CuKα rotating anode beamline. Detailed instrumental setup is described elsewhere.[35]

Bright-Field Transmission Electron Microscopy (BF-TEM).

Hybrid samples were sectioned with a Leica Ultracut UCT cryo-ultramicrotome at -60 °C. Sample slices were collected on a water/dimethyl sulfoxide 60 %/40 % (v/v) solution surface and transferred to copper TEM grids. Pt NP samples were prepared by dissolving the NPs in methanol, ultrasonicating the solution for 1 minute and dropping 5 microliters of the solution to a carbon-supported copper TEM grid with a pipette. BF-TEM images were taken with a FEI Tecnai T12 Spirit electron microscope equipped with a SIS Megaview III CCD camera, operated at an acceleration voltage of 120 kV.

High-Angle Annular Dark Field Scanning Transmission Electron Microscopy (HAADF-STEM)

HAADF-STEM images were taken with a FEI Tecnai F20 field emission electron microscope at an acceleration voltage of 200 kV.

Thermogravimetric Analysis (TGA).

TGA was performed using a TA Instruments Q500 instrument equipped with an auto-sampler. Measurements were taken by heating from 20 °C to 550 °C at 10 °C/min.

Material Synthesis.

PI-*b*-PDMAEMA block copolymers were synthesized using anionic polymerization according to a method described elsewhere.[38] The ligand and Pt NP syntheses as well as NP ageing were performed as described in reference 35.

Pt NP size was characterized by BF-TEM and HAADF-STEM. The composition of ligand-coated Pt NPs was characterized by TGA under flowing

nitrogen. The mass fraction of ligands which was converted into residual carbon after pyrolysis in nitrogen environment was assumed to be consistent (24%) to that obtained previously.[35]

Both the aged NPs and as-made NPs were found to irreversibly aggregate in methanol after extended storage in air (1 month), which could be due to the desorption (oxidation) of the ligands. Thus, all nanoparticles were used within 2 weeks after their synthesis.

Hybrid synthesis.

Mixtures of aged ligand-stabilized Pt NPs and PI-*b*-PDMAEMA were dissolved in 10 wt. % methanol/chloroform 1:9 (w/w) solutions and stirred for at least 1 hr. The solutions were cast on 1 cm diameter aluminum Petri dishes on a hot plate at 50 °C. During casting, a glass hemisphere was used to cover the hot plate and a crystallization dish (diameter 6 cm) full of chloroform was used to slow down chloroform evaporation from the methanol-chloroform mixture. The as-made films were further annealed in a vacuum oven at 110 °C or 130 °C for at least 2 days.

Hybrid disassembly.

Hybrid samples were disassembled by putting small pieces into cyclohexane or THF (~0.1 % w/w) and stirring the solution for 4 hours. For TEM investigation a drop of the resulting solution was put on a TEM copper grid and dried before imaging.

Results and Discussion

1. Nanoparticle ligand density.

The platinum nanoparticles in this work were synthesized via one-phase reduction of metal salts in the excess environment of thiol ligand molecules, followed by the removal of excess ligand and salt.[35] After synthesis the nanoparticles were "aged" by refluxing in water to remove some of the ligands and then were thoroughly washed. In our previous report, based on bright field transmission electron microscopy

(BF-TEM) results, the number of thiol ligand molecules on one Pt NP was calculated to be 92 and 65 before and after the ageing process, respectively, which corresponds to an area occupied by one thiol head group of 0.111 nm^2 and 0.157 nm^2, respectively.[35] In this section, we will revisit the question of the ligand density on the Pt NPs, this time based on particle size distribution data obtained from high-angle annular dark field scanning transmission electron microscopy (HAADF-STEM) image analysis. In the work of Warren *et al.*, we calculated the number of ligands for a Pt NP under the following assumptions[35]:

1. All Pt NPs are assumed to have an average diameter $d = 1.83$ nm.

2. Pt NPs are spherical and have the same density as bulk platinum metal.

3. The average weight fraction of ligands on the Pt NPs can be derived from the TGA mass loss.

4. The ligand molecular weight after particle synthesis is identical to that of the originally synthesized ligand, with the same counterion ratio between bromides and chlorides.

5. All ligand that is present is bound directly to nanoparticle surface, which is supported by NMR analysis.[35]

Here, we want to take a closer look at the first assumption. As the metal particle size decreases, the surface area to volume ratio (S/V) increases, which leads to a higher ligand content per unit mass of Pt for smaller NPs. Rather than using average values for the radius, a more accurate assumption is to linearly correlate the surface area of Pt NPs to the number of ligands. In order to obtain the surface area of Pt NPs, one needs to determine the accurate particle size distribution including sub-1-nm NPs, which is difficult to obtain from BF-TEM due to the lack of contrast.[39] HAADF-STEM imaging is a more effective technique for this problem since it collects

electrons scattered at larger angles (> 5°), and and therefore provides high contrast images for large atomic number species.[40]

Figure 3.2 shows the HAADF-STEM images of the Pt NPs from batches that were used to form nanostructures with block copolymers. The histograms derived from these images revealed:

1. that a large number of sub-1-nm NPs are distinctly visible in HAADF-STEM images, while the bright field TEM images do not provide enough contrast to show such small particles. The formation of metal nanoclusters (i.e., nanoparticles smaller than 1 nm)[41,42] in the presence of thiols have been reported for other metals such as silver, gold and palladium.[43-45]

2. that, compared to as-made NPs (top left in Figure 3.2), aged NPs (top right in Figure 3.2) have a broader size distribution toward larger particles. We note, however, that the sub-1-nm particles are still present in significant quantities even after the ageing process.

In the following we calculate the thiol head group area from this new HAADF-STEM data. From TGA analysis (data not shown), the as-made NPs, on average, contained 55.5 wt. % Pt, and the aged NPs contained 64.2 wt. % Pt. The following equations refer to the as-made NPs.

The total Pt mass for the ensemble of NPs imaged as shown in Figure 3.2 is:

$$M_{Pt} = \rho \cdot \sum \frac{4}{3}\pi r^3 = 1.749 \cdot 10^{-18}\,\text{g} \qquad [1]$$

where r is the radius of each particle core and the summation is over all particles of the measured size distribution. The total surface area, S, for this ensemble is:

$$S = \sum 4\pi r^2 = 4.410 \cdot 10^{-16}\,\text{m}^2 = 441.0\,\text{nm}^2. \qquad [2]$$

Therefore the area that one thiol occupies on the platinum surface is:
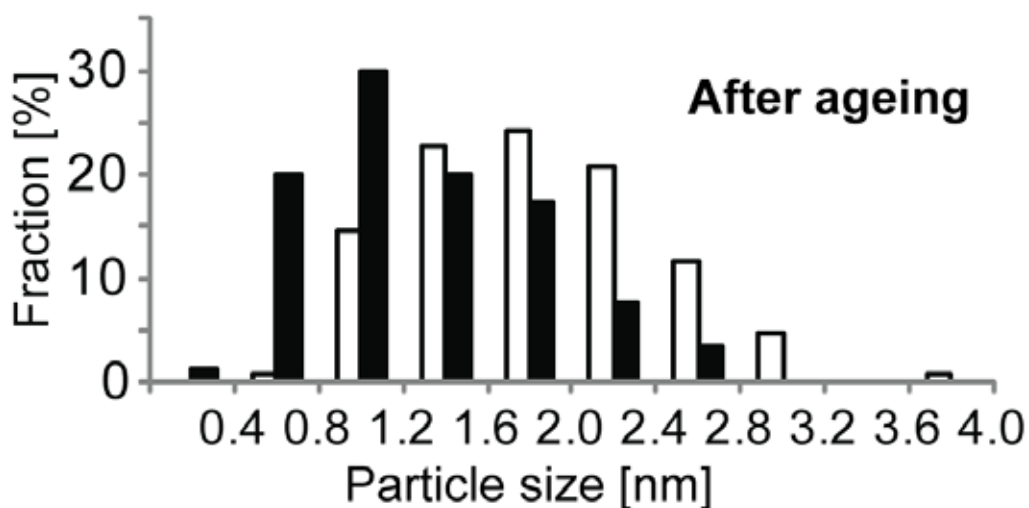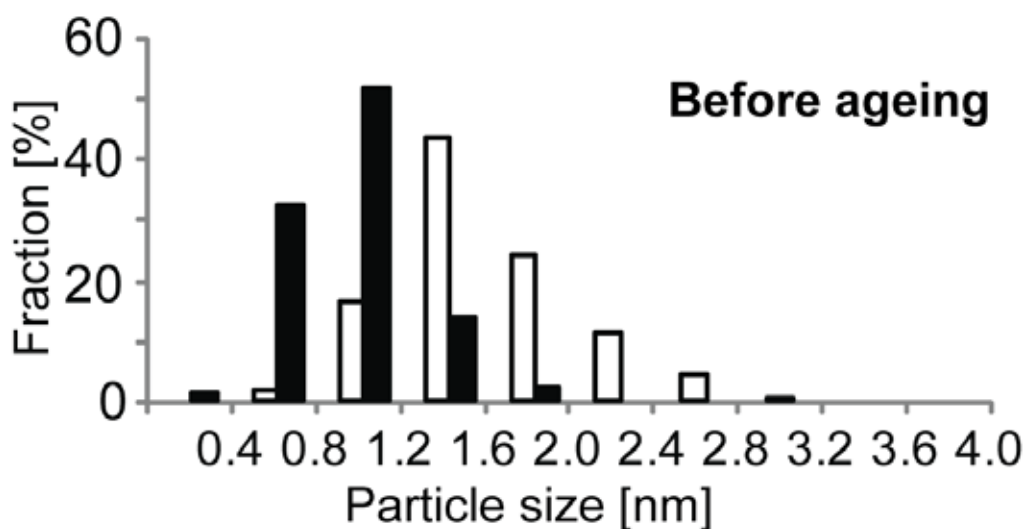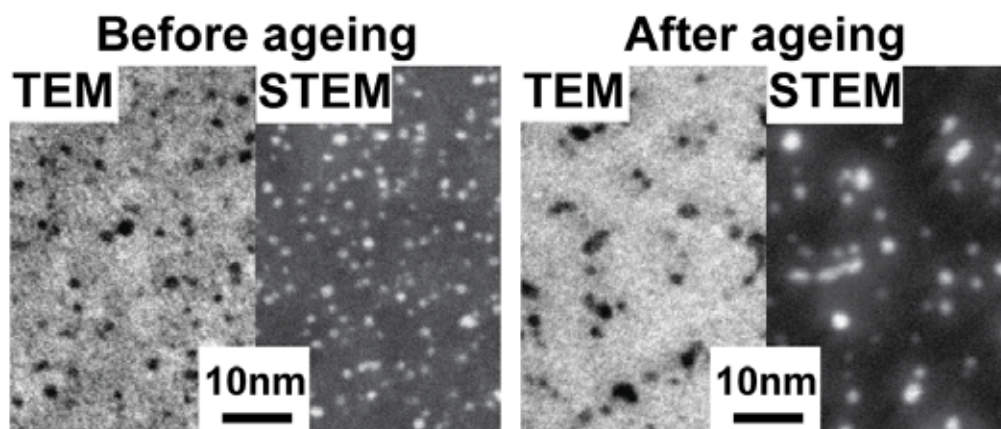
Figure 3.2 (Top) BF-TEM and HAADF-STEM images of Pt NPs before and after ageing process. (Middle/Bottom) Histograms of Pt NP size distributions obtained from BF-TEM and HAADF-STEM images. White bars refer to the distribution from BF-TEM images, and black bars refer to that from HAADF-STEM images.

$$\frac{S}{\#\,of\,ligands} = 441.0\,\text{nm}^2 \bigg/ \left[\frac{\left(\dfrac{1.749\cdot10^{-18}\,\text{g}}{1-0.555}\right)-1.749\cdot10^{-18}\,\text{g}}{331.7\,\text{g/mol}} \cdot \frac{6.022\cdot10^{23}\,\text{ligands}}{\text{mol}} \right] = 0.173\,\text{nm}^2/\text{ligand}\;.\;[3]$$

Here 331.7 g/mol is the molar mass of the ligand in Figure 3.1A.[35] The aged NPs yielded 0.196 nm^2 per thiol following the same calculation. For comparison, the area per thiol head group for a methanethiol-coated Pt{111} surface is 0.200 nm.[46] Many factors affect the area per thiol head group on metal surfaces, including surface curvature, existence of metal nanocrystal defects such as edges, steps and vertices, and tail size of the ligand.[39,47-51] The fact that the NP ligand density is similar to that of a simple alkanethiol on a flat Pt surface suggests that the effects from the high NP surface curvature cancels the steric effect from the large tail volume, allowing a large conical angle for the ligand molecule rotation.

2.   Hybrid morphology exploration.

We investigated PI-*b*-PDMAEMA/Pt NP self-assembly with two different PI-*b*-PDMAEMA block copolymers, referred to as MK31 (31,000 g/mol, 33 wt. % PDMAEMA) and MK29 (29,000 g/mol, 17 wt. % PDMAEMA). The polydispersity index (PDI) of both polymers was below 1.1 (M_w/M_n = 1.03 and 1.06, for MK31 and MK29, respectively, where M_w is weight average molecular weight and M_n is number average molecular weight).

We prepared a series of hybrid samples by varying Pt NPs/PI-*b*-PDMAEMA ratios. All the Pt NPs used to synthesize hybrids were aged, with ligand head group densities of ~0.196 nm^2 per thiol, following the calculation discussed above. Table 3.1 lists the Pt NPs/PI-*b*-PDMAEMA ratios of different hybrids and the corresponding morphologies obtained, as suggested by a combination of small angle x-ray scattering and TEM analysis, see below. The table also includes the results of our previous

Table 3.1. Summary of hybrids' hydrophilic volume fraction and corresponding morphology.

Sample	PI-b-PDMAEMA M_n (Kg·mol^{-1})	PDMAEMA Fraction (wt. %)	Pt NPs/PI-b-PDMAEMA weight ratio	Hydrophilic domain volume ratio*	Morphology	q^* (nm^{-1})
MK29-1	29	17	0.52	0.25	Spherical	0.28
MK29-2	29	17	0.76	0.29	Spherical	0.26
MK29-3	29	17	1.0	0.33	Wormlike Micelle	0.23
MK29-4	29	17	1.54	0.41	Wormlike Micelle	0.18
CCM-Pt-4‡	31	33	2.2	0.55	Lamellae	0.19
MK31-1 †	31	33	(3.5)	(0.65)	Lamellae	0.17
MK31-2	31	33	3.0	0.62	Lamellae + Inverse hexagonal	0.18
MK31-3	31	33	3.2	0.63	Inverse hexagonal	0.21
CCM-Pt-6‡	31	33	3.5	0.65	Inverse hexagonal	0.21

*Hydrophilic domain volume ratio (Pt NPs/PI-b-PDMAEMA volume ratio) were calculated according to ρ(PI) = 0.91 g/mol, ρ(PDMAEMA)=1.15 g/cm^3, ρ(Pt) = 21.09 g/cm^3, ρ(ligand)= 1.3 g/cm^3.

† Sample showed precipitation of particles.

report.[35] As the volume fraction of the inorganic content increases, four different morphologies were obtained as revealed by BF-TEM, see Figure 3.3: spherical micelles (Figure 3.3A), wormlike micelles (Figure 3.3B), lamellae (Figure 3.3C), and inverse hexagonal cylinders (Figure 3.3D). In the BF-TEM images, PI appears as bright domains while PDMAEMA/Pt NPs appear dark, with contrast arising from the electron density difference between the different domains. We note that when more NPs were added to MK29 with the shorter PDMAEMA chains (5,000 g/mol for MK29 versus 10,000 g/mol for MK31), macrophase separation with aggregated NPs was observed. Also, in some of the films that used MK29, occasionally NP agglomeration was observed along with microphase separated structures. All these observations suggest that MK29's PDMAEMA chains may be at the lower limit relative to the NP size necessary to observe good structure control. The radius of gyration calculated for MK31 and MK29 are 2.5 nm and 1.8 nm, respectively.[52] Indeed, the radius of gyration of MK29 is very close to the average Pt NP size, inconsistent with criteria #3 in our list above.

Figure 3.4 shows the small-angle X-ray scattering (SAXS) patterns of annealed hybrids with the four different morphologies. Although the patterns display too few orders to unambiguously determine phases, if one assumes phases indicated by TEM (Figure 3.3), the position of the first order is a consistency check of the structure. Here the scattering vector q is defined as $q = 4\pi\sin\theta/\lambda$, where 2θ is the scattering angle and λ is the wavelength of the CuKα x-ray beam, 1.54Å. q^* signifies the position of the first peak in the scattering pattern. The first Bragg reflection for the lamellar hybrid MK31-1 at 0.17 nm^{-1} corresponds to an interplanar spacing of 36 nm, while that for the inverse hexagonal hybrid MK31-3 at 0.21 nm^{-1} corresponds to an channel-to-channel spacing ((10) period in the hexagonal lattice, $d_{10} = 4/\sqrt{3}q^*$) of 35 nm. Both spacings are consistent with the periods of the nanostructures measured from BF-TEM images.
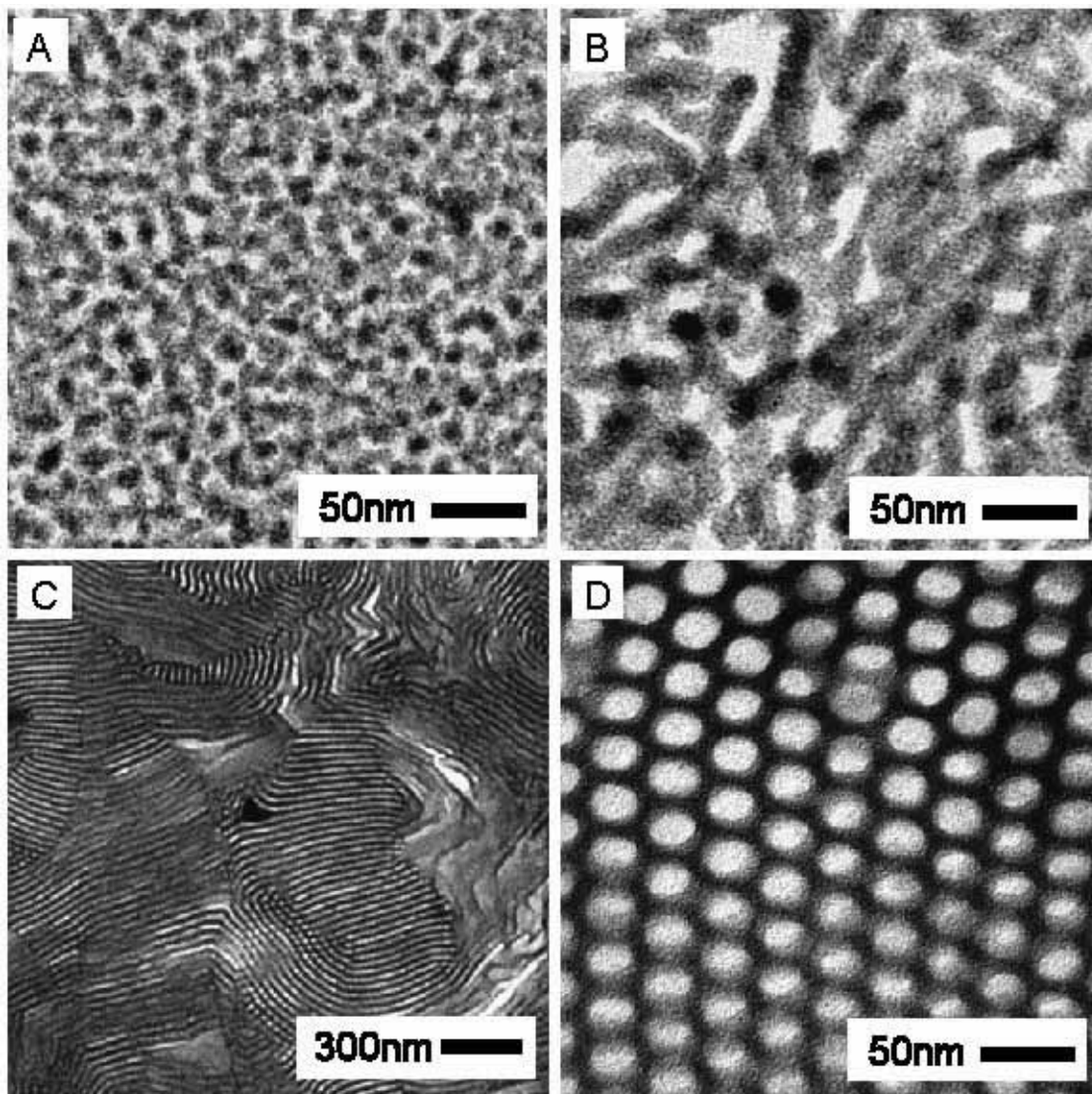
Figure 3.3. Representative bright field TEM images: (A) spherical micellar morphology (MK29-2); (B) wormlike cylinders morphology (MK29-3); (C) lamellar morphology (MK31-1); (D) inverse hexagonal morphology (MK31-3).
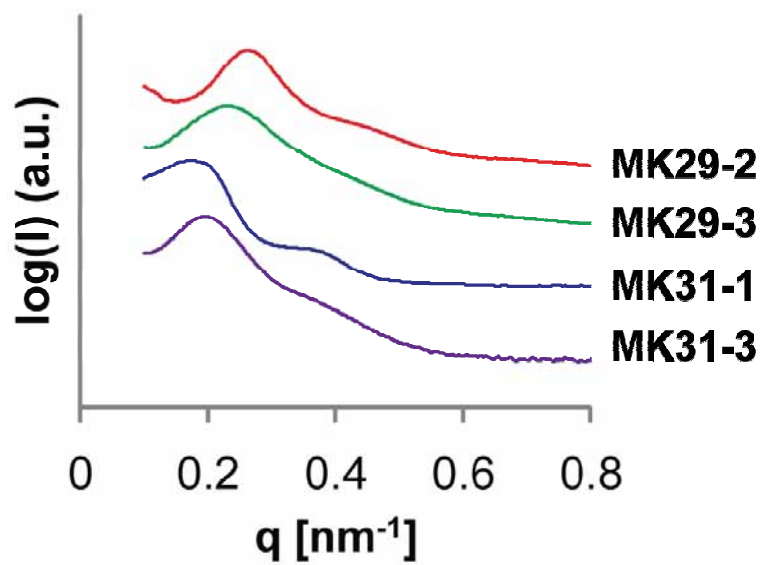
Figure 3.4. Small angle X-ray scattering (SAXS) patterns from annealed BCP/Pt NP hybrids. The curves show the intensity profiles for spherical micellar, wormlike micellar, lamellar, and inverse hexagonal morphologies, from top to bottom.

We note that in most hybrids, due to the small grain size of the nanostructures (generally smaller than a couple of microns, corresponding to 40-50 repeat units at most in thermally annealed films) coupled with the large x-ray attenuation from Pt, higher-order reflections were not clearly distinguished.

From both SAXS and TEM data of samples with lower NP loadings, the morphologies obtained had particularly limited long range orders. It has to be noted that thin sections of samples for TEM (Figure 3.3A and B) were sliced using cryo-ultramicrotoming at the water/DMSO eutectic temperature of -60 °C, which is around the glass transition temperature (T_g) of PI (-60 °C). Thus structure deformation during (or after) microtoming cannot be excluded and is rather very likely for samples with PI majority phase. When Pt NPs/PDMAEMA domains make up the majority part of the hybrids, however, low T_g PI domains are embedded within a higher T_g framework (T_g of PDMAEMA ~ 20 °C). No distortions are thus expected during the sample preparation process, consistent with our observations in TEM (Figure 3.3C and D).

3. Isolated nano-objects disassembled from hybrids

We have shown that hybrids with inverse hexagonal morphology can be subsequently pyrolyzed followed by acid or plasma treatment to remove the block copolymer, generating a nanoporous metal 3D framework.[35] In contrast, similar heat treatments of hybrids without inter-connected inorganic network structures such as lamellar and micellar films will lead to a collapse of the 3D structure. For poly(isoprene-*block*-ethylene oxide) (PI-*b*-PEO)/aluminosilicate hybrid films with a dispersed inorganic phase, Ulrich *et al*. showed that isolated polymer-ceramic hybrid nano-objects with well-defined shape and size can be achieved through dissolution in organic solvents.[53] For the PI-*b*-PDMAEMA/Pt NPs system, we thus explored the formation of shape and size controlled metallic nano-objects from disassembly experiments.[34,54-56] Indeed, by stirring hybrid films with spherical, wormlike micellar
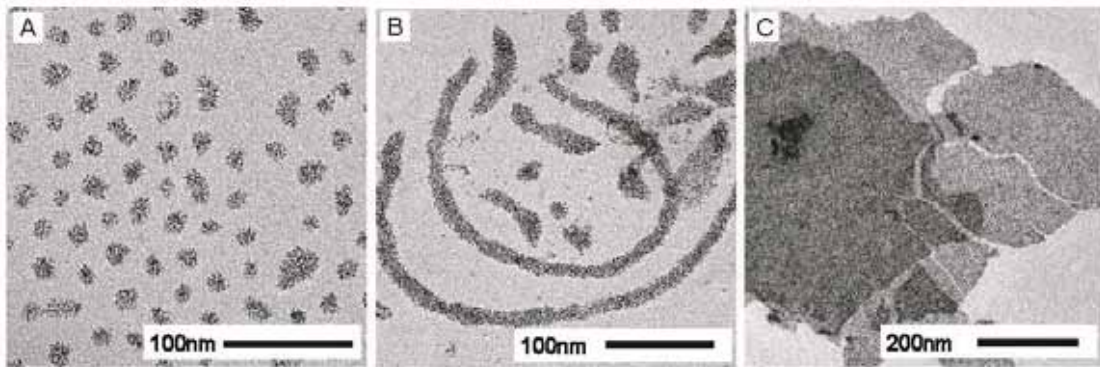
Figure 3.5. Representative bright field TEM images of isolated nano-objects: (A) spheres from sample MK29-2; (B) wormlike cylinders from sample MK29-4; (C) lamellar sheets from sample MK31-1.

and lamellar morphologies in cyclohexane or tetrahydrofuran for 4 hours, isolated spheres, cylinders and nano-sheets were obtained, respectively, as shown in Figure 3.5. Figure 3.5A shows nano-spheres obtained from micellar structures. Dissolution of wormlike micelles leads to isolated cylinders with different aspect ratios, see Figure 3.5B. Nano-sheets were obtained from dissolution of lamellar hybrids, see Figure 3.5C. It should be noted that these results provide independent proof of the structure assignments that were based on SAXS and TEM results in the previous section. In analogy to what was observed for the PI-*b*-PEO/aluminosilicate system, the current nano-objects have a core-shell structure with a PDMAEMA/Pt NP core and PI chains as a shell, increasing the solubility of the nano-object in organic solvents.[53] Since PI chains provide only low contrast, the TEM images only show the core of the nano-objects. High resolution images of these isolated nano-structures further confirm that the cores consist of small Pt NPs (data not shown as is already evident from Figure 3.5).

The average size of the spheres obtained by dissolution of samples MK29-1 and MK29-2 increased from 14 nm to 17 nm, respectively, consistent with increasing Pt NP/BC ratios of the hybrids. Likewise, the average dimensions of the nano-cylinders disassembled from hybrids MK29-3 and MK29-4 increased from 12 nm to 16 nm. The length of the cylinders as well as the size of the nano-sheets obtained from lamellar hybrids was not very well defined, ranging from several hundred nanometers to several microns. As demonstrated before for aluminosilicate cylinders, the length (size) of the nano-objects can be tailored, for example, through ultrasonication, making this a powerful tool for the formation of well-defined nano-objects.[6,57] These nano-objects are stable in solution for at least one week both in cyclohexane and in THF (data not shown), indicating that the NPs and PDMAEMA formed an integrated composite.

Conclusion

We have successfully formed BCP/metal hybrid materials from functional ligand-stabilized Pt NPs and amphiphilic PI-*b*-PDMAEMA diblock copolymers, with increasing metal loadings leading to four distinct nanocomposites. The ligand functionality containing an ionic part and a hydrophilic tail with steric hindrance ensures high NP solubility in polar solvents as well as compatibility with the hydrophilic block of the BCP. The Pt NP size distribution was measured by HAADF-STEM, which enabled a more accurate estimate of the ligand head group density of the Pt NPs. Disassembly of hybrids without a continuous inorganic phase resulted in metallic nano-objects with core-shell architecture and well defined shapes. By future tuning of metal NP/BCP hybrid systems through block copolymer structure/chemistry variations and/or nanoparticle compositions, other morphologies such as bi- or triply-continuous structures particularly interesting for energy related applications[3,58] as well as mixed metals based ordered nanostructures should become accessible which may exhibit novel optical, magnetic or catalytic properties.

REFERENCES

1.	Bates, F. S. *Science* **1991,** *251*, 898.
2.	Bates, F. S.; Fredrickson, G. H. *Annu. Rev. Phys. Chem.* **1990,** *41*, 525.
3.	Cho, B.-K.; Jain, A.; Gruner, S. M.; Wiesner, U. *Science* **2004,** *305*, 1598.
4.	Kamperman, M.; Wiesner, U. *Block Copolymers in Nanoscience*, Lazzari, M.; Liu, G.; Lecommandoux, S., Eds. WILEY-VCH Verlag GmbH & KgaA: Weinheim, 2006; p 309.
5.	Templin, M.; Franck, A.; DuChesne, A.; Leist, H.; Zhang, Y. M.; Ulrich, R.; Schadler, V.; Wiesner, U. *Science* **1997,** *278*, 1795.
6.	B. Hamdoun, D. Ausserré, S. Joly, Y. Gallot, V. Cabuil, C. Clinard. *J. Phys. II France* **1996,** 6, 493.
7.	Simon, P. F. W.; Ulrich, R.; Spiess, H. W.; Wiesner, U. *Chem. Mater.* **2001,** *13*, 3464.
8.	Bagshaw, S. A.; Prouzet, E.; Pinnavaia, T. J. *Science* **1995,** *269*, 1242.
9.	Tanev, P. T.; Pinnavaia, T. J. *Science* **1995,** *267*, 865.
10.	Zhao, D. Y.; Feng, J. L.; Huo, Q. S.; Melosh, N.; Fredrickson, G. H.; Chmelka, B. F.; Stucky, G. D. *Science* **1998,** *279*, 548.
11.	Yang, P. D.; Zhao, D. Y.; Margolese, D. I.; Chmelka, B. F.; Stucky, G. D. *Nature* **1998,** *396*, 152.
12.	Lee, J.; Orilall, M. C.; Warren, S. C.; Kamperman, M.; Disalvo, F. J.; Wiesner, U. *Nat. Mater.* **2008,** *7*, 222.
13.	Kamperman, M.; Garcia, C. B. W.; Du, P.; Ow, H. S.; Wiesner, U., *J. Am. Chem. Soc.* **2004,** *126*, 14708-14709.
14.	Malenfant, P. R. L.; Wan, J.; Taylor, S. T.; Manoharan, M. *Nat. Nanotechnol.* **2007**, 463, 78.
15.	Chan, Y. N. C.; Craig, G. S. W.; Schrock, R. R.; Cohen, R. E. *Chem. Mater.* **1992,** *4*, 885.
16.	Chan, Y. N. C.; Schrock, R. R.; Cohen, R. E. *Chem. Mater.* **1992,** *4*, 24.
17.	Sankaran, V.; Cummins, C. C.; Schrock, R. R.; Cohen, R. E.; Silbey, R. J. *J. Am. Chem. Soc.* **1990,** *112*, 6858-6859.
18.	Spatz, J. P.; Herzog, T.; Mossmer, S.; Ziemann, P.; Moller, M. *Adv. Mater.* **1999,** *11*, 149.
19.	Yamauchi, Y.; Sugiyama, A.; Morimoto, R.; Takai, A.; Kuroda, K. *Angew. Chem., Int. Ed.* **2008,** *47*, 5371.
20.	Bockstaller, M. R.; Lapetnikov, Y.; Margel, S.; Thomas, E. L. *J. Am. Chem. Soc.* **2003,** *125*, 5276.
21.	Kim, B. J.; Chiu, J. J.; Yi, G. R.; Pine, D. J.; Kramer, E. J. *Adv. Mater.* **2005,** *17*, 2618.
22.	Kim, B. J.; Bang, J.; Hawker, C. J.; Kramer, E. J. *Macromolecules* **2006,** *39*, 4108.
23.	Kim, B. J.; Fredrickson, G. H.; Kramer, E. J. *Macromolecules* **2008,** *41*, 436-447.

24.   Chiu, J. J.; Kim, B. J.; Kramer, E. J.; Pine, D. J. *J. Am. Chem. Soc.* **2005,** *127*, 5036.

25.   Lin, Y.; Boker, A.; He, J. B.; Sill, K.; Xiang, H. Q.; Abetz, C.; Li, X. F.; Wang, J.; Emrick, T.; Long, S.; Wang, Q.; Balazs, A.; Russell, T. P. *Nature* **2005,** *434*, 55.

26.   Oren, R.; Liang, Z.; Barnard, J. S.; Warren, S. C.; Wiesner, U.; Huck, W. T. S. *J. Am. Chem. Soc.* **2009,** *131*, 1670.

27.   Jain, A.; Wiesner, U. *Macromolecules* **2004,** *37*, 5665.

28.   Attard, G. S.; Göltner, C. G.; Corker, J. M.; Henke, S.; Templer, R. H. *Angew. Chem., Int. Ed.* **1997,** *36*, 1315.

29.   Yamauchi, Y.; Yokoshima, T.; Mukaibo, H.; Tezuka, M.; Shigeno, T.; Momma, T.; Osaka, T.; Kuroda, K. *Chem. Lett.* **2004,** *33*, 542.

30.   Lo, C. T.; Lee, B.; Pol, V. G.; Rago, N. L. D.; Seifert, S.; Winans, R. E.; Thiyagarajan, P. *Macromolecules* **2007,** *40*, 8302.

31.   Park, J. H.; Sun, Y. J.; Goldman, Y. E.; Composto, R. J. *Macromolecules* **2009,** *42*, 1017.

32.   Huh, J.; Ginzburg, V. V.; Balazs, A. C. *Macromolecules* **2000,** *33*, 8085.

33.   Thompson, R. B.; Ginzburg, V. V.; Matsen, M. W.; Balazs, A. C. *Science* **2001,** *292*, 2469.

34.   Warren, S. C.; DiSalvo, F. J.; Wiesner, U. *Nat. Mater.* **2007,** *7*, 156.

35.   Warren, S. C.; Messina, L. C.; Slaughter, L. S.; Kamperman, M.; Zhou, Q.; Gruner, S. M.; DiSalvo, F. J.; Wiesner, U. *Science* **2008,** *320*, 1748.

36.   Warren, S. C.; Wiesner, U. *Pure Appl. Chem.* **2009,** *81*, 73.

37.   Warren, S. C.; Banholzer, M. J.; Slaughter, L. S.; Giannelis, E. P.; DiSalvo, F. J.; Wiesner, U. *J. Am. Chem. Soc.* **2006,** *128*, 12074.

38.   Creutz, S.; Teyssie, P.; Jerome, R. *Macromolecules* **1997,** *30*, 5596.

39.   Eklund, S. E.; Cliffel, D. E. *Langmuir* **2004,** *20*, 6012.

40.   Otten, M. T., *Journal of Electron Microscopy Technique* **1991,** *17* (2), 221-230.

41.   The terms *nanoparticle*, and *nanocluster* are loosely defined. According to literature[42], the term *nanoparticle* refers either "to all 0 D nanosized building blocks" or "amorphous or semicrystalline 0D nanostructures with dimensions larger than 10 nm." Nanoclusters, on the other hand, refer to smaller-sized nanostructures. In this article we use the term *nanoparticles* for our platinum nanomaterials to maintain consistency with our previous publications.[35,36]

42.   Fahlman, B. D. *Materials Chemistry.* Springer: Dordrecht, The Netherlands, 2007.

43.   Dance, I. G.; Fisher, K. J.; Banda, R. M. H.; Scudder, M. L. *Inorg. Chem.* **1991,** *30*, 183.

44.   Jadzinsky, P. D.; Calero, G.; Ackerson, C. J.; Bushnell, D. A.; Kornberg, R. D. *Science* **2007,** *318*, 430.

45.   Zamborini, F. P.; Gross, S. M.; Murray, R. W. *Langmuir* **2001,** *17*, 481.

46.   Kim, S. S.; Kim, Y.; Kim, H. I.; Lee, S. H.; Lee, T. R.; Perry, S. S.; Rabalais, J. W. *J. Chem. Phys.* **1998,** *109*, 9574.

47.   Love, J. C.; Estroff, L. A.; Kriebel, J. K.; Nuzzo, R. G.; Whitesides, G. M. *Chem. Rev.* **2005,** *105*, 1103.

48.   Hostetler, M. J.; Stokes, J. J.; Murray, R. W. *Langmuir* **1996,** *12*, 3604.

49.   Hostetler, M. J.; Wingate, J. E.; Zhong, C.-J.; Harris, J. E.; Vachet, R. W.; Clark, M. R.; Londono, J. D.; Green, S. J.; Stokes, J. J.; Wignall, G. D.; Glish, G. L.; Porter, M. D.; Evans, N. D.; Murray, R. W., *Langmuir* **1998**, *14*, 17.

50.   Luedtke, W. D.; Landman, U., *J. Phys. Chem. B* **1998**, *102*, 6566.

51.   Hill, H. D.; Millstone, J. E.; Banholzer, M. J.; Mirkin, C. A. *ACS Nano* **2009,** *3*, 418.

52.   Santore, M. M.; Kozlova U.S. Patent Application, 11/592,454, 2006.

53.   Ulrich, R.; DuChesne, A.; Templin, M.; Wiesner, U. *Adv. Mater.* **1999,** *11*, 141.

54.   Li, F.; Wang, Z.; Stein, A. *Angew. Chem., Int. Ed.* **2007**, *46*, 1885.

55.   Li, F.; Delo, S. A.; Stein, A. *Angew. Chem., Int. Ed.* **2007**, *46*, 6666.

56.   Lin, X.; Wang, Y.; Wu, L. *Langmuir*, **2009**, *25*, 6081.

57.   Wang, X.; Guerin, G.; Wang, H.; Wang, Y.; Manners, I.; Winnik, M. A. *Science* **2007**, *317*, 644.

58.   Crossland, E. J. W.; Kamperman, M.; Nedelcu, M.; Ducati, C.; Wiesner, U.; Smilgies, D. F.; Toombes, G. E. S.; Hillmyer, M. A.; Ludwigs, S.; Steiner, U.; Snaith, H. J. *Nano Lett.* **2009,** *9*, 2807.

CHAPTER 4

HIERARCHICAL POROUS POLYMER SCAFFOLDS MADE SIM^{2}PLE:
COMBINING SPINODAL DECOMPOSITION WITH BLOCK COPOLYMER
ASSEMBLY PLUS RINSING[*]

Abstract

Hierarchical porous polymer materials are of increasing importance due to their potential application in catalysis, separation technology or bioengineering. While specific examples for their synthesis exist there is a need for a facile yet versatile conceptual approach to hierarchical porous polymer scaffolds with tunable ordered mesostructure. Here we introduce a method termed Spinodal-decomposition Induced Macro and Meso-phase separation PLus Extraction by rinsing (SIM^{2}PLE). It combines well-established concepts of spinodal decomposition at the macroscale and block copolymer self-assembly to tune morphology at the nanoscale with porosity formation on both length scales via rinsing with protic solvents such as water and alcohols. As a first example here hierarchical porous films are formed from poly(styrene-*block*-ethylene oxide) (PS-*b*-PEO) and a PEO oligomer as a small additive. Varying casting temperatures and solvents enables access to tailored hexagonal and cubic mesostructures. We expect this method based on simple thermodynamic principles to provide a powerful approach for the synthesis of hierarchically porous materials.

[*]Sai, H.; Tan, K.W.; Hur, K.; Gruner, S. M.; Wiesner, U. *In preparation.*

Hierarchically porous materials, ubiquitous in biological systems[1-3] and a target for synthetic materials,[4-8] provide synergies between mechanical properties, transport properties and enhanced surface area. Integrating mesoscale (2-50 nm) porosity with three-dimensional continuous macropores (> 50 nm) is of particular importance as it combines high specific surface area with high flux and pore accessibility desired e.g. in catalytic conversions. Potential applications of such hierarchically structured materials range from catalysis to separation technology to bioengineering. Amongst polymeric materials, block copolymer (BCP) self-assembly is known to offer access to mesoscale ordered structures with tunable size and morphology through control over molecular parameters such as block chemistry, sequence and molar mass.[9, 10] Specific methods have been developed to form mesopores from BCP-based assemblies, including chemical block removal[11-13] and swelling with sacrificial components.[14-16] The strong interest in hierarchical polymer scaffolds has resulted in specific strategies for structure generation at multiple length scales using BCPs, such as confined self-assembly in preformed macroscale templates[17-23] and non-solvent- or polymerization- induced phase separation.[24-27] As pointed out in detail recently, however, when combined together, these approaches often require specific and invasive chemistries, only work in narrow synthesis parameter windows, or rely on multiple tedious steps that limit their general use.[16] There is thus a need for a facile yet versatile conceptual approach to hierarchically porous polymer scaffolds with well-controlled structures.

A well-studied physical phenomenon in polymer science is the spinodal decomposition of polymer blends.[16, 28-32] By driving a multicomponent polymeric mixture to a supersaturated state through control of temperature or through quick solvent evaporation, a continuous interface at the micron-scale emerges upon phase segregation. A facile and versatile, yet unexplored approach for generating

hierarchical porosity would be to induce spinodal decomposition in a block copolymer-additive blend that would separate into an additive-rich phase and a BCP-rich phase, where one block gets selectively swollen by the additive (Figure 4.1). *Simply* rinsing out both the additive-rich phase as well as the additive swelling the BCP block with the same selective solvent would then enable hierarchical pore formation. To render the process more relevant for industrial applications it is highly desirable for this extraction solvent to be water or other protic solvents and for the swollen block to be polyethylene oxide (PEO) so as to endow the final material with anti-fouling properties well-established for PEO.[33, 34] Well-defined structure formation would benefit from (a) the BCP to be strongly segregating to ensure structural integrity of the BCP phase during additive removal, (b) one block to have a high glass transition temperature, T_g, to ensure mechanical stability, and (c) a relatively small additive to maximize BCP swelling and, in particular, its removal by rinsing. Key advantage of such an approach would be its conceptual and practical simplicity.

We will refer to this approach as Spinodal-decomposition Induced Macro and Meso-phase separation PLus Extraction by rinsing (SIM^{2}PLE). In order to demonstrate its validity, as a first example here we chose a widely-used strongly-segregating amphiphilic block copolymer, poly(styrene-*block*-ethylene oxide) (PS-*b*-PEO), and a PEO oligomer (o-PEO) as a water / alcohol-soluble small additive, to form a mechanically stable film through solvent evaporation induced phase-separation. To that end, a 36.6 kg/mol PS-*b*-PEO containing 13.8 wt. % PEO was synthesized via sequential anionic polymerization according to previously reported procedures.[35] The BCP was then mixed at a ratio of roughly 1:1 with the o-PEO additive with molar mass of 400 g/mol, the mixture dissolved in xylene at 10 total weight percent, followed by solvent evaporation at 130 °C on a hot plate covered with a hemispherical dome. During the evaporation period, the clear solution turned cloudy,
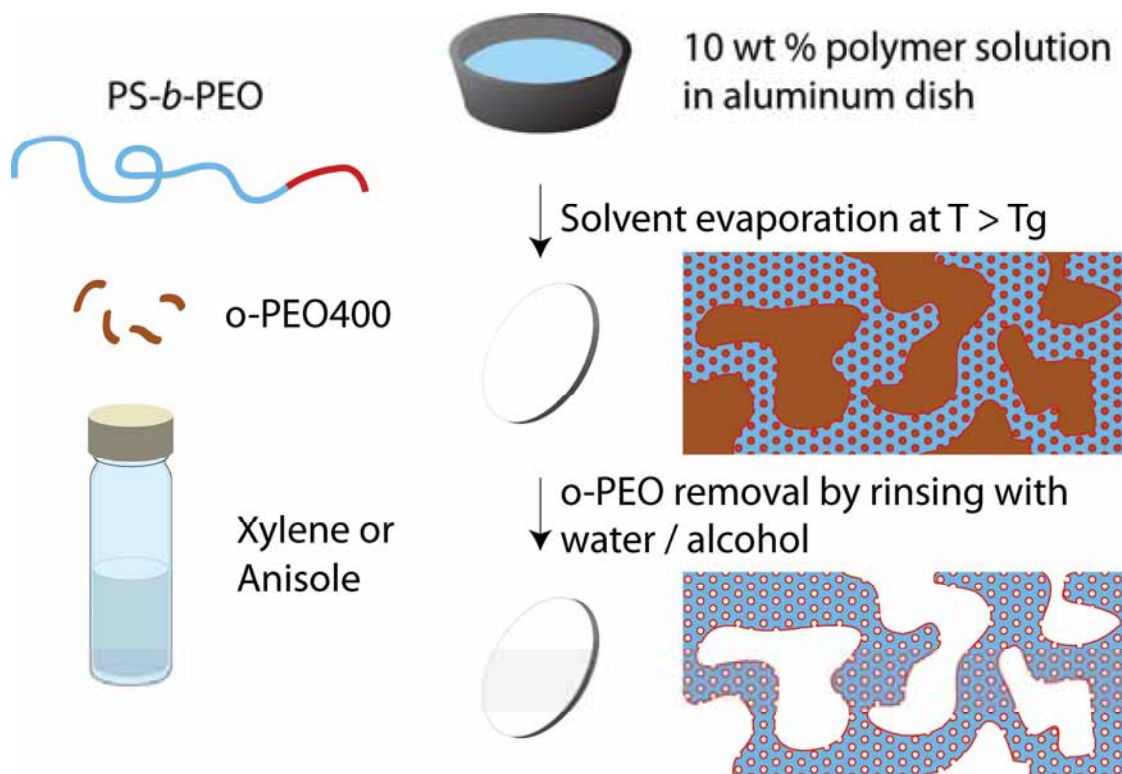
Figure 4.1. Schematic for the synthesis of hierarchically porous polymer scaffolds with ordered mesostructure using the SIM^{2}PLE method. Note that the red color on the surface of the pores suggests PEO lining.

indicating macrophase separation induced scattering of visible light. After xylene evaporation was complete, as indicated by mass loss, the resulting white film was immersed in the protic solvents water, methanol or ethanol to remove o-PEO. Drying the film yielded a lightweight material with a highly opaque appearance.

Figure 4.2 shows scanning-electron microscopy (SEM) images of the film cross-section after removal of o-PEO via rinsing in methanol. Randomly distributed porosity is observed on the micrometer length scale throughout the film (see Figure 4.2a,b). These macropores, albeit broadly distributed in size, form an interconnected network characteristic of co-continuous structures obtained via spinodal decomposition.[25] Within the polymer struts, hexagonally arranged cylindrical mesopores are observed that have a radius of ~13 nm, as estimated from an analysis of the SEM images (see Figure 4.2c,d). These mesopores are preferentially aligned parallel to the macropore walls, and a fraction of pores are observed to be accessible from the macropores (see Figure 4.2c). Rinsing with other protic solvents (water and ethanol) resulted in the same structures (see Supplementary Materials, Figure 4.S1).

Removal of o-PEO from the bulk film is confirmed by comparing gel-permeation chromatography (GPC) results with N,N-dimethylformamide (DMF) as an eluent for the as-cast film and films rinsed with the three protic solvents water, methanol and ethanol (see Figure 4.2e). From the refractive index detector response, 90-95% of the o-PEO is removed by rinsing the as-cast film with these protic solvents for 2 hours at room temperature (compare peaks on the right at ~35 mL). Successful removal of the oligomeric additive corroborates the high degree of interconnected macro- and mesoporosity throughout the structure as observed in SEM.

Further evidence for easy accessibility of, and removal of short-chain o-PEO from, mesopores via rinsing could be established via small angle x-ray scattering (SAXS). Removal of o-PEO should lead to higher electron density contrast and thus
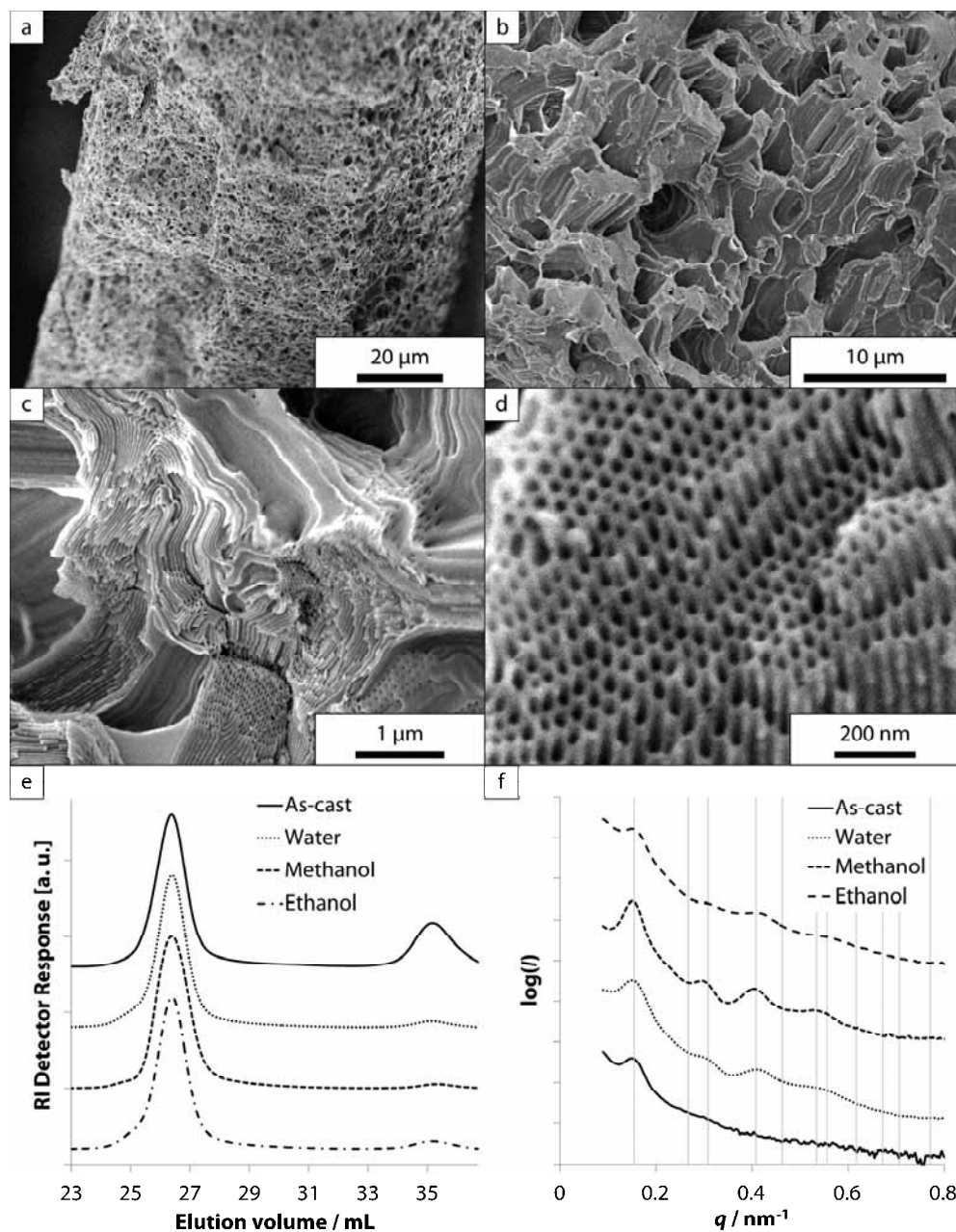
Figure 4.2. (a-d) SEM images at different length scales of a fractured cross-section of a bulk hierarchically porous block copolymer film after removal of o-PEO in methanol. (e) Gel-permeation chromatography traces of as-made and rinsed samples. Each curve is normalized in RI detector response at the peak height of the PS-*b*-PEO peak, and calibrated for elution volume at the PS-*b*-PEO peak. (f) Small-angle X-ray scattering patterns of the as-cast film and films after o-PEO400 removal through rinsing in protic solvents. Curves for methanol-rinsed and ethanol-rinsed samples are shifted vertically by 10^2 and 10^4 upwards, respectively. Tick marks correspond to expected peak positions for a lattice with P6*mm* symmetry with primary peak position of $q^* = 0.154$ nm^{-1}.

appearance of higher order reflections. Figure 4.2f shows the SAXS patterns of an as-made film as well as films after rinsing with water, methanol and ethanol, respectively. The pattern for the as-cast film shows a weak primary peak at $q^* = 0.154$ nm^{-1}, where q denotes the scattering vector magnitude, and is defined as $q = 4\pi\sin\theta/\lambda$, where θ is half of the scattering angle, and λ is the x-ray wavelength. After 2 hours of soaking in protic solvents at room temperature, a set of reflections consistent with a disordered two-dimensional hexagonal lattice (*P6mm* symmetry) appears, with the identical primary peak position, q^*, to the as-cast film. From the primary peak positions, using P6*mm* symmetry, a channel-to-channel distance of 47.1 nm can be calculated, suggesting significant swelling of the PEO block by o-PEO when compared with results on the parent block copolymer film exhibiting a diffuse scattering peak at $q^*=0.25$ nm^{-1} (see Supplementary Materials, Figure 4.S2). The absence of peaks for the rinsed materials at $(q/q^*)^2 = 3$ and 9 may be a consequence of zeros of the cylindrical form factor, $J_1(qR)/qR$, where J_1 is the Bessel function of the first kind with order 1, when R, the cylinder radius, is around 15 nm. The small discrepancy in pore radius, i.e. 13 vs. 15 nm, as determined from SEM and SAXS, respectively, is most likely due to the projection of a three-dimensional structure to a two-dimensional plane and associated inaccuracies in the determination of structural length scales from SEM images. Both GPC and SAXS results suggest that water and methanol are slightly more effective in o-PEO additive removal than ethanol, which may be due to their smaller size.

Nanoscale x-ray computed tomography, NanoCT, was employed in this study to image the three-dimensional (3D) macroporous structure on micron length scales. This technique requires no alteration to the samples prior to imaging, and can reconstruct a relatively large volume of ~1 mm^3. Figure 4.3a shows a three-dimensional rendering of x-ray absorption contrast in the sample, revealing the co-
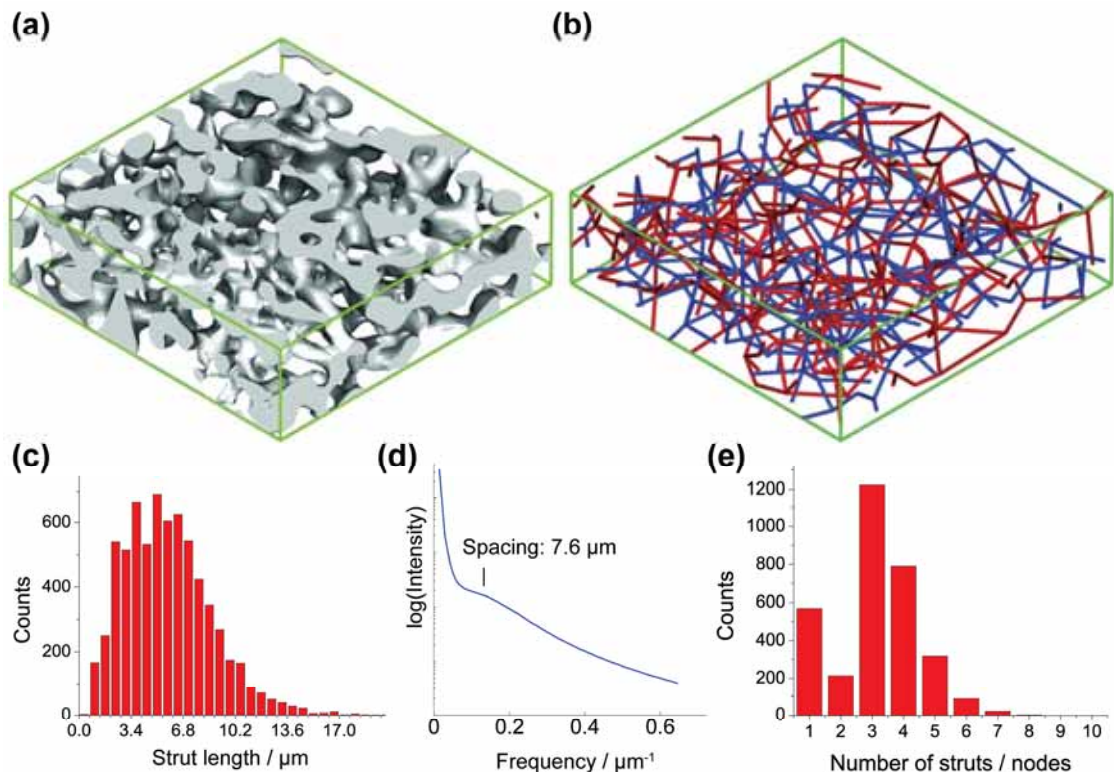
Figure 4.3. Three-dimensional tomographic reconstruction of the macrostructure of a film of a PS-*b*-PEO/o-PEO400 blend cast at 130 °C from xylene, using nanoscale x-ray computed tomography (NanoCT). The sample was rinsed before imaging to remove the o-PEO400. (a) A 68 μm × 68 μm × 20 μm slice of the image visualized through isosurface visualization. Voxel size is 0.68 μm on each side. (b) Skeletal networks of the polymeric (blue) and the porous (red) regions for the same volume as (a). Both networks are fully connected, leaving no isolated clusters. (c) Strut length distribution of the polymer network from a 136 μm × 136 μm × 136 μm slice. A broad distribution with a mean value of 6-7 μm is observed. (d) Radial distribution function plot of the 3D FFT volumetric data from the same slice as (c). A weak correlation peak at 0.13 μm^{-1}, corresponding to a feature size of 7.6 μm, is observed after second derivative analysis. (e) Population distribution of struts per node on the same network as (c). Mono- and di-valent nodes arise from analysis artifacts on the edges of the volume.

continuous nature of the structure. Strut-thinning processes[36] on the interface toward either the polymer region or toward the pore region yielded fully connected skeletal networks throughout the film thickness, confirming a micron-scale bicontinuous network consistent with the suggested spinodal decomposition mechanism (Figure 4.3b). A characteristic feature size of 6-7 μm is detected from both the node-to-node distance distribution of the skeletal network as well as from a weak correlation peak at 7.6 μm in the radial distribution function of the 3D Fast Fourier Transform (FFT) (Figure 4.3c,d). Furthermore, the skeletal network analysis provides information on the degree of complexity as shown in the population distribution of struts per node shown in Figure 4.3e: while a large fraction of nodes are found to be trivalent, we also observed nodes that are as crowded as octavalent.

One of the advantages of working with BCPs is the versatility in precisely controlling nanostructures. Here we found that mesopore morphologies can be tuned by simply controlling the casting temperature. Figure 4.4a-d shows the macro- and meso-structural characteristics as the casting temperature is reduced from 130 to 100 °C while using identical conditions otherwise. The low magnification SEM image in Figure 4.4a displaying the entire film thickness reveals the pore structure differences on the μm length scale when compared with the image in Figure 4.2a. Macropores with sizes as large as 5-10 μm are observed for films cast at 100 °C. On the mesoscale, four-fold symmetry projections for the pore arrangement in cross-sections of the polymer scaffold are observed when the films are cast at 100 °C (Figure 4.4b,c), suggesting a cubic symmetry for the mesostructure formed. It should be noted that in contrast to the hexagonal mesopores, the cubic mesopore structures are isotropic and thus allow for even easier access from the macropores.

In order to corroborate the mesoscale structural difference observed in SEM, SAXS patterns were obtained for the films cast at 100 °C (Figure 4.4d). Similar to the
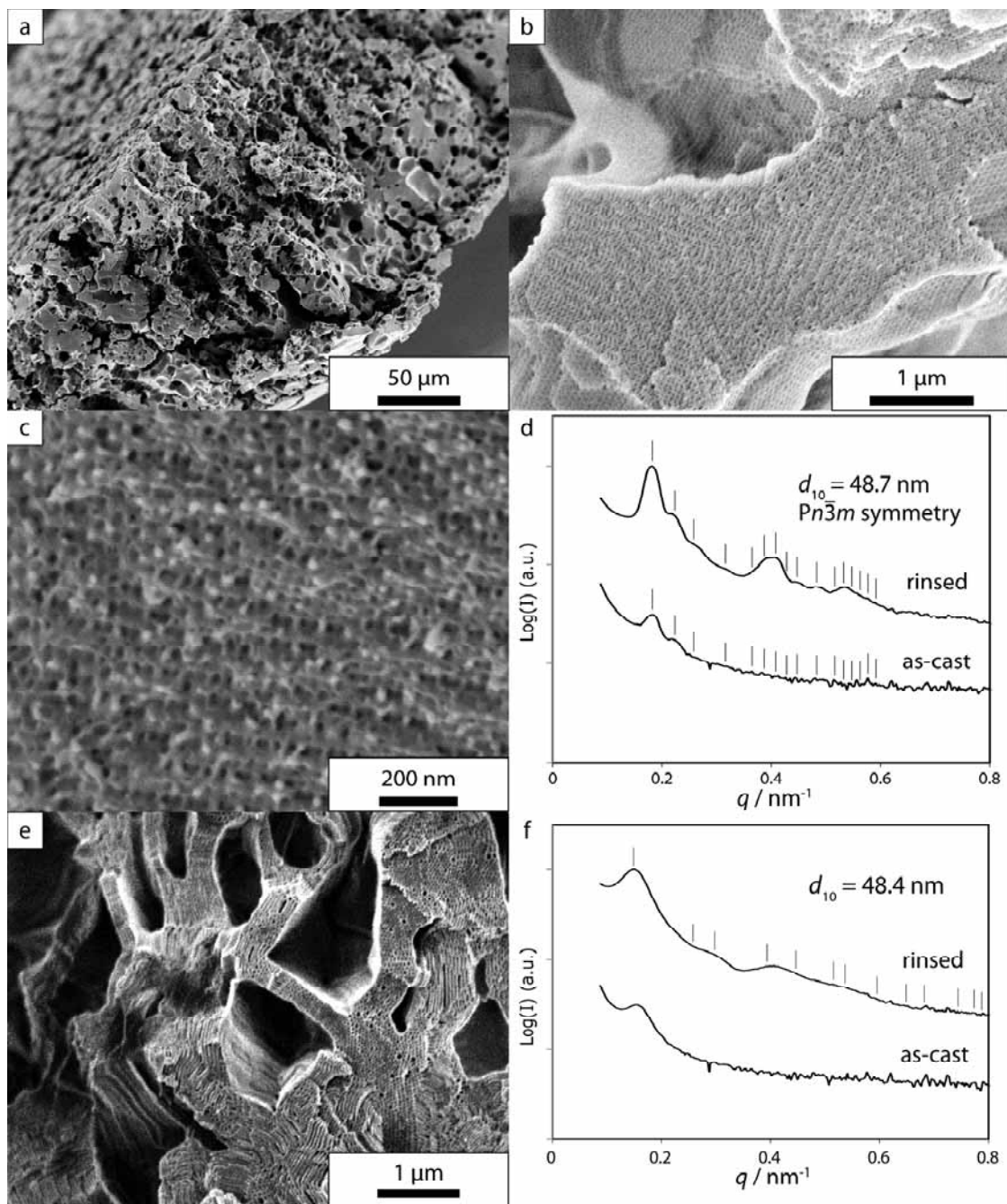
Figure 4.4. (a-c): SEM images of film cross-sections of PS-*b*-PEO/o-PEO400 blends cast from xylene at 100 °C at increasing magnifications. Films were rinsed prior to exposing a fresh cross-section for imaging. Images show macroporosity (a), interconnected mesopores accessible from the macropores (b) and four-fold symmetry in the mesoscale porosity (c). (d) SAXS patterns of as-made and rinsed films cast at 100 °C. Spectrum for the rinsed film is shifted in intensity compared to results from as-made films. (e) SEM image of a film cross-section of a PS-*b*-PEO/o-PEO400 blend cast from anisole at 130 °C. (f) SAXS patterns of as-made and rinsed films cast at 130 °C from anisole.

films prepared at 130 °C, SAXS patterns of as-cast samples showed weak peaks whereas after rinsing with protic solvents patterns exhibited strong higher-order scattering peaks while retaining the primary peak position of the as-cast film. For example, after rinsing with methanol, films show a set of reflections with the ratios of $(q/q^*)^2$ = 2, 3, 4, 6, 9, 10, 12, 14 and 17 with the first order peak location at $q^* = 0.183$ nm^{-1}, which is consistent with a cubic symmetry of aspect 4 with lattice spacing of 48.7 nm.[37] We note that the possibility of indexing the first peak with $(q/q^*)^2 = 4$ is excluded because of the existence of the peak at $q \sim 0.483$ nm^{-1}, or $(q/q^*)^2 = 14$, becoming $(q/q^*)^2 = 28$, since there is no set of lattice indices that satisfies this reflection condition. In the lyotropic liquid crystal community the cubic symmetry of aspect 4 has been associated with double diamond structures. Although the packing frustration in four-fold nodes in neat diblock copolymer systems generally precludes such double-diamond network structure formation, BCP/homopolymer blends are predicted by self-consistent field theory to form double diamond structures through homopolymer segregation in the nodes.[10, 38-40]

As steps towards generalizing these results, we have varied the solvent system from xylene to anisole, a more polar and hydrogen-bonding solvent that dissolves PEO better and has a higher boiling point. Figure 4.4e,f shows the SEM image and SAXS patterns of a film cast at 130 °C from anisole. SEM again shows hexagonal mesopores, while the position of the first peak in the SAXS assigns a mesopore center-to-center spacing of 48.4 nm. While the slow evaporation of anisole compared to xylene resulted in more anisotropic and smaller macropores (Figure 4.4e), the observed hexagonally ordered mesopores indicate that the mesoporous structures for this pair of solvents are not as sensitive to the solvent choice as they are to the change in casting temperature. Furthermore, we have also varied the block copolymer system from PS-*b*-PEO to poly(4-*tert*-butyl)styrene-*block*-ethylene oxide (PtBS-*b*-PEO).

Preliminary results of the SIM²PLE method with oligomeric poly(acrylic acid) (o-PAA) as the additive and tetrahydrofuran (THF) as solvent gave similar hierarchical structures and accessible pores after rinsing with ammonium hydroxide-containing aqueous solution (see Supplementary Materials, Figure 4.S3). Poly(4-*tert*-butyl)styrene has a higher glass transition temperature (T_g = 138 °C) than PS, (T_g = 100 °C), which allows for standard sterilization procedures e.g. autoclaving, to be used on these materials for potential biological applications.

In line with our initial design, the presence of o-PEO played a dual role in the formation of film porosity: we speculate that the o-PEO, a precipitating solvent for the majority PS block of the BCP, induces spinodal decomposition of the initially single-phase solution as the solvent evaporates, consistent with the observed opacity in the films. The macrophase separated o-PEO provides continuous macroporous domains. On the other hand, such spinodal decomposition leaves residual o-PEO in the BCP-rich phase, swelling the PEO block of the block copolymer, leading to ordered mesostructure formation, and rinsed out to yield mesoporosity. The BCP-rich phase develops an ordered mesostructure within the macroscopically phase-separated film.[41, 42] Casting at an elevated temperature compared to the glass transition temperature of polystyrene (130ºC vs. T_g(PS)~100ºC) facilitates fast equilibration on the mesoscale in the melt state, resulting in a high degree of order. Since o-PEO is not a strongly associating swelling agent, rinsing at room temperature for a short period of time is sufficient to form the final hierarchically porous structure. This is in contrast to the often harsh bond cleaving conditions required for etching block copolymer domains.[11-13] Use of the highly amphiphilic BCP, PS-*b*-PEO, prevents significant intrusion of rinsing solvents into the hydrophobic part of the scaffold, contributing to mesostructural integrity. We also note that since the PEO block in the BCP is not

decomposed, the pores are lined with PEO chains providing wettability and possibly anti-fouling properties of the walls.

In conclusion, we have developed a facile and versatile one-pot approach for the preparation of hierarchical macro- and meso-porous scaffolds via spinodal decomposition of a BCP/small additive mixture from solution. The SIM^{2}PLE method combines ease of preparation with high degree and choice of ordering within the macroporous structure and replaces more demanding decomposition or chemical transformation steps to induce macro- and meso-porosity by a simple rinsing step with protic solvents like water or alcohols. It thus provides advantages over multiple-step fabrication methods currently employed for integrating nanoscale porosity into macroscopic scaffolds. We have already shown it to work for multiple block copolymers, small molar mass additives, solvents, and protic rinsing agents. Since the method is based on simple thermodynamic principles it may provide a powerful conceptual approach to generate hierarchical materials.

REFERENCES

1. Weiner, S.; Wagner, H. D., *Annu Rev Mater Sci* **1998,** *28*, 271.
2. Autumn, K.; Liang, Y. A.; Hsieh, S. T.; Zesch, W.; Chan, W. P.; Kenny, T. W.; Fearing, R.; Full, R. J., *Nature* **2000,** *405* (6787), 681.
3. Aizenberg, J.; Weaver, J. C.; Thanawala, M. S.; Sundar, V. C.; Morse, D. E.; Fratzl, P., *Science* **2005,** *309* (5732), 275.
4. Lakes, R., *Nature* **1993,** *361* (6412), 511.
5. Yang, P. D.; Deng, T.; Zhao, D. Y.; Feng, P. Y.; Pine, D.; Chmelka, B. F.; Whitesides, G. M.; Stucky, G. D., *Science* **1998,** *282* (5397), 2244.
6. Sanchez, C.; Arribart, H.; Guille, M. M. G., *Nat. Mater.* **2005,** *4* (4), 277.
7. Kamperman, M.; Burns, A.; Weissgraeber, R.; van Vegten, N.; Warren, S. C.; Gruner, S. M.; Baiker, A.; Wiesner, U., *Nano Lett.* **2009,** *9* (7), 2756.
8. Innocenzi, P.; Malfatti, L.; Soler-Illia, G. J. A. A., *Chem. Mater.* **2011,** *23* (10), 2501.
9. Bates, F. S.; Fredrickson, G. H., *Annu. Rev. Phys. Chem.* **1990,** *41* (1), 525.
10. Matsen, M. W.; Bates, F. S., *Macromolecules* **1996,** *29* (23), 7641.
11. Lee, J. S.; Hirao, A.; Nakahama, S., *Macromolecules* **1988,** *21* (1), 274.
12. Urbas, A. M.; Maldovan, M.; DeRege, P.; Thomas, E. L., *Adv. Mater.* **2002,** *14* (24), 1850.
13. Zalusky, A. S.; Olayo-Valles, R.; Wolf, J. H.; Hillmyer, M. A., *J. Am. Chem. Soc.* **2002,** *124* (43), 12761.
14. Maki-Ontto, R.; de Moel, K.; de Odorico, W.; Ruokolainen, J.; Stamm, M.; ten Brinke, G.; Ikkala, O., *Adv. Mater.* **2001,** *13* (2), 117.
15. Wang, Y.; Tong, L.; Steinhart, M., *ACS Nano* **2011,** *5* (3), 1928.
16. Li, L.; Shen, X.; Hong, S. W.; Hayward, R. C.; Russell, T. P., *Angew. Chem., Int. Ed.* **2012,** *51* (17), 4089.
17. Rider, D. A.; Chen, J. I. L.; Eloi, J.-C.; Arsenault, A. C.; Russell, T. P.; Ozin, G. A.; Manners, I., *Macromolecules* **2008,** *41* (6), 2250.
18. Chen, D.; Park, S.; Chen, J.-T.; Redston, E.; Russell, T. P., *ACS Nano* **2009,** *3* (9), 2827.
19. Dobriyal, P.; Xiang, H.; Kazuyuki, M.; Chen, J.-T.; Jinnai, H.; Russell, T. P., *Macromolecules* **2009,** *42* (22), 9082.
20. Escale, P.; Save, M.; Lapp, A.; Rubatat, L.; Billon, L., *Soft Matter* **2010,** *6* (14), 3202.
21. Jones, B. H.; Lodge, T. P., *Chem. Mater.* **2010,** *22* (4), 1279.
22. Jones, B. H.; Lodge, T. P., *ACS Nano* **2011,** *5* (11), 8914.
23. Knoll, W.; Caminade, A. M.; Char, K.; Duran, H.; Feng, C. L.; Gitsas, A.; Kim, D. H.; Lau, A.; Lazzara, T. D.; Majoral, J. P.; Steinhart, M.; Yameen, B.; Zhong, X. H., *Small* **2011,** *7* (10), 1384.
24. Peinemann, K.-V.; Abetz, V.; Simon, P. F. W., *Nat. Mater.* **2007,** *6* (12), 992.
25. Nakanishi, K.; Amatani, T.; Yano, S.; Kodaira, T., *Chem. Mater.* **2008,** *20* (3), 1108.

26.   Phillip, W. A.; Dorin, R. M.; Werner, J.; Hoek, E. M. V.; Wiesner, U.; Elimelech, M., *Nano Lett.* **2011,** *11* (7), 2892.

27.   Seo, M.; Amendt, M. A.; Hillmyer, M. A., *Macromolecules* **2011,** *44* (23), 9310.

28.   Cahn, J. W., *J. Chem. Phys.* **1965,** *42* (1), 93.

29.   Bates, F. S., *Science* **1991,** *251* (4996), 898.

30.   Izumitani, T.; Hashimoto, T., *Macromolecules* **1994,** *27* (7), 1744.

31.   Lee, J. H.; Balsara, N. P.; Chakraborty, A. K.; Krishnamoorti, R.; Hammouda, B., *Macromolecules* **2002,** *35* (20), 7748.

32.   Morita, H.; Kawakatsu, T.; Doi, M.; Yamaguchi, D.; Takenaka, M.; Hashimoto, T., *Macromolecules* **2002,** *35* (19), 7473.

33.   Prime, K. L.; Whitesides, G. M., *Science* **1991,** *252* (5009), 1164.

34.   Gombotz, W. R.; Guanghui, W.; Horbett, T. A.; Hoffman, A. S., *J. Biomed. Mater. Res.* **1991,** *25* (12), 1547.

35.   Floudas, G.; Ulrich, R.; Wiesner, U., *J. Chem. Phys.* **1999,** *110* (1), 652.

36.   Lee, T. C.; Kashyap, R. L.; Chu, C. N., *CVGIP: Graphical Models and Image Processing* **1994,** *56* (6), 462.

37.   Kasper, J. S.; Lonsdale, K., *International tables for X-ray crystallography.* Kynock Press: Birmingham, Eng., 1952; Vol. 2.

38.   Matsen, M. W., *Phys. Rev. Lett.* **1995,** *74* (21), 4225.

39.   Martinez-Veracoechea, F. J.; Escobedo, F. A., *Macromolecules* **2009,** *42* (22), 9058.

40.   Martinez-Veracoechea, F. J.; Escobedo, F. A., *Macromolecules* **2009,** *42* (5), 1775.

41.   Koizumi, S.; Hasegawa, H.; Hashimoto, T., *Macromolecules* **1994,** *27* (22), 6532.

42.   Ohta, T.; Ito, A., *Phys. Rev. E* **1995,** *52* (5), 5250.

APPENDIX: SUPPLEMENTARY INFORMATION

Materials and Methods

Materials. For the sequential anionic polymerization of PS-*b*-PEO, *n*-butyllithium (1.6 M in hexanes, Acros Organics), *sec*-butyllithium (1.4 M in hexanes, Aldrich), calcium hydride (reagent grade, Sigma-Aldrich), chloroform (ACS grade, J. T. Baker) methanol (anhydrous, J. T. Baker), ethanol (absolute, Pharmco-AAPER), naphthalene (ACS grade, Fisher Scientific), potassium (chunks, 98%, Aldrich) and potassium chloride (extra dry, Alfa Aesar) were used as received. 1,1-diphenylethylene (TCI America) was vacuum distilled and stored under inert atmosphere at -40 °C. Cyclohexane (99.5 %, Sigma-Aldrich) was dried with *n*-butyllithium, with 1,1-diphenylethylene as an indicator, and was vacuum distilled into the reaction flask prior to use. Tetrahydrofuran (J. T. Baker) was distilled over potassium, dried with *n*-butyllithium with 1,1-diphenylethylene as an indicator, and was vacuum-distilled immediately prior to usage. Styrene (99 %, Sigma-Aldrich) and (4-*tert*-butyl)styrene (93 %, Sigma-Aldrich) were stirred under inert atmosphere overnight with calcium hydride and underwent freeze-pump-thaw cycling three times before being vacuum distilled into a frozen ampoule immediately prior to usage. Potassium naphthalenide solution in THF was prepared according to previous work.[1] Ethylene oxide (99.5 %, Aldrich) was double-distilled over *n*-butyllithium at -20 °C into a frozen ampoule immediately prior to usage. Methanolic hydrochloric acid (HCl) solution (3N, Supelco) was degassed by three freeze-pump-thaw cycles immediately prior to usage. For the structure formation, xylene (mixture of isomers, ACS grade, Sigma-Aldrich), anisole (anhydrous, Sigma-Aldrich), THF (anhydrous, Sigma-Aldrich), polyethylene glycol (average M_n ~ 400 g/mol, Sigma-Aldrich) and poly(acrylic acid) (average M_w ~1,800 g/mol, Sigma-Aldrich) were used as received.

Synthesis.

Synthesis of PS-b-PEO and PtBS-b-PEO. A standard Schlenk line with argon as inert gas and a glovebox with nitrogen environment were used in the anionic polymerization of PS-*b*-PEO as described by previous literature.[1] In a 1 L two-neck reaction flask equipped with Rotaflo valves, approximately 350 mL of cyclohexane was vacuum distilled. To this flask, ~40 mL of freshly prepared styrene was added, then 0.73 mL of *sec*-butyllithium solution was added, and the polymerization was carried out at 40 °C overnight. An aliquot of this polymer was withdrawn and quenched with methanol for homopolymer molar mass analysis by GPC. The polymer was then end-capped with excess ethylene oxide, stirred for 12 hours and terminated with excess methanolic HCl. Lithium chloride was removed by multiple extractions of the polymer solution in chloroform with water. The polymer was precipitated in methanol, dried at 130 °C in the reactor for 4 days on a vacuum line, and potassium chloride (5-fold excess against initiator) was added in the glovebox. THF was vacuum distilled into the reactor, and the polymer solution was titrated with potassium naphthalenide solution in THF until a faint green color persisted. Ethylene oxide was added to the reactor, and the polymerization proceeded at room temperature for 4 days. Finally the polymer was terminated with excess methanolic HCl, dried and redissolved in chloroform, extracted multiple times with water and precipitated in cold methanol before drying under vacuum for 2 days.

PtBS-*b*-PEO was synthesized via sequential anionic polymerization following the above steps, except that the PtBS block was polymerized for one hour in THF at -78 °C followed by ethylene oxide end-capping.

Synthesis of the macro/meso-porous scaffolds. 55 mg of PS-*b*-PEO and 45 mg of o-PEO were dissolved in 0.9 g of xylene to form a 10 wt % polymer+o-PEO solution. Xylene dissolves the polymer mixture above ~35 °C. The polymer solution was stirred

before being added to a pre-weighed aluminum dish with a bottom area of ~5 cm^2. The dish was placed on a leveled hotplate, and a hemispherical glass cover was placed on top of the hotplate to prevent rapid solvent evaporation. The solution was then heated at 130 °C. Complete evaporation of xylene was confirmed by mass loss after approximately 1 hour. Prolonged heating resulted in a slow loss of o-PEO via evaporation. After completion of film formation the film was immersed in 20 mL of protic solvents (distilled water, methanol or ethanol) and gently shaken for 2 hours at room temperature to remove o-PEO. Film cracking was observed, reducing the final material dimension to a few millimeters in lateral dimensions. Similar procedure was followed for films cast from anisole with the exception of evaporation time, which was 2 hours.

For PtBS-*b*-PEO scaffolds, 60 mg of PtBS-*b*-PEO and 40 mg of oligomeric poly(acrylic acid) were dissolved in THF at 10 wt% and was cast on a Teflon dish at 50 °C. After solvent evaporation, the transparent film was immersed in ammonium hydroxide solution (1 M) for one hour, followed by rinsing with methanol prior to drying.

Characterization.

Table 4.S1 summarizes the polymer characterization data. PS homopolymer, the corresponding PS-*b*-PEO BCP, and the purchased PEO oligomer were characterized by gel-permeation chromatography (GPC) equipped with a Waters 515 pump, PSS GRAM 100-1000-3000 columns and an Agilent 1200 refractive index detector, using *N*,*N*-dimethylformamide as the eluent. Elugrams were analyzed against a polystyrene standard curve. Total molar mass of the BCP and fraction of o-PEO additive were determined via proton nuclear magnetic resonance (NMR) using a Varian Mercury-300 spectrometer. For PtBS-*b*-PEO, the molar mass of PtBS block was characterized by a separate GPC using THF as the eluent. Small-angle x-ray scattering (SAXS)

patterns of as-cast and rinsed films, as well as the parent BCP film, were obtained at the Cornell High Energy Synchrotron Source (CHESS) G1 station with a beam energy of 9 keV as well as at a home-built Rigaku RU300 CuKα rotating anode beamline. The details of both SAXS beamline configurations are described elsewhere.[2] Acquired 2D patterns were radially integrated around the beam center to produce intensity versus scattering vector magnitude, q, using the MOA suite by Dr. Gilman Toombes.[2] Rinsed films were dried, fractured to expose inner cross-sectional areas, mounted on a stub with carbon tape and coated with gold/palladium before structure characterization by scanning-electron microscopy (SEM) on a Zeiss LEO-1550 instrument at an acceleration voltage of 2.0 kV with an in-lens detector. Nanoscale x-ray computer tomography (nano-CT) image of a hierarchically porous sample was obtained on a Xradia VERSA XRM-500 instrument with 680 nm voxel resolution. 3D isosurface visualization on a 68 μm × 68 μm × 20 μm slice, and 3D FFT analysis on a 136 μm × 136 μm × 136 μm slice were performed using MATLAB. Network connectivity on the material and void sides of the sample was performed on the FFT sample set using ImageJ64.[3]

SUPPLEMENTARY FIGURES AND TABLES

Table 4.S1. Polymer molar mass characterization. Data in parenthesis signifies that polystyrene standard curves were used for molar mass determination of polymers other than polystyrene.

	M_n GPC/ g/mol	M_n NMR / g/mol	PDI	wt % PEO
PS	31540	N/A	1.03	N/A
PS-*b*-PEO	(40790)	36570	1.03	13.75
o-PEO400	(897.2)	N/A	1.03	N/A
PtBS	46750	N/A	1.05	N/A
PtBS-*b*-PEO	(79990)	55040	1.04	15.05
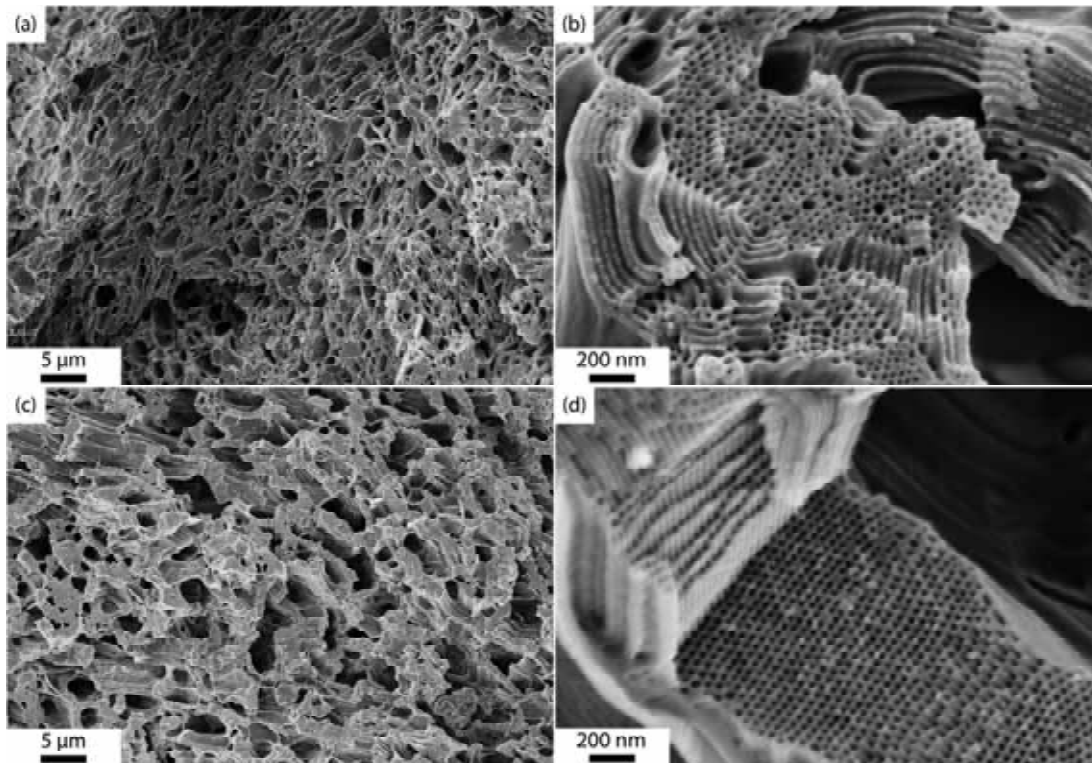
Figure 4.S1. SEM images of samples rinsed in water (a,b) and ethanol (c,d).
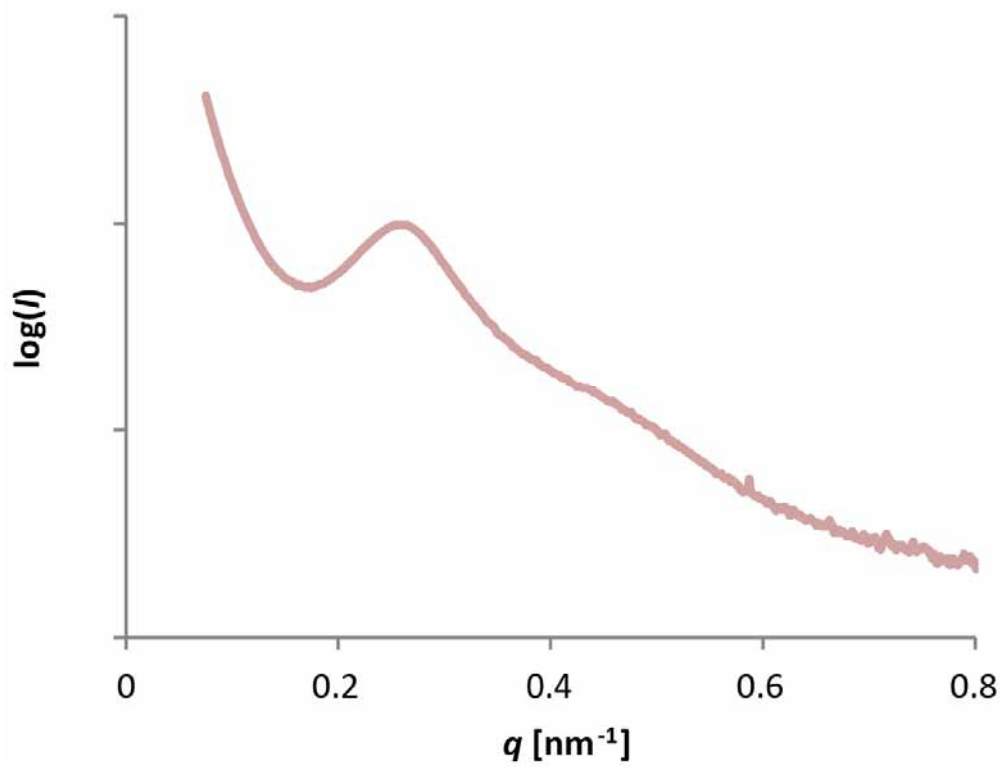
Figure 4.S2. Small-angle x-ray scattering of the parent PS-*b*-PEO BCP.
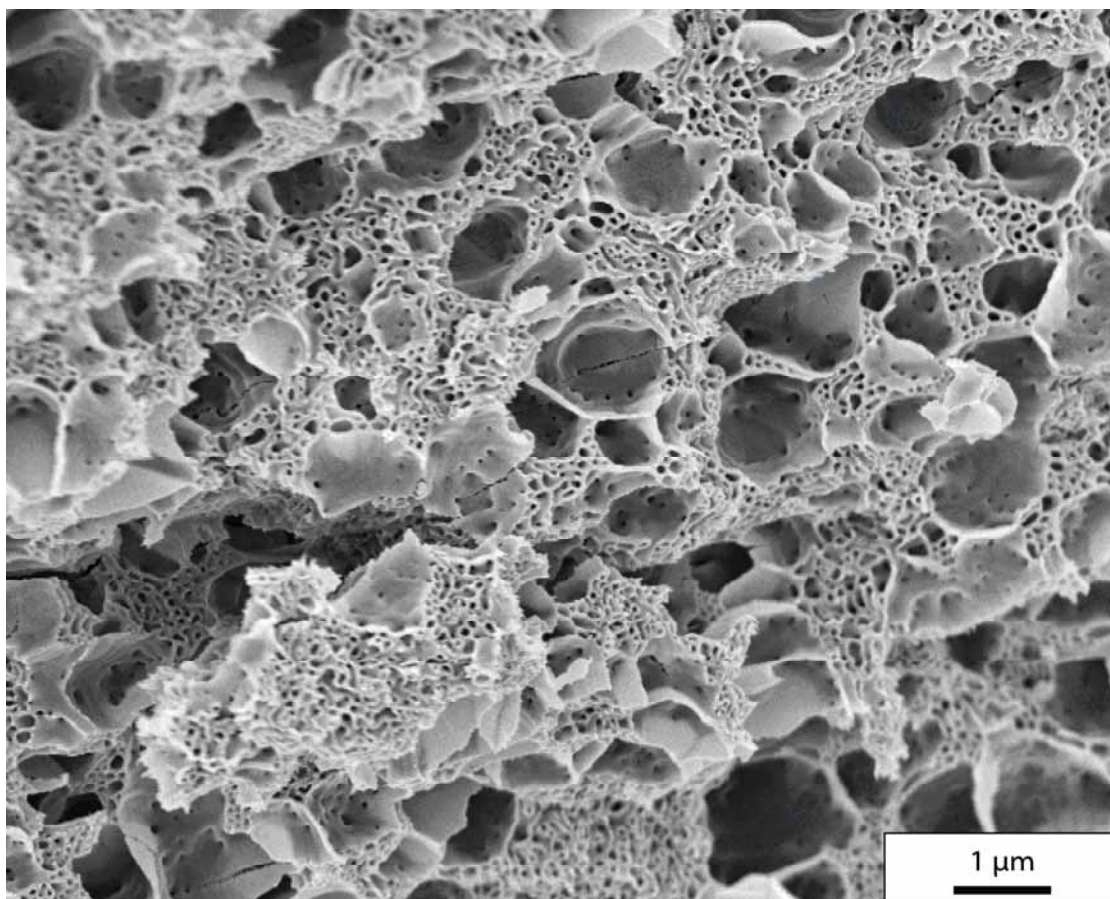
Figure 4.S3. SEM image of a PtBS-*b*-PEO scaffold following the SIM²PLE method.

REFERENCES

1.   Floudas, G.; Ulrich, R.; Wiesner, U., *J. Chem. Phys.* **1999,** *110* (1), 652-663.
2.   Finnefrock, A. C.; Ulrich, R.; Toombes, G. E. S.; Gruner, S. M.; Wiesner, U., *J. Am. Chem. Soc.* **2003,** *125* (43), 13084-13093.
3.   Lee, T. C.; Kashyap, R. L.; Chu, C. N., *CVGIP: Graphical Models and Image Processing* **1994,** *56* (6), 462-478.

CHAPTER 5

MORPHOLOGICAL CONTROL IN THE SYNTHESIS OF MACRO/MESO-
POROUS POLYMER SCAFFOLDS THROUGH SPINODAL DECOMPOSITION[*]

Abstract

Materials with connected porosity across multiple length scales are of
increasing interest as substrates for catalysis as well as scaffolds for other materials.
Here specific synthesis parameters were explored to produce hierarchically porous
polymer scaffolds using the spinodal-decomposition induced macro/meso-phase
separation plus extraction by rinsing (SIM^{2}PLE) method applied to the block
copolymer/additive system poly(styrene-*block*-ethylene oxide) / oligo(ethylene oxide).
Final film thickness influenced structure homogeneity across the film. Film casting
temperature affected both the macro- and meso-scale pore structure, most notably
causing changes in the mesoscopic morphology. Additive molar mass variations
altered macropore size while mesostructure essentially stayed unaffected. Three
different casting solvents for the system were found for which the method provides
connected porosity across different length scales. The results provide design criteria
for block copolymer/oligomer blend-based hierarchically porous scaffold formation
via the SIM^{2}PLE method.

[*] Sai, H.; Tan, K. W.; Gruner, S. M.; Wiesner, U. *In preparation*.

Introduction

Hierarchically porous materials with nanoscale features are of increasing interest due to fast transport of media through the pores coupled with enhanced surface area and improved mechanical stability.[1, 2] Such materials have potential applications in areas including membrane and separation science,[3-5] catalysis,[6-8] novel optical material design,[9, 10] and tissue engineering scaffolds for cell culture.[11, 12] Various processes have been developed to controllably fabricate such hierarchical structures, including colloidal crystal templating or pre-patterned substrates with mesostructure-forming precursors,[13-17] ice or salt-crystal templating,[18-20] and bio-templating.[21, 22] Many of these approaches involve multiple steps, however, including backfilling of preformed macroporous materials, thus suffering from a high level of complexity in synthetic protocols.

The use of polymer blends to form bicontinuous structures by spinodal decomposition has been widely studied as a viable approach to making polymer mesostructures and macrostructures.[23-28] As an example, polymeric bicontinuous microemulsions, formed by blending an AB block copolymer (BCP) with A and B oligomeric or polymeric additives, have been used as templates for backfilling with another structure-directing material to yield hierarchical structures.[29-32] Polymerization- and sol-gel induced phase separation has been applied to make monolithic hierarchical structures of silica and carbon materials.[33, 34] All-organic three-dimensional hierarchical structures obtained from this approach have been scarce in the literature, however.

BCP/additive blending has provided access to a large variety of morphologies and inspired researchers to study, in depth, the theoretical and experimental aspects.[26, 28, 35-43] The rich literature on the competition between macro- and micro-phase separation suggests that by controlling the formation kinetics a region in phase-space

may become accessible where continuous macroscale porosity is formed by macrophase separation of an additive-rich phase and a BCP-rich phase, followed by microphase separation on the mesoscale in the latter.

In a previous communication (Chapter 4 in this dissertation) we reported on the Spinodal-decomposition Induced Macro/Meso-phase separation PLus Extraction by rinsing (SIM²PLE) method, in which solvent evaporation from BCP/additive blend solutions of poly(styrene-*block*-ethylene oxide) / oligo(ethylene oxide) (PS-b-PEO/o-PEO) yielded macro- and meso-porous, hierarchical polymer scaffolds with ordered mesopores.[44] In the present paper we present a full account on this method. Parameters varied in this study include: film thickness, film casting temperature, molar mass of the additive, and casting solvents. Key parameters for continuous macropore morphology formation are identified. The results together provide a set of design criteria for successfully applying the SIM²PLE method to BCP/additive systems.

Experimental Section

Materials

A PS-*b*-PEO with total molar mass of $M_n =$ 36.5 kg/mol, PEO content of 13.7 wt% and polydispersity index of 1.03 was synthesized via sequential anionic polymerization as reported previously.[44] Other reagents, unless otherwise noted, were purchased from Sigma-Aldrich and used as received.

Synthesis

Hierarchically porous polymer films of approximately 100-200 μm thickness were prepared via spinodal-decomposition induced macro/meso-phase separation plus extraction by rinsing (SIM²PLE) according to the procedure described in Chapter 4 by screening the following three parameters: (1) film casting temperature, (2) o-PEO molar mass, and (3) solvents (Figure 5.1). Casting temperature was varied between
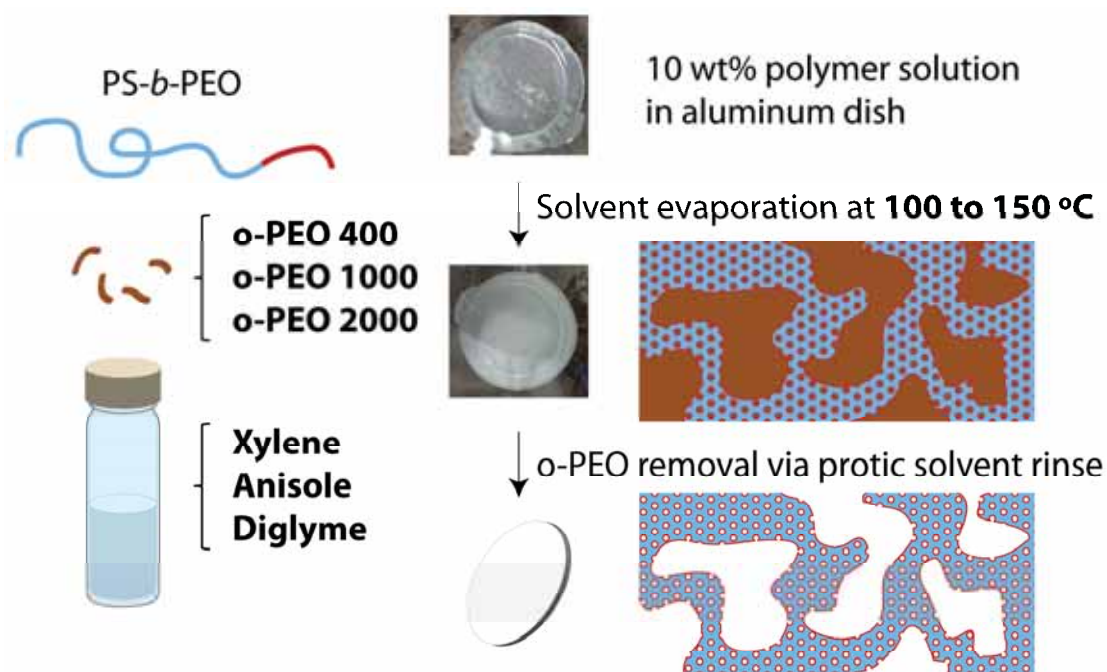
Figure 5.1. Schematic for the synthesis of macro/meso-porous polymer scaffolds using the SIM^{2}PLE method, with varying parameters in bold characters. Figure is adapted from Chapter 4.

Table 5.1. List of SIM^{2}PLE-cast films and synthesis conditions.

	Temperature / °C	**MW o-PEO / g·mol^{-1}**	**Solvent**
1[*]	100	400	Xylene
2[*]	130	400	Xylene
3	130	1000	Xylene
4	130	2000	Xylene
5	130	400	Anisole
6[*]	150	400	Anisole
7	150	400	Diglyme

[*] denotes films reported in Chapter 4.

100 °C and 150 °C. Three dihydroxyl terminated PEO oligomers with molar masses of 400, 1000 and 2000 g/mol were employed as o-PEO additive. Xylene, anisole and di(ethylene glycol) dimethyl ether (diglyme) were used as solvents. The weight ratio between PS-b-PEO and o-PEO was kept constant at 1:1. Table 5.1 provides a list of all films prepared together with their synthesis conditions. Solutions with 10 wt. % polymer in the selected solvent were poured into aluminum dishes subjected to heating on a hotplate covered with hemispherical glass chamber. We note that in xylene, o-PEO precipitates at room temperature, but readily dissolves upon heating to 40 °C. Film casting was completed within 1-2 hours, followed by rinsing in methanol at room temperature to remove the additive as the final pore formation step.

In a separate experiment to investigate the effect of casting conditions on macropore morphology, the BCP was dried to a pellet by heating in a vacuum oven at 200 °C for 3 days and used together with o-PEO400 obtained from a new bottle and handled under dry nitrogen to minimize the effect of any residual water content. This BCP/additive mixture was dissolved in xylene at 10 wt% and separated into four vials. Water was added at 0.1 wt% of the total solution to two of the vials. The films were then cast at 130 °C in aluminum dishes. One film with and one without additional water were removed from the hotplate approximately 5 minutes after macrophase separation became evident via strong film opacity, while the other two films were heated continuously for one hour total.

Characterization

Scanning electron microscopy (SEM) images were acquired on a Zeiss LEO 1550 field emission microscope with acceleration voltage of 2.0 kV using an in-lens detector. The samples were fractured to expose fresh cross-sections, mounted on carbon tape and sputter coated with gold-palladium.

Transmission small-angle x-ray scattering (SAXS) patterns were obtained on a home-built rotating anode beamline as well as at the G1 station of the Cornell High Energy Synchrotron Source (CHESS). Details of the beamline setup are described elsewhere.[45]

Results and Discussion

Effect of film casting environment on structural homogeneity and film morphology

In the SIM^2PLE film formation process, upon heating and solvent evaporation the block copolymer-additive mixture undergoes macroscopic phase separation into BCP-rich and additive-rich domains as well as mesoscale ordering in the BCP-rich phase/domains. The macrophase separation is visually observed by the onset of opacity in the casting solution. By tracking the mass loss we determined that for 1:1 PS-*b*-PEO/o-PEO400 films, formation of such macroscopic phases occur when polymer to solvent weight ratio becomes ~1:1. At a casting temperature of 130 °C with xylene as solvent, this onset of macrostructure formation roughly corresponded to a time point 5-10 minutes after the heating started.

The drying kinetics of films from polymer solutions is usually associated with formation of an evaporation front skin from a polymer gel near the vapor/solution interface, resulting in gradients in compositions from the film bottom to the evaporation front.[46-49] We have observed that when films of ~1 mm final thickness were cast from solution (corresponding to ~10 mm in initial thickness), solvent evaporation was blocked by the drying front causing significant vertical asymmetry in the polymer/solvent composition (see Supporting Information, Figure 5.S1). This could be suppressed by going to thinner films. Thus all subsequent films were cast to form a final thickness of only ~ 200 μm, for which film asymmetry as observed in

cross-sections of the final films was minimized (see Supporting Information, Figure 5.S2, for comparison with thicker films).

We also originally noted that prolonged (4 hours or more) heating of the samples led to gradual release of some vapor from the samples which appeared as fogging on the hemispherical casting chamber wall after all casting solvent was gone. Although the nature of the generated vapor is under investigation, we suspect that water is forming as a result of condensation reactions between chain ends of the o-PEO (the vapor pressure of o-PEO is negligible, especially for larger molar mass). As higher molar mass o-PEO's tend to exclude themselves from BCPs, the products of such reactions could lead to undesired structural alterations. Thus the cast films were quenched to room temperature at 1-2 hours after solvent evaporation was initiated.

Effect of casting temperature and solvents on pore structure

In addition to changes in the interaction parameters between PS and PEO blocks in the melt state, adjusting the casting temperature can alter the interaction between the PEO block and o-PEO, resulting in changes in the volume fraction between the PS and PEO domains in the BCP-rich region. In the previous communication, we have reported the formation of hexagonally packed inverse cylinders and cubic structures on the mesoscale when films were cast at 130 and 100 °C, respectively (Chapter 4).

The formation of macroporosity in the solution casting process is induced by the precipitation of o-PEO from the solution. Thus it is expected that if the additive solubility can be tuned in the solution phase, it would lead to changes in the onset time point for macrophase separation, which in turn can be used to tune the size of the final macropores. Table 5.2 lists the solubility parameters and boiling points of the solvents used in this study. Anisole was chosen as a direct comparison to xylene because of its

similarity in molecular structure with the exception of an additional ether group in anisole. This leads to higher o-PEO solubility in anisole when compared to xylene. Diethylene glycol dimethyl ether (diglyme) was chosen as the o-PEO-selective solvent possessing a similar boiling point to anisole. Since anisole and diglyme both have elevated boiling points, casting at higher temperatures was possible as compared to what was used for the xylene-containing samples.

We have reported previously (see chapter 4) that at a casting temperature of 130 °C, anisole-cast films displayed similar macroporosity as well as mesoporosity to xylene-cast films with similar channel-to-channel spacings. On the other hand, films cast from anisole at 150 °C (Figure 5.2a-b) showed a drastically different morphology than films cast from diglyme at 150 °C (Figure 5.2c-d). Small but irregularly sized macropores (1-3 μm) with cell wall thickness close to the block copolymer length scale (< 100 nm) were observed for anisole under these conditions (Figure 5.2a). No mesostructures were apparent in such films (Figure 5.2b). In contrast, films cast from diglyme at 150 °C showed an open cellular macropore structure (Figure 5.2c) with cylindrical/lamellar mesostructures in the walls (Figure 5.2d).

The lack of mesostructure in the anisole-cast film at 150 °C coincides with the observed delay in the onset of macrophase separation. The domain sizes of spinodal decomposition are determined by the incompatibility of the components (quench depth) and the polymer mobility. Since anisole is a good solvent for both PS and PEO domains, the effective Flory-Huggins interaction parameter is lowered by dilution with solvent. This induces a delay in the onset of macro- as well as meso-phase separation, which in turn provides less time for macrophase restructuring and coarsening and mesophase development. Diglyme provides an example of a selective solvent toward the PEO block, inducing early macro- and meso-phase separation and allowing for macrodomain coarsening similar to xylene.

Table 5.2. List of relevant solvent properties.

	Boiling point / °C	δ_D / MPa$^{1/2}$	δ_P / MPa$^{1/2}$	δ_H / MPa$^{1/2}$
Xylene	138.5	17.6	1.0	3.1
Anisole	153.6	17.8	4.1	6.7
Diglyme	162	15.8	6.1	9.2

Boiling points are from CRC Handbook of Physics and Chemistry.[54] Solubility parameters are from Hansen[55] and Barton. [56]
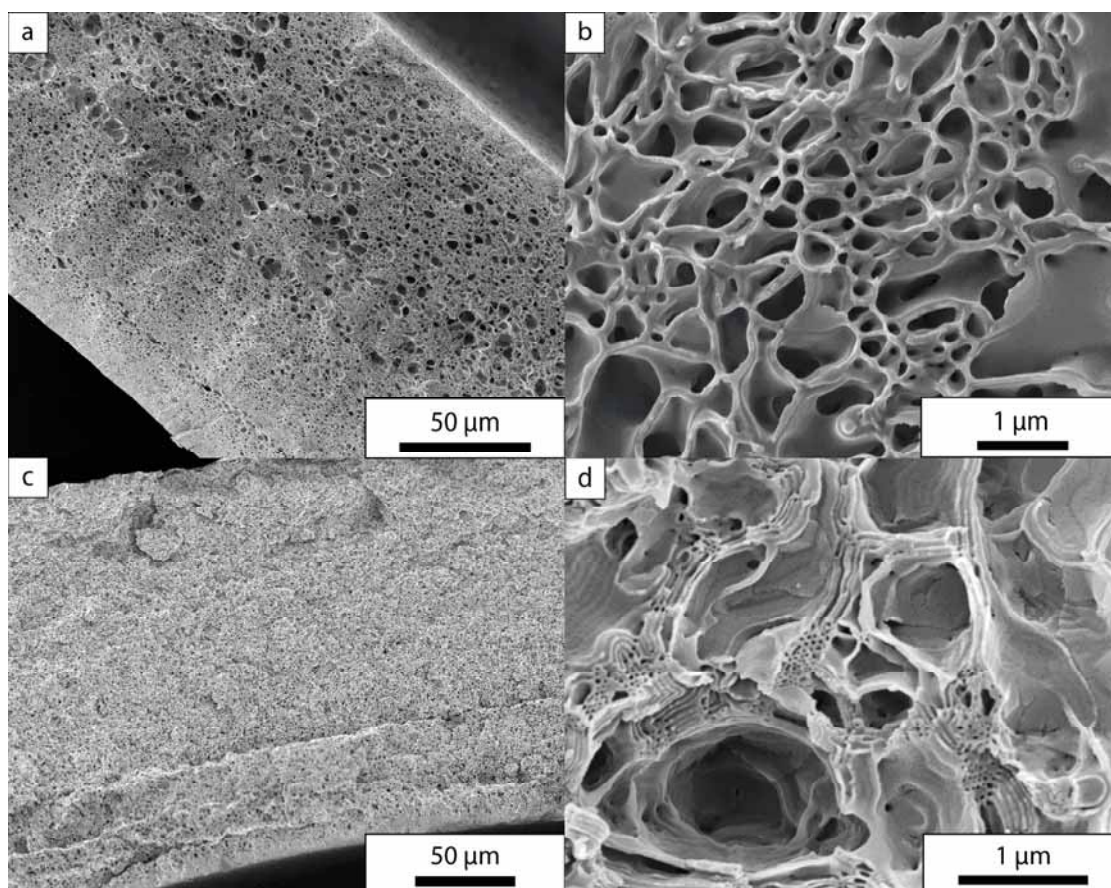

Figure 5.2. SEM images of films cast from (a-b) PS-*b*-PEO/o-PEO400 solution in anisole at 150 °C and (c-d) PS-*b*-PEO/o-PEO400 solution in diglyme at 150 °C.

The above trends together with the results of our earlier study suggest that casting temperature provides a handle on the mesoscale morphology while retaining macroporosity in the resulting materials. Although choice of the solvent, xylene, limited the usable temperature range to 138 °C, two distinct morphologies were observed at two distinct temperatures, namely a cubic lattice with symmetry of aspect 4 at 100 °C, and a hexagonal lattice at 130 °C. For anisole as the solvent, a hexagonal mesostructure in the walls was observed at 130 °C, while as shown here at 150 °C no mesopores are discerned in the relatively thin walls of the final material. It is worth noting that the shape of the macropores may be affected by the mesoscopic morphology: hexagonally arranged channels, intrinsically anisotropic compared to cubic mesostructures, can serve as a driving force for anisotropy in macropores, since the o-PEO does not provide confinement on mesoscopic lattice growth. A similar effect has been simulated and observed for PS-b-PI/PS blends with lamellar phases.[40, 50]

Effect of additive molar mass on pore structure

Homopolymer (HP) molar mass has been reported to affect the swelling behavior of BCP domains.[51] Mixing HPs that are larger than the compatible block of the block copolymer leads to macrophase separation, while mixing of HPs with smaller molar mass than the block of the BCP is generally considered entropically favaroble.[52] We hypothesize that o-PEO precipitates from the BCP system due to high degrees of self-association in o-PEO via hydrogen bonding of the end-groups.[53]

Figure 5.3 shows a series of SEM images on BCP/o-PEO blends from different molar mass o-PEOs cast from xylene at 130 °C. The film macrostructure (shown in Figure 5.3a-c) suggests a slight increase in macropore size and broadening of pore size distribution while the overall macroporosity seems to decrease. In contrast to the
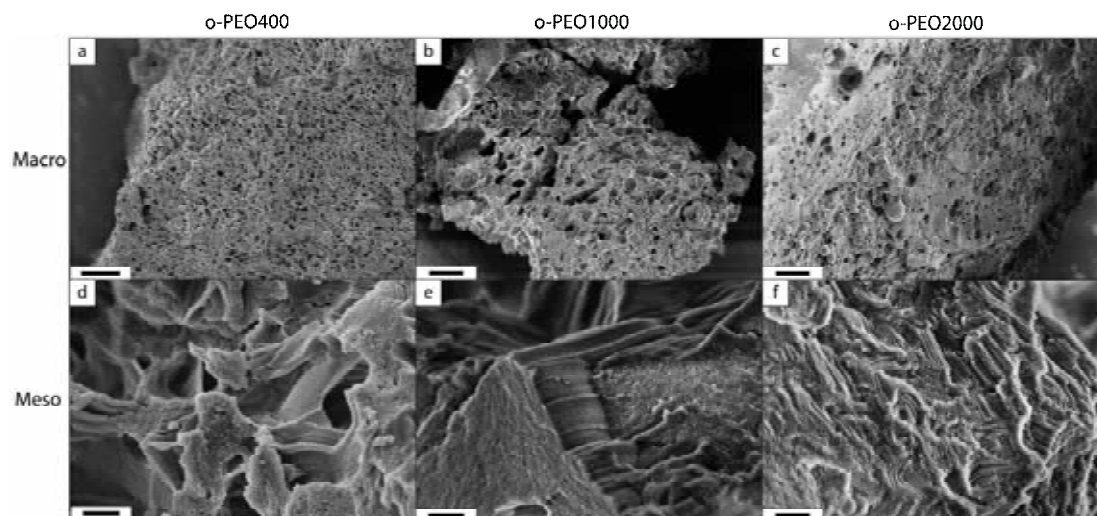
Figure 5.3. SEM images of PS-*b*-PEO/o-PEO blend films with different molecular weights of o-PEO after rinsing. (a-c) macrostructure of films with o-PEO400 (a), o-PEO1000 (b), and o-PEO2000 (c). All scale bars are 20 μm. (d-f) nanostructures of films with o-PEO400 (d), o-PEO1000 (e), and o-PEO2000 (f). Hexagonal structures are observed. All scale bars are 500 nm

structural variation observed as a function of casting temperature reported earlier, the BCP mesostructure (Figure 5.3d-f) did not show substantial changes as a function of o-PEO molar mass but stayed hexagonal in all cases. When o-PEO with a molar mass of 6000 g/mol was used (data not shown), i.e. slightly larger than the PEO block size of the PS-*b*-PEO, a clear film with two visually distinguishable domains formed, indicating complete macrophase separation.

Coarsening of the macrostructure with larger o-PEO's can be explained by the increased incompatibility between the PEO block and the additive o-PEO: as they become less compatible macrophase separation occurs earlier along the evaporation/heating timeline, allowing macrodomains to merge and grow. It is interesting that in contrast to the macrostructure, the film mesostructure does not considerably change when using additives with varying mixing limits. More detailed studies such as changing the end group functionalities in the PEO chains and observing the degree of association between o-PEO and BCP PEO domains vs. self-association of o-PEO would be needed, however, to better understand this phenomenon.

Effect of residual water and casting time on film formation kinetics

We finally note that casting duration and residual water content in the solution synergistically affect the resulting film morphology. After 3 to 4 months since the first sets of films were synthesized, including the seven films described in Table 5.1, we observed that the same experimental procedure failed to produce the networked macroporous structure, but instead lead to the formation of an isolated spherical/closed cellular macroporous structure (see Supporting Information, Figure 5.S3). In order to determine key parameters responsible for this change in the kinetically trapped morphology, we introduced a controlled amount of water and obtained two time points
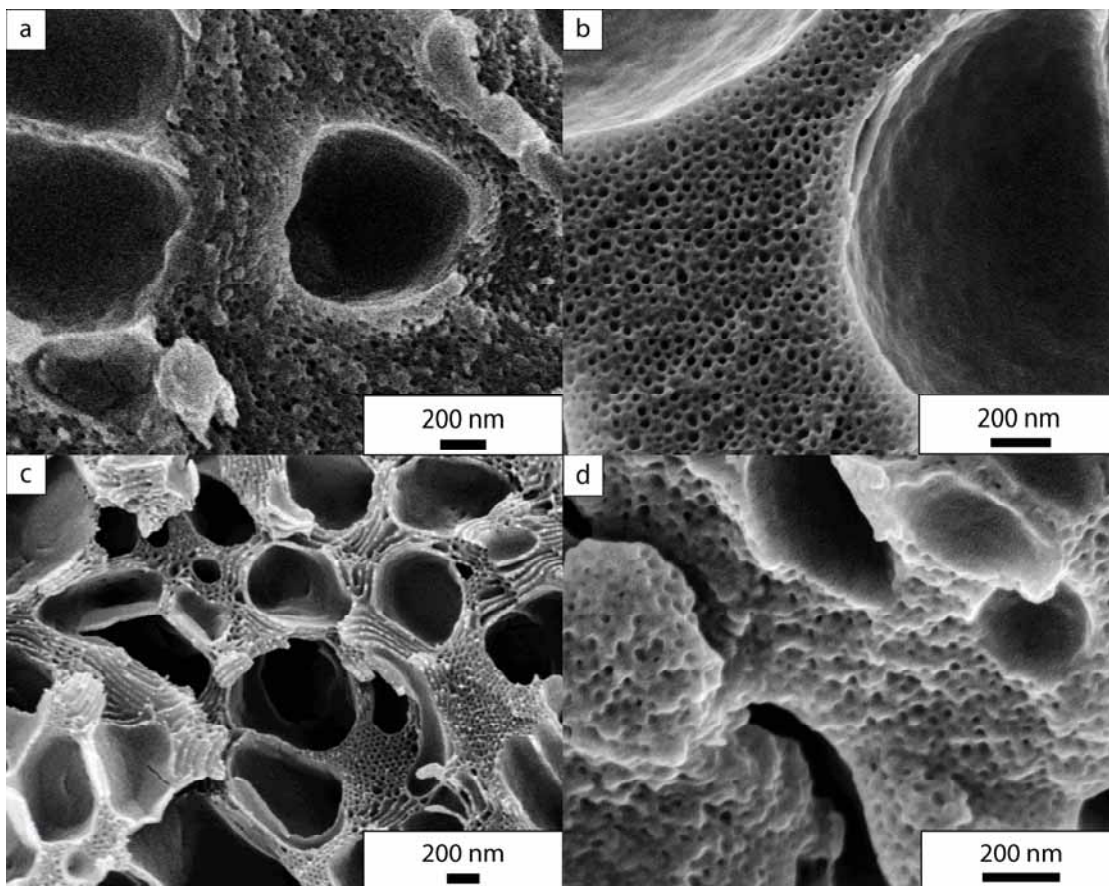
Figure 5.4. SEM images of films cast from (a-b) dry PS-*b*-PEO/o-PEO400 solution in xylene and (c-d) PS-*b*-PEO/o-PEO400 solution in xylene with 0.1 wt% water. Samples shown in (a,c) were heated for 5 minutes after macrophase separation. Samples shown in (b,d) were heated for 1 hour.

for water-free and water-containing films. Only the film that contained 0.1 wt% water in the solution and was heated for a short timeshowed the network macroporous structure (Figure 5.4). While these results point to the importance of water in the SIM^{2}PLE process in particular in the presence of PEO, further studies on how water content and other parameters not studied here affect the structure formation kinetics in detail are underway.

Design criteria for hierarchical structure formation through SIM^{2}PLE process

The above set of experiments indicates that mesostructure formation is largely dominated by factors such as temperature and volume fraction, while macrostructure formation is strongly affected by factors such as quench depth (supersaturation) and polymer mobility. From our results a number of requirements for successful hierarchical structure formation using the *SIM^{2}PLE process* can be identified:

1, The *BCP matrix block should be glassy at room temperature but rubbery at the casting temperature*: In order to provide mechanical stability after solvent evaporation and additive removal, the BCP has to be glassy at room temperature. However, mobility at casting temperature is required to provide equilibration in the mesophase.

2, *The additive-rich phase should phase-separate from the neat block copolymer phase while maintaining appreciable solubility in the block copolymer phase*: In order to provide mesoporosity after film rinsing, a considerable amount of additive should stay in the BCP-rich phase. In our case, o-PEO with a smaller molar mass than the BCP PEO block satisfied this condition by the self-associating nature of hydroxyl-terminated o-PEO.

3, *The solvent should be chosen such that the quench depth or supersaturation of the metastable polymer solution is suitable for forming macrostructures on the μm*

length scale: smaller macrophase separation length scales limit the BCP-rich phase from forming well-defined morphologies and prevent long-range order formation, while excessive coarsening of the macrostructure can result in film inhomogeneity.

Conclusion

A set of synthesis parameters in the SIM^{2}PLE process, including casting temperature, film thickness, o-PEO molar mass, and casting solvent, have been varied to study their effects on the hierarchical macro/meso-scale structure. Of these parameters, changing the casting temperature resulted in mesostructural transformations from hexagonal to cubic lattices to no mesostructure in the walls, while changes in the o-PEO molar mass and casting solvent caused variations in the kinetics of macrophase separation and coarsening of the macroscopic domains, thus altering the macroporosity in the final films. Film thickness variations changed the homogeneity of film structure. Other parameters, such as BCP molar mass, casting speed, water content (in particular in the presence of PEO), and polymer chemical functionality to tailor enthalpic interactions, need further studies to gain a deeper understanding of the structure formation within these films. The results provide design criteria for the successful hierarchically structure formation of hierarchical polymer scaffolds from BCP/additive blends using the SIM^{2}PLE process.

which is supported by the NSF and the National Institutes of Health/National Institute of General Medical Sciences under NSF award DMR-0936384.

REFERENCES

1.   Lakes, R., *Nature* **1993,** *361* (6412), 511-515.

2.   Innocenzi, P.; Malfatti, L.; Soler-Illia, G. J. A. A., *Chem. Mater.* **2011,** *23* (10), 2501-2509.

3.   Hillmyer, M., Nanoporous Materials from Block Copolymer Precursors. In *Block Copolymers II*, 2005; pp 137-181.

4.   Peinemann, K.-V.; Abetz, V.; Simon, P. F. W., *Nat. Mater.* **2007,** *6* (12), 992-996.

5.   Phillip, W. A.; Dorin, R. M.; Werner, J.; Hoek, E. M. V.; Wiesner, U.; Elimelech, M., *Nano Lett.* **2011,** *11* (7), 2892-2900.

6.   van Donk, S.; Janssen, A. H.; Bitter, J. H.; de Jong, K. P., *Catalysis Reviews-Science and Engineering* **2003,** *45* (2), 297-319.

7.   Yu, J.; Su, Y.; Cheng, B., *Adv. Funct. Mater.* **2007,** *17* (12), 1984-1990.

8.   Li, Y.; Sasaki, T.; Shimizu, Y.; Koshizaki, N., *J. Am. Chem. Soc.* **2008,** *130* (44), 14755-14762.

9.   Huang, Y.; Lieber, C. M., *Pure Appl. Chem.* **2004,** *76* (12), 2051-2068.

10.   Stein, A.; Li, F.; Denny, N. R., *Chem. Mater.* **2008,** *20* (3), 649-666.

11.   Bechtle, S.; Ang, S. F.; Schneider, G. A., *Biomaterials* **2010,** *31* (25), 6378-6385.

12.   Dankers, P. Y. W.; Boomker, J. M.; Huizinga-van der Vlag, A.; Wisse, E.; Appel, W. P. J.; Smedts, F. M. M.; Harmsen, M. C.; Bosman, A. W.; Meijer, W.; van Luyn, M. J. A., *Biomaterials* **2011,** *32* (3), 723-733.

13.   Yang, P. D.; Deng, T.; Zhao, D. Y.; Feng, P. Y.; Pine, D.; Chmelka, B. F.; Whitesides, G. M.; Stucky, G. D., *Science* **1998,** *282* (5397), 2244-2246.

14.   Rhodes, K. H.; Davis, S. A.; Caruso, F.; Zhang, B. J.; Mann, S., *Chem. Mater.* **2000,** *12* (10), 2832-+.

15.   Yu, S. H.; Colfen, H., *J. Mater. Chem.* **2004,** *14* (14), 2124-2147.

16.   Zhang, G.; Wang, D. Y.; Gu, Z. Z.; Mohwald, H., *Langmuir* **2005,** *21* (20), 9143-9148.

17.   Kamperman, M.; Burns, A.; Weissgraeber, R.; van Vegten, N.; Warren, S. C.; Gruner, S. M.; Baiker, A.; Wiesner, U., *Nano Lett.* **2009,** *9* (7), 2756-2762.

18.   Lu, A. H.; Li, W. C.; Schmidt, W.; Schuth, F., *Microporous Mesoporous Mater.* **2006,** *95* (1-3), 187-192.

19.   Khan, F.; Walsh, D.; Patil, A. J.; Perriman, A. W.; Mann, S., *Soft Matter* **2009,** *5* (16), 3081-3085.

20.   Mori, H.; Aotani, K.; Sano, N.; Tamon, H., *J. Mater. Chem.* **2011,** *21* (15), 5677-5681.

21.   Chen, Y.; Gu, J.; Zhang, D.; Zhu, S.; Su, H.; Hu, X.; Feng, C.; Zhang, W.; Liu, Q.; Parker, A. R., *J. Mater. Chem.* **2011,** *21* (39), 15237-15243.

22.   Cho, K.; Na, K.; Kim, J.; Terasaki, O.; Ryoo, R., *Chem. Mater.* **2012**.

23.   Cahn, J. W., *J. Chem. Phys.* **1965,** *42* (1), 93-&.

24.   Bates, F. S., *Science* **1991,** *251* (4996), 898-905.

25.   Bates, F. S.; Maurer, W. W.; Lipic, P. M.; Hillmyer, M. A.; Almdal, K.; Mortensen, K.; Fredrickson, G. H.; Lodge, T. P., *Phys. Rev. Lett.* **1997,** *79* (5), 849-852.

26.   Floudas, G.; Hadjichristidis, N.; Stamm, M.; Likhtman, A. E.; Semenov, A. N., *J. Chem. Phys.* **1997,** *106* (8), 3318-3328.

27.   Fredrickson, G. H.; Bates, F. S., *J. Polym. Sci., Part B: Polym. Phys.* **1997,** *35* (17), 2775-2786.

28.   Likhtman, A. E.; Semenov, A. N., *Macromolecules* **1997,** *30* (23), 7273-7278.

29.   Fleury, G.; Bates, F. S., *Soft Matter* **2010,** *6* (12), 2751-2759.

30.   Jones, B. H.; Lodge, T. P., *Chem. Mater.* **2010,** *22* (4), 1279-1281.

31.   Jones, B. H.; Lodge, T. P., *Chem. Mater.* **2011,** *23* (21), 4824-4831.

32.   Jones, B. H.; Lodge, T. P., *ACS Nano* **2011,** *5* (11), 8914-8927.

33.   Nakanishi, K.; Amatani, T.; Yano, S.; Kodaira, T., *Chem. Mater.* **2008,** *20* (3), 1108-1115.

34.   Liang, C.; Dai, S., *Chem. Mater.* **2009,** *21* (10), 2115-2124.

35.   Whitmore, M. D.; Noolandi, J., *Polym. Eng. Sci.* **1985,** *25* (17), 1120-1121.

36.   Hashimoto, T.; Kimishima, K.; Hasegawa, H., *Macromolecules* **1991,** *24* (20), 5704-5712.

37.   Semenov, A. N., *Macromolecules* **1993,** *26* (9), 2273-2281.

38.   Izumitani, T.; Hashimoto, T., *Macromolecules* **1994,** *27* (7), 1744-1750.

39.   Matsen, M. W., *Phys. Rev. Lett.* **1995,** *74* (21), 4225-4228.

40.   Ohta, T.; Ito, A., *Phys. Rev. E* **1995,** *52* (5), 5250-5260.

41.   Lee, J. H.; Balsara, N. P.; Chakraborty, A. K.; Krishnamoorti, R.; Hammouda, B., *Macromolecules* **2002,** *35* (20), 7748-7757.

42.   Martinez-Veracoechea, F. J.; Escobedo, F. A., *Macromolecules* **2009,** *42* (22), 9058-9062.

43.   Martinez-Veracoechea, F. J.; Escobedo, F. A., *Macromolecules* **2009,** *42* (5), 1775-1784.

44.   Sai, H.; Tan, K. W.; Gruner, S. M.; Wiesner, U., In preparation.

45.   Finnefrock, A. C.; Ulrich, R.; Toombes, G. E. S.; Gruner, S. M.; Wiesner, U., *J. Am. Chem. Soc.* **2003,** *125* (43), 13084-13093.

46.   Vrentas, J. S.; Vrentas, C. M., *J. Polym. Sci., Part B: Polym. Phys.* **1994,** *32* (1), 187-194.

47.   Vrentas, J. S.; Vrentas, C. M., *J. Appl. Polym. Sci.* **1996,** *60* (7), 1049-1055.

48.   Alsoy, S.; Duda, J. L., *Drying Technol.* **1998,** *16* (1-2), 15-44.

49.   Okuzono, T.; Ozawa, K.; Doi, M., *Phys. Rev. Lett.* **2006,** *97* (13).

50.   Koizumi, S.; Hasegawa, H.; Hashimoto, T., *Macromolecules* **1994,** *27* (22), 6532-6540.

51.   Abetz, V.; Simon, P., Phase Behaviour and Morphologies of Block Copolymers. In *Block Copolymers I*, 2005; pp 125-212.

52.   Jiang, M.; Xie, H. K., *Prog. Polym. Sci.* **1991,** *16* (6), 977-1026.

53.   Sarkar, A.; Ghosh, K., *Kolloid-Zeitschrift and Zeitschrift Fur Polymere* **1970,** *236* (2), 140-142.

54.   *CRC handbook of chemistry and physics.* **1978.**

55.   Hansen, C. M. *Ind. Eng. Chem. Prod. Res. Dev.* **1969,** *8* (1), 2-11.

56.   Barton, A. F. M., *Chem. Rev.* **1975,** *75* (6), 731-753.

Figure 5.S1. Photograph of a PS-*b*-PEO/o-PEO mixture cast from xylene solution at 130 °C with the projected film thickness of 1 mm. Note the dual layer appearance in the vessel, where bottom layer is wet with solvent and top layer dense and dry.
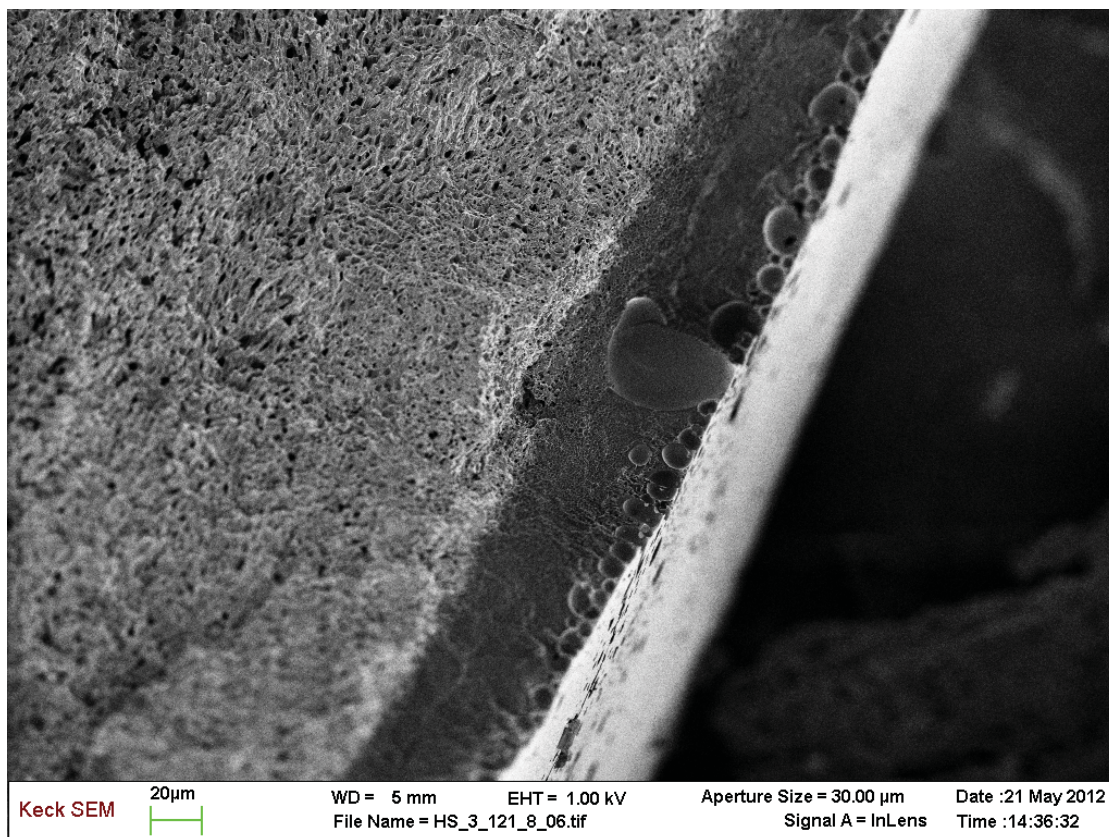
Figure 5.S2. SEM image of a PS-*b*-PEO/o-PEO mixture cast with an approximately 400 µm film thickness. A dense skin layer of 40 µm is visible.
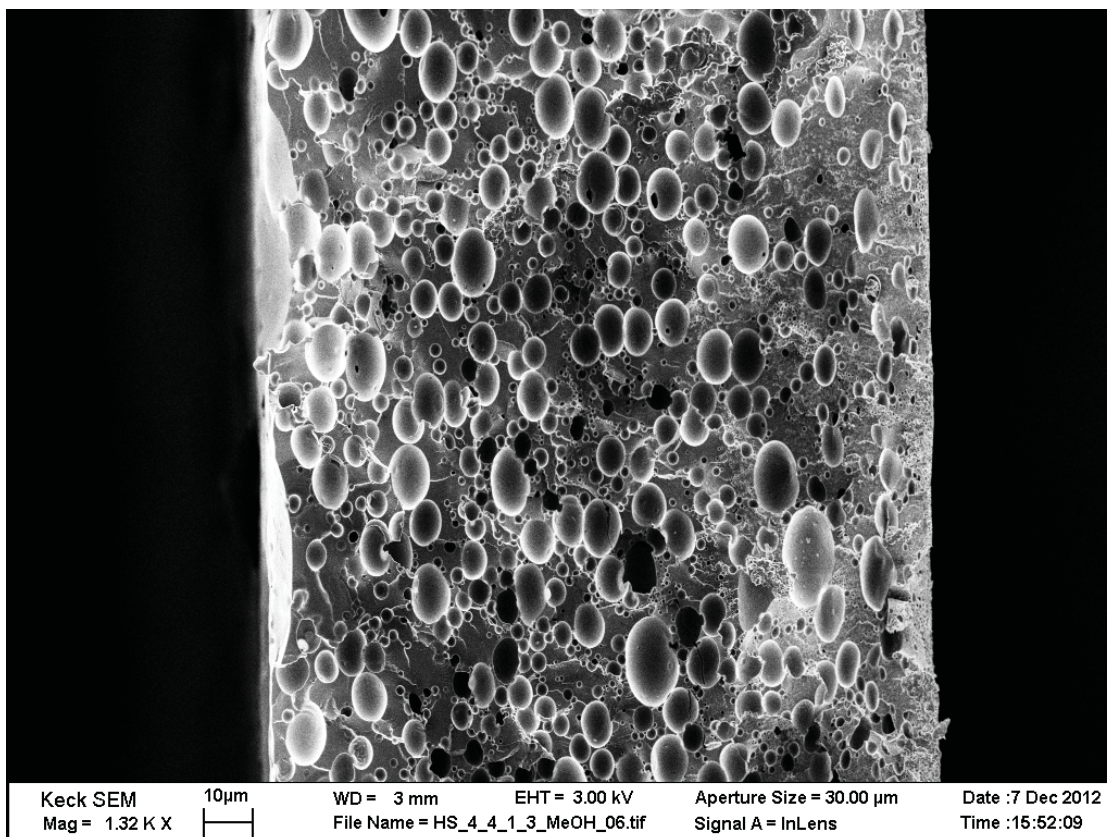
Figure 5.S3. SEM image of a PS-*b*-PEO/o-PEO mixture showing spherical closed macroporosity.

CHAPTER 6

CONCLUSION

In this dissertation, I have explored various facets of complexity in synthetic self-assembly nanomaterials: multicompartment nanoparticles (Chapter 2), multicomponent organic/inorganic hybrid materials (Chapter 3), and hierarchically porous polymer scaffolds (Chapters 4 and 5).

In Chapter 2, a new type of mesoporous silica nanoparticle was synthesized and characterized containing multiple mesoscopic lattices within a single particle, referred to as multi-MSNs. Ethyl acetate concentration in the reaction feed was identified as a key parameter for controlling multi-MSN morphologies.

In Chapter 3, organic/inorganic hybrid nanomaterials from the amphiphilic block copolymer PI-*b*-PDMAEMA and Pt NPs were synthesized and characterized. Study of the ligand density on the nanoparticle surface revealed possible interactions between free metal surface and aminated polymer side-chains. Changing the ratio of BCP to NP resulted in a variety of mesostructures, some of which could subsequently be dissociated into nano-objects via selective dissolution of the matrix PI block.

In Chapters 4 and 5, hierarchically porous three-dimensional polymer scaffolds were synthesized via the SIM^{2}PLE method. Spinodal decomposition of the BCP/additive mixtures resulted in macrostructure formation accompanied by microphase separation of the BCP-rich domains resulting in ordered mesostructures. A facile washing step with protic solvents yielded the final porous polymer scaffolds. Design criteria for the synthetic method with control over mesopore lattices and macropore sizes were identified.

In summary, I have shown that by fine-tuning the building block compositions and thermodynamic synthesis conditions, one can design and prepare potentially functional nanomaterials via bottom-up-type self-assembly approaches common in biological systems.

One can extrapolate this work to various future directions by combining multiple of the features observed. For example, in conjunction with multicompartment and multicomponent materials, a drug delivery system where different compartments in the multi-MSNs are loaded with different drug molecules would be an interesting application. Between multicompartment and multi-length scale features, BCPs that can incorporate MSNs in one block would constitute a hierarchically structured catalytic support that would prevent clogging and caking of side-products on small pores. Finally, incorporating inorganic nanoparticles in SIM^{2}PLE scaffolds or backfilling of the scaffolds with deposition processes can lead to multicomponent hierarchical structures.